

PROPERTIES AND APPLICATIONS OF WHISPERING-
GALLERY MODE RESONANCES IN FUSED
SILICA MICROSPHERES

By

JEROMY PAUL REZAC

Bachelor of Science

North Dakota State University

Fargo, North Dakota

1995

Submitted to the Faculty of the
Graduate College of the
Oklahoma State University
in partial fulfillment of
the requirements for
The Degree of
DOCTOR OF PHILOSOPHY
August, 2002

UMI Number: 3102817

UMI[®]

UMI Microform 3102817

Copyright 2003 by ProQuest Information and Learning Company.

All rights reserved. This microform edition is protected against
unauthorized copying under Title 17, United States Code.

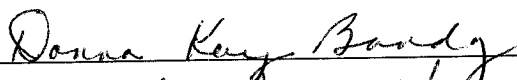
ProQuest Information and Learning Company
300 North Zeeb Road
P.O. Box 1346
Ann Arbor, MI 48106-1346

PROPERTIES AND APPLICATIONS OF WHISPERING-
GALLERY MODE RESONANCES IN FUSED
SILICA MICROSPHERES

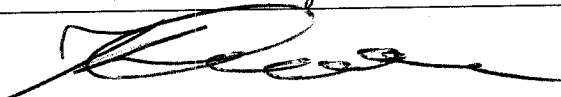
Thesis Approved:

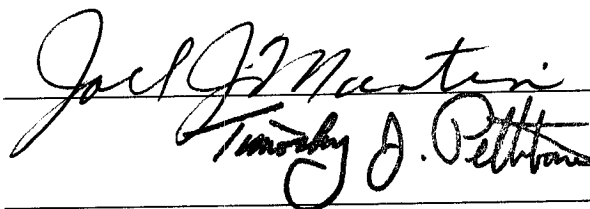
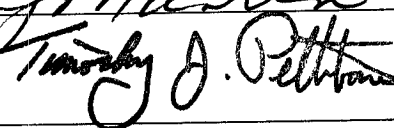


Thesis Advisor







Dean of Graduate College

ACKNOWLEDGEMENT

I would like to thank all of the people who have influenced and supported me throughout the years, whether in the academic field or in a personal nature. At the top of the list is my wife, Jean, who has been with me for a good portion of this journey. I am very grateful for her love and support and for the patience and understanding she has shown for the long hours and stress associated with this Ph.D. I would like to thank my parents for the love and support they have given me all my life. They provided a stable and nurturing environment that enabled me to grow.

Of course, this research and dissertation would not have been possible without the instruction of my advisor and mentor, Dr. Al Rosenberger. I owe him a big THANK YOU for the endless hours of discussions and help. His trust in my abilities has allowed me to explore my potential and expand into many diverse areas of research. My success is a mark of his guidance.

I am very grateful for all of the friends I have made over the past years. Without them, I would not have had the courage or the desire to endure this long journey. Fortunately, there are too many of you to list. I am also grateful to the faculty and staff at the physics department for making my stay memorable. I would like to extend a special thank to Dr. Donna Bandy, who has been more than just a committee member and instructor, but also a person who has been interested in my career, research, and overall well being.

Working with fellow students in the lab has been one of most rewarding aspects in my education, I would like to thank George Farca, Siyka Shopova, Reza Mofid, Seth Koterba, and Sarah Bates for their hard work and friendship. Much of the work in this dissertation is a result of their work and thought provoking questions.

TABLE OF CONTENTS

Chapter	Page
I. INTRODUCTION	1
II. MICROSPHERE CAVITY THEORY	6
1. Whispering Gallery Mode Equations.....	6
2. Ring Cavity Model.....	12
(a) Theory	12
(b) Solutions and Physical Interpretation	18
III. GENERAL EXPERIMENTAL PROCEDURES	21
1. Introduction.....	21
2. Microsphere Fabrication	22
3. Coupling Techniques	26
4. Tapered Fiber Fabrication and Coupling	30
5. Limitations	34
(a) Experimental Test of Ring Cavity Model.....	34
(b) Fiber Mode Coupling.....	38
6. Laser Properties	41
IV. COMPRESSION TUNING AND LASER FREQUENCY TRACKING	45
1. Introduction.....	45
2. Theory	46
3. Experimental Setup.....	48
4. Tuning Results	53
5. Locking Results	56
6. Summary and Conclusions	60
V. TEMPERATURE TUNING AND THERMAL BISTABILITY	63
1. Introduction.....	63
2. Thermal Conductivity of Air	66
(a) Theory	66
(b) Experimental Setup and Results	68

3. Thermal Bistability	75
(a) Introduction.....	75
(b) Theory.....	77
(c) Experimental Setup and Results	79
VI. MICROSPHERES AS SENSORS	85
1. Introduction.....	85
2. Theory.....	87
3. Experimental Results	91
(a) Liquid Chemical Detection.....	91
(b) Trace Gas Detection.....	96
BIBLIOGRAPHY.....	101
APPENDIX.....	107
MODIFIED RING CAVITY MODEL.....	107

LIST OF TABLES

Table	Page
III.1. Loss coefficient of fused silica at selected wavelengths	22
III.2. Summary of prism and fiber coupling properties.	28
III.3. Calculated values of T_l and α_i from the measured dip depth and Q at varied gap distances between the taper-fiber and microsphere	37
IV.1. Tuning ranges for a 550- μm diameter microsphere at two wavelengths.....	61
V.1. Summary of parameters for Fig. V.6.	83
V.2. Summary of parameters for Fig. V.7.	84
VI.1. Absorption coefficient for varying concentrations of ICG in methanol at a wavelength of 800 nm.....	92
VI.2. Experimental effective detection path length from CO_2 data.	100
VI.3. Expected effective detection path length from the observed WGM Q and dip depth.....	100

LIST OF FIGURES

Figure	Page
II.1 Representation of the WGM structure for different mode numbers and polarization.	7
II.2 Spectrum of WGM.....	11
II.3 Model of four-mirror ring cavity	13
III.1 Input and output coupling to a WGM using prisms and tapered-fiber coupling, demonstrating reflection and transmission signals	28
III.2 Apparatus designs for mounting bi-tapered fibers.....	33
III.3 Frequency scans of WGMs with varying gap distances between the tapered fiber and microsphere	37
III.4 Representation of mode coupling between two of the lowest order modes of a tapered fiber fabricated from a single mode fiber.....	39
III.5 Laser power through free space and a tapered fiber as a function of wavelength.	39
III.6 Constant frequency tapered fiber transmission during HF acid etching.....	40
III.7 Tunable diode laser's scan range as a function of scan frequency.	44
III.8 Hysteresis of tunable diode laser frequency with applied voltage for fine frequency tuning	44
IV.1 Experimental setup for compression tuning and locking the WGM to a laser	49
IV.2 Capacitive voltage divider used to combine DC bias and modulation signal from lock-in stabilizer for application to compressor PZT.	49
IV.3 Schematic of compression tuner	50
IV.4 Scan range, for a 2.5-V amplitude sinusoidal voltage applied to the PZT, versus frequency.....	55

IV.5	Maximum tuning speed of compression tuner with 2.5-V sinusoidal signal.....	55
IV.6	Unlocked and locked frequency scans at 1570 nm over a 19-GHz scan range.	57
IV.7	Locked tuner PZT bias as it follows a 19-GHz frequency scan (and return) of the tunable diode laser at 1570 nm	59
V.1	WGM temperature dependence of a 700- μ m diameter microsphere.....	65
V.2	Vacuum chamber used for performing pressure-dependent experiments or trace gas detection.....	70
V.3	Resonance frequency shift used to determine the temperature rate of change.	73
V.4	Log plot of microsphere temperature above equilibrium vs. time at 350 mTorr for increasing and decreasing frequency scan direction.....	73
V.5	Pressure vs. thermal conductivity for two different spheres plotted against a theoretical curve.....	74
V.6	Representation of thermal bistability for different scan directions.....	76
V.7	WGM thermal bistability at varying pressure and constant laser scan rate.	83
V.8	WGM thermal bistability of different laser scan rates at 0.35 Torr.....	84
VI.1	Effective path lengths associated with the intracavity path length and effective detection path length, constant α_i	90
VI.2	Effective path lengths associated with the intracavity path length and effective detection path length, constant T_l	90
VI.3	Absorption spectrum of ICG in methanol for a 1-micromolar-concentration solution.....	92
VI.4	Multiple scans of the same WGM of a microsphere immersed in methanol and varying concentrations of ICG dye.....	94
VI.5	Normalized position of WGM dip bottom with varying ICG concentration.....	94
VI.6	Experimental setup for trace gas detection.	97
VI.7	WGM spectrum for three different CO ₂ concentrations at atmospheric pressure at the 1572.4-nm absorption line	99

A.1	Representation of the two-mode tapered fiber coupling to the microsphere	108
A.2	Modified ring cavity model	108
A.3	Theoretical curves with the modified ring cavity model	115
A.4	Apparent absorption coefficient using the original ring cavity model with the dip depth and Q calculated from the modified two-mode model	116
A.5	Experimental verification of peaks in the modified ring cavity model.	119
A.6	Experimental verification of asymmetry in the modified ring cavity model.	119

CHAPTER I

INTRODUCTION

Fire! In 1666, The Great Fire of London devastated Stuart London, destroying 80 percent of the city along with Old St. Paul's Cathedral. The 33-year-long project of constructing a new St. Paul's Cathedral, designed by Sir Christopher Wren, began nine years later in 1675. In its dome, 259 steps up from ground level, is the Whispering Gallery. It's given this name because a whisper breathed against its wall bounces along the surface to the far side of the dome, 112 feet away, where it is audible. This idea can also be applied to optical waves where light is guided around the inside of a circular resonator, cylindrical or spherical, bound by continuous total internal reflection (TIR). Of particular interest is the case where after one round trip the light is in phase with itself, resulting in a resonance condition. This special case is given the name whispering-gallery mode (WGM). The general theory of these optical resonances in a spherical dielectric was first studied in 1939 by Richtmyer^[1] and is included in staple electromagnetic textbooks.^[2] The advent of monochromatic light sources, namely lasers, allows WGMs to be experimentally validated and their extraordinary properties exploited. The purpose of this dissertation is to study the physics of the WGMs in a spherical dielectric and present practical uses for these microresonators.

Associated with total internal reflection is an evanescent field that extends into the adjacent medium. Overlapping a source evanescent field with that of the resonator

allows light to couple in and out of the WGMs; this evanescent coupling can be viewed as photon tunneling. A direct analogy can be drawn between the microsphere with evanescent coupling and a passive ring cavity with very high reflectivity mirrors and some additional intrinsic loss. A cavity constructed from mirrors that are all highly reflective means the cavity fills slowly and if the intrinsic losses are too large, there will be minimal intracavity buildup. Fortunately, the low attenuation fused silica used to fabricate the microspheres has been well developed for fiber optic applications.

In our lab, WGMs have been observed in a cylindrical optical fiber and in a microsphere fabricated from the same fiber. The microsphere has the advantage that its curved surface has the effect of continuously refocusing the light, confining it to the equatorial region. Another example of a confined evanescently coupled microresonator is a thin microdisk,^[3] where the top, bottom and edge of the disk confine the light. This type of microcavity suffers from added losses from the top and bottom sides, limiting the quality (Q) factor. All of the work presented in this dissertation is performed with microspheres. Therefore, whenever the term whispering-gallery mode is used, it refers to the whispering-gallery modes of a microsphere. Ideally, microspheres possess Q values up to 1×10^{10} , linewidths of tens of kHz, and cavity lifetimes on the order of microseconds.

In Chapter II, the basic nomenclature and fundamental principles needed to discuss and analyze experimental data is presented. A basic description of WGM resonance is presented followed by a review of the WGM equations. A model in the form of the previously mentioned four-mirror ring cavity is developed for microsphere coupling and losses in order to describe the observed reflected and transmitted signals

along with the intracavity intensity. Inclusion of intracavity loss to simulate the microsphere's intrinsic losses from material absorption, surface scattering, and surface contaminants, such as water, makes the model different from the standard four-mirror ring cavity. This chapter concludes with a brief description of the model's limitations.

Chapter III details the general experimental techniques employed during most of the experiments presented. This includes a description of microsphere fabrication and tapered fiber construction from single mode optical fiber with a hydrogen-oxygen (H-O) torch, along with mounting techniques for each. Since proper analysis of data is impossible without understanding the tools used, the very important task of examining the properties of the lasers used is performed. Experimental data is presented to verify the ring cavity model and demonstrate its limitations with tapered fiber coupling. This leads to a modified model that is presented in the Appendix, placed there since the results of this model possibly affect the interpretation of all the experimental results throughout this dissertation. The extended model does not change the fundamental principles nor most of the results presented, but does warrant consideration for future projects. The transmission properties of the bi-tapered fiber are described and also used to develop the modified model in the Appendix.

Microsphere resonance frequency tuning is introduced in Chapter IV. In certain situations, the ability to tune a WGM resonance frequency a short distance is beneficial. A good example is tuning to a molecular absorption line. A compression tuner that is capable of fine-tuning a microsphere over a free spectral range (FSR) using a piezoelectric actuator and up to ten free spectral ranges using a coarse tuning screw is presented. Using the compression tuner in conjunction with a commercial lock-in

stabilizer, a microsphere resonance is locked to a tunable laser at 1570 nm or 830 nm. Locked tracking ranges of a FSR are possible and compression modulation rates of up to 13 kHz have been achieved with tuning speed of at least 16 GHz/ms.

More resonance frequency tuning is presented in Chapter V. In this chapter, tuning is controlled by temperature rather than compression. With a sensitivity of 1.6 GHz/K, thermal effects are easily observed and potentially troublesome. In the first part of this chapter, the WGM resonance frequencies are used as passive elements to determine the temperature change of the microsphere per unit time. With this tool, the thermal decay rate of a microsphere heated slightly above room temperature is monitored. This leads to the determination of the thermal conductivity of air around the microsphere and the accommodation coefficient of air on fused silica. Using a vacuum chamber designed for microsphere experiments, the thermal decay rate and conductivity are examined as a function of air pressure. The experimentally determined thermal decay rate is then used in the second part of this chapter, which examines the interesting phenomenon of thermal bistability. The term thermal bistability refers to the apparent lineshape and linewidth of the WGM being dependent upon the laser frequency scan direction, resulting from microsphere heating due to power lost from intracavity absorption.

Presented in Chapter VI are the theory and experimental results of intracavity chemical sensing and trace gas detection. Any absorptive medium present in the evanescent field of the microsphere effectively changes the absorption coefficient of the cavity. In the case of intracavity chemical sensing, the microsphere is immersed in methanol. By adding a dye (indocyanine green) and methanol solution to that

surrounding the microsphere, nanomolar changes in concentration are observed by monitoring the depth of the dip, which changes due to the increased absorption. From experimental data, the absorption coefficient of the nanomolar solution is extrapolated. In the same manner, the effective absorption coefficient is changed by adding a gas, with an absorption line at the same frequency as a WGM, to the ambient atmosphere surrounding the microsphere. Experimental results using CO₂ gas are examined. Despite the small size of the microsphere, the high Q of the WGM gives effective absorption lengths on the order of meters.

The Appendix develops the modified ring cavity model that is necessary to describe the asymmetry in observed WGM resonance dips when using tapered fiber coupling. It also predicts the observed phenomenon of peaks or partial peaks in the reflection spectrum near resonance frequencies. The model is based on two modes propagating in the tapered region of the coupling fiber. Comparing the modified model to the original model reveals that the intrinsic Q of the microsphere may be higher than first predicted, possibly changing the interpretation of all the experimental results where tapered fiber coupling was employed; this is consistent with the sensor results in Chapter VI. Experimental examples are given to validate the model. This model suggests that further study and improved methods of tapered fiber fabrication are necessary.

In addition to the topics covered in this dissertation, our lab has studied microspheres for use as spectrum analyzers, microlasers,^[4-6] and to observe nonlinear effects.^[7-9] Additionally, the unique properties of microspheres gives them the potential to be used in areas such as cavity QED,^[10] atom trapping,^[11, 12] laser stabilization,^[13] and telecommunications applications.^[14-16]

CHAPTER II

MICROSPHERE CAVITY THEORY

1. Whispering Gallery Mode Equations

Microsphere WGMs are characterized by polarization and three mode numbers q , ℓ , and m and are denoted by $TE_{q\ell m}$ or $TM_{q\ell m}$. A representation of how these numbers define the WGM structure is shown in Figure II.1. The mode is transverse electric (TE) when the main component of the electric field is oriented tangentially to the microsphere surface and transverse magnetic (TM) when it is oriented radially. The mode number q gives the number of intensity maxima in the radial direction and ℓ gives the number of wavelengths in the propagation distance around the equator of the microsphere. More specifically, the integer number of wavelengths around the circumference of the microsphere is given, for a particular WGM, by $\ell = \beta_{q\ell m}^{TE(M)} a$. Here a is the microsphere

radius and $\beta_{q\ell m}^{TE(M)} = \frac{n_{eff} \omega_{q\ell m}^{TE(M)}}{c}$ is the effective propagation constant defining the effective index of refraction of the whispering-gallery mode. The effective index varies with polarization and mode numbers due to the fact that each WGM has a different percentage of the mode in the evanescent field and its value lies between that of the microsphere (n_s) and that of the surrounding medium (n_a), that is $n_a < n_{eff} < n_s$.

The mode number m gives the number of intensity maxima in “latitude”, or

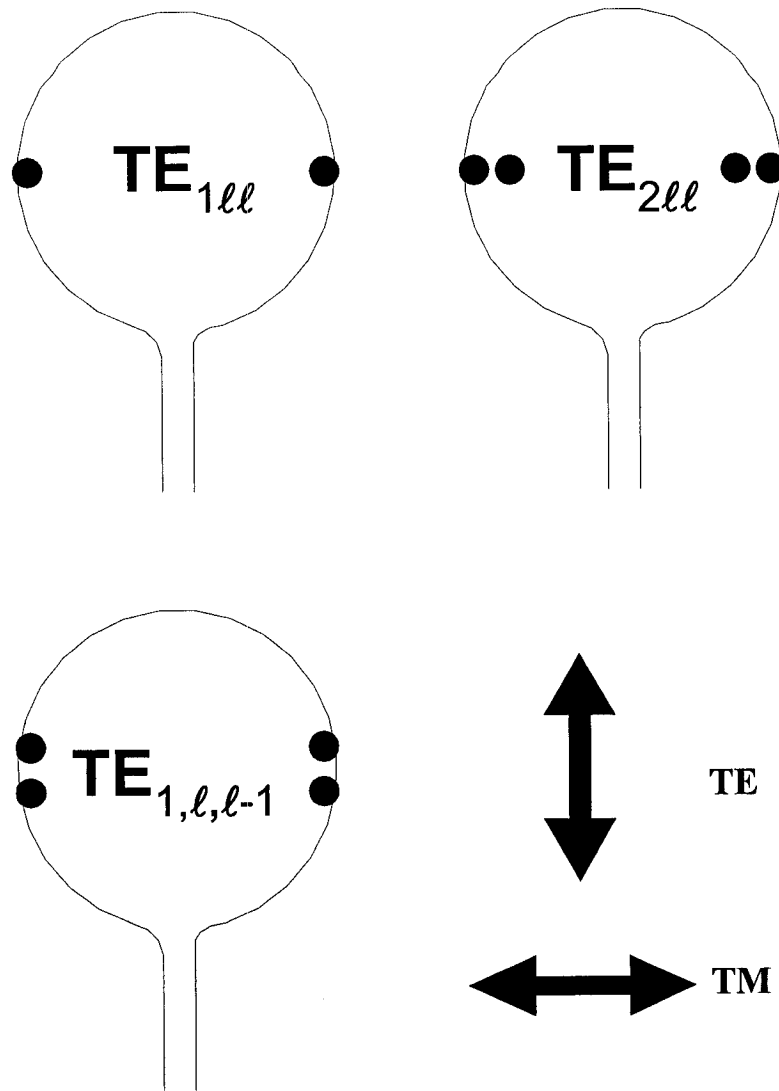


Figure II.1 Representation of the WGM structure for different mode numbers and polarization. The first index number gives the number of lobes in the radial direction, while the third index number gives the number of lobes in the latitudinal direction. The second index number roughly gives the number of wavelengths around the circumference at the equator of the microsphere. The arrows represent the direction of the electric field for the two different possible polarizations, TE or TM.

angular direction, as $\ell - |m| + 1$. A “fundamental” WGM has $\ell = |m|$ and $q = \ell$, giving one transverse maximum.

The solutions to Maxwell’s equations, for the internal electric and magnetic field components of $TE_{q\ell m}$ modes of a microsphere of radius a , satisfying the proper boundary conditions at the surface of the microsphere, are

$$\begin{aligned} E_r(r, \theta, \phi, t) &= 0 \\ E_\theta(r, \theta, \phi, t) &= -E_0 \frac{im}{\sin \theta} P_\ell^m(\cos \theta) j_\ell(k_{q\ell m}^{TE} r) e^{im\phi} e^{-i\omega_{q\ell m}^{TE} t} \\ E_\phi(r, \theta, \phi, t) &= E_0 \frac{\partial P_\ell^m(\cos \theta)}{\partial \theta} j_\ell(k_{q\ell m}^{TE} r) e^{im\phi} e^{-i\omega_{q\ell m}^{TE} t} \end{aligned} \quad (\text{II.1})$$

$$\begin{aligned} H_r(r, \theta, \phi, t) &= -E_0 \frac{\ell(\ell+1)}{i\omega_{q\ell m}^{TE} \mu_1} P_\ell^m(\cos \theta) \frac{1}{r} j_\ell(k_{q\ell m}^{TE} r) e^{im\phi} e^{-i\omega_{q\ell m}^{TE} t} \\ H_\theta(r, \theta, \phi, t) &= -E_0 \frac{1}{i\omega_{q\ell m}^{TE} \mu_1} \frac{\partial P_\ell^m(\cos \theta)}{\partial \theta} \frac{1}{r} [k_{q\ell m}^{TE} r j_\ell(k_{q\ell m}^{TE} r)]' e^{im\phi} e^{-i\omega_{q\ell m}^{TE} t} \\ H_\phi(r, \theta, \phi, t) &= -E_0 \frac{m}{\omega_{q\ell m}^{TE} \mu_1} \frac{P_\ell^m(\cos \theta)}{\sin \theta} \frac{1}{r} [k_{q\ell m}^{TE} r j_\ell(k_{q\ell m}^{TE} r)]' e^{im\phi} e^{-i\omega_{q\ell m}^{TE} t} \end{aligned} \quad (\text{II.2})$$

and the internal electric and magnetic field components of $TM_{q\ell m}$ modes are:

$$\begin{aligned} E_r(r, \theta, \phi, t) &= -E_0 \ell(\ell+1) P_\ell^m(\cos \theta) \frac{j_\ell(k_{q\ell m}^{TM} r)}{k_{q\ell m}^{TM} r} e^{im\phi} e^{-i\omega_{q\ell m}^{TM} t} \\ E_\theta(r, \theta, \phi, t) &= -E_0 \frac{\partial P_\ell^m(\cos \theta)}{\partial \theta} \frac{1}{k_{q\ell m}^{TM} r} [k_{q\ell m}^{TM} r j_\ell(k_{q\ell m}^{TM} r)]' e^{im\phi} e^{-i\omega_{q\ell m}^{TM} t} \\ E_\phi(r, \theta, \phi, t) &= -E_0 \frac{im P_\ell^m(\cos \theta)}{\sin \theta} \frac{1}{k_{q\ell m}^{TM} r} [k_{q\ell m}^{TM} r j_\ell(k_{q\ell m}^{TM} r)]' e^{im\phi} e^{-i\omega_{q\ell m}^{TM} t} \end{aligned} \quad (\text{II.3})$$

$$\begin{aligned}
E_r(r, \theta, \phi, t) &= 0 \\
E_\theta(r, \theta, \phi, t) &= -E_0 \frac{k_{q\ell m}^{TM}}{\omega_{q\ell m}^{TM} \mu_1} \frac{m P_\ell^m(\cos \theta)}{\sin \theta} j_\ell(k_{q\ell m}^{TM} r) e^{im\phi} e^{-i\omega_{q\ell m}^{TM} t} \\
E_\phi(r, \theta, \phi, t) &= E_0 \frac{k_{q\ell m}^{TM}}{i\omega_{q\ell m}^{TM} \mu_1} \frac{\partial P_\ell^m(\cos \theta)}{\partial \theta} j_\ell(k_{q\ell m}^{TM} r) e^{im\phi} e^{-i\omega_{q\ell m}^{TM} t}
\end{aligned} \tag{II.4}$$

where E_0 is the electric field, the P_ℓ^m are the associated Legendre polynomials, j_ℓ are the spherical Bessel functions of the first kind, $k_{q\ell m}^{TE(M)} = \frac{n_s \omega_{q\ell m}^{TE(M)}}{c}$, μ_s is the permeability of the microsphere, and the prime denotes the derivative with respect to the argument $k_{q\ell m}^{TE(M)} r$. The external field components can be expressed by replacing $k_{q\ell m}^{TE(M)} r$ by $K_{q\ell m}^{TE(M)} r$, $j_\ell(k_{q\ell m}^{TE(M)} r)$ by the spherical Hankel function $h_\ell^{(1)}(K_{q\ell m}^{TE(M)} r)$, and μ_s by μ_a , where the wave number written in upper case, representing the value outside the microsphere, is $K_{q\ell m}^{TE(M)} = k_{q\ell m}^{TE(M)} / n$, where $n = n_s / n_a$ is the ratio of the index of refraction of the microsphere to that of the medium surrounding it.

The WGM resonance frequencies can be written as

$$\nu_{q\ell m}^{TE(M)} = \frac{\omega_{q\ell m}^{TE(M)}}{2\pi} = \delta(\ell + 1/2 + a_q) \left(\frac{\ell + 1/2}{2} \right) - \Delta^{TE(M)} \pm \varepsilon^2 \left(\frac{\ell - |m|}{2} \right) + \frac{3a_q^2}{2^{2/3} 10 (\ell + 1/2)^{1/3}}, \tag{II.5}$$

where $\delta = c/2\pi a n_s$ is the microsphere's nominal free spectral range, a_q is the q^{th} zero of the Airy function ($a_1 = 2.338$, $a_2 = 4.088$, $a_3 = 5.521$, $a_4 = 6.787$, etc.), $\Delta^{TE} = n / \sqrt{n^2 - 1}$ and $\Delta^{TM} = (n\sqrt{n^2 - 1})^{-1}$ is a polarization dependent frequency shift, $\varepsilon = \sqrt{(a_+^2 - a_-^2) / a_+^2}$ is the eccentricity in terms of the major and minor radii, the upper sign is used for oblate spheroids and the lower sign for prolate spheroids. Using the hydrogen-oxygen torch to fabricate a microsphere usually results in a prolate shape. This eccentricity lifts the

frequency degeneracy of the latitudinal modes.

An excellent experimental example that shows the spectrum of the WGMs and how polarization and mode number lift their frequency degeneracy is presented in Figure II.2. The top curve in each plot is the reflection signal obtained using prism coupling and the bottom curve is the transmission signal that was collected with a single tapered fiber, where the scales are not the same for the two signals. The large oscillations in the reflection signal are caused by a Fabry-Perot effect from an uncoated window. This is verified by the fact that the period of the laser power oscillation is 10 GHz, which corresponds to Fabry-Perot effects from the 1-cm thick window that was in the beam path. Figure II.2 (a) is a scan over approximately two free spectral ranges (FSR) of the microsphere, where the FSR is measured to be 140 GHz. This corresponds to a microsphere diameter of approximately 480 μm . Many higher order modes are also present in one FSR. Reducing the scan range in Figure II.2 (b) allows for observation of a smaller region of plot (a) in order to show the structure and spacing between the higher order modes. Here, two sets of equally spaced modes interlaced with each other are observed. The equally spaced modes are assumed to belong to a family of modes that have the same polarization and ℓ -mode number with different m -mode numbers. The two different families of modes are different due to fact that they have different polarizations or q -mode numbers. Measuring the spacing between the modes of the same family to be 4.8 GHz gives an eccentricity of $\varepsilon = 0.26$. Further reduction of laser scan distance in Figure II.2 (c) reveals the lineshape of two individual WGMs. As will be shown later in this chapter, the reflection and transmission lineshapes are both Lorentzian in nature.

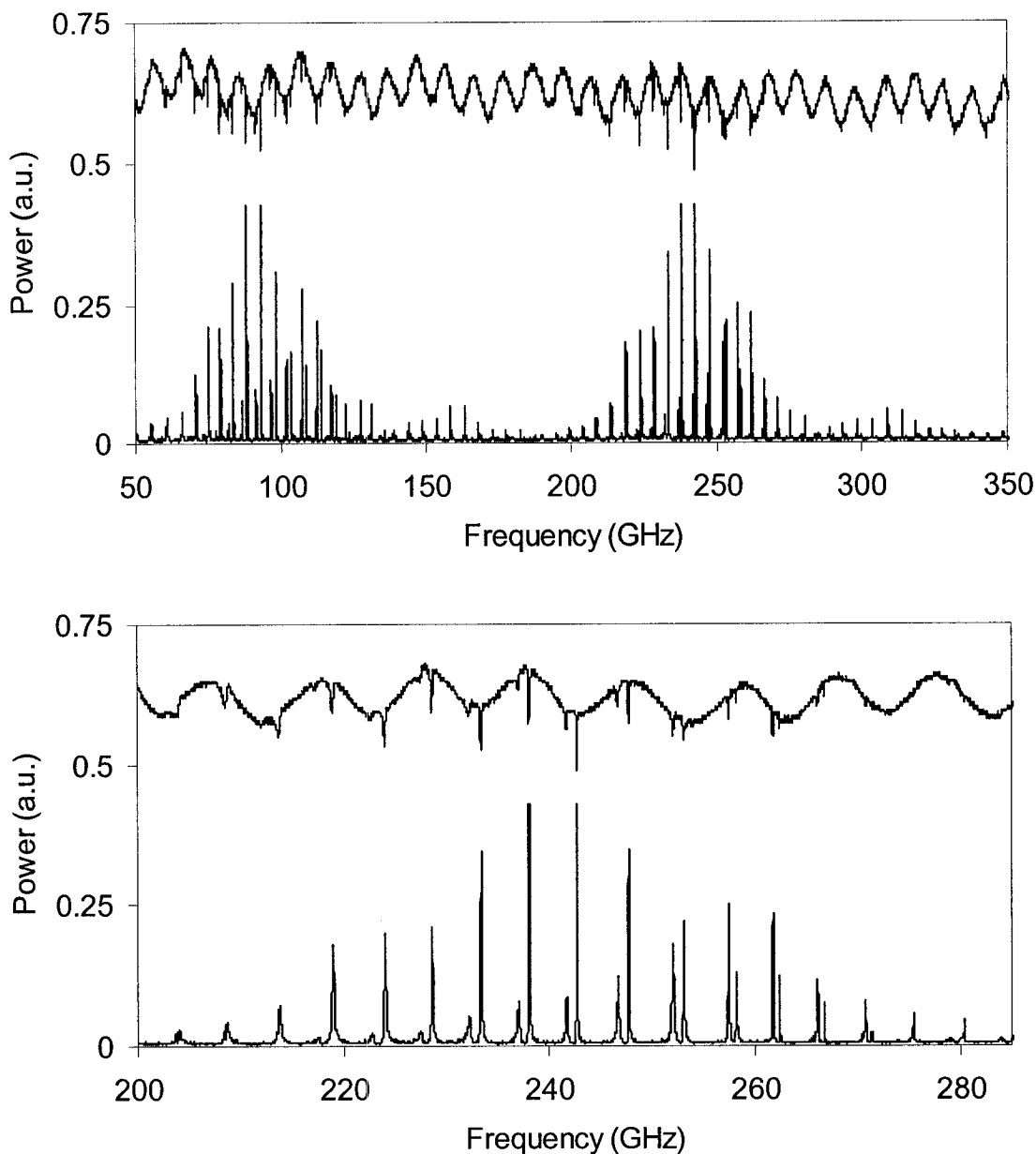


Figure II.2 Top curve in each plot is the reflection signal using prism coupling. Bottom curve is the transmission signal collected with a single tapered fiber. The scale is not the same for the reflection and transmission signals. The large oscillations in the reflection signal are caused by a Fabry-Perot effect from an uncoated window. a) Scan over the two free spectral ranges of the microsphere. Many higher order modes are present. b) Scan over a smaller region of plot (a) in order to show the spacing and structure between the higher order modes. c) (Shown on next page) Further reduction in laser scan distance to show the lineshape of individual WGMs.

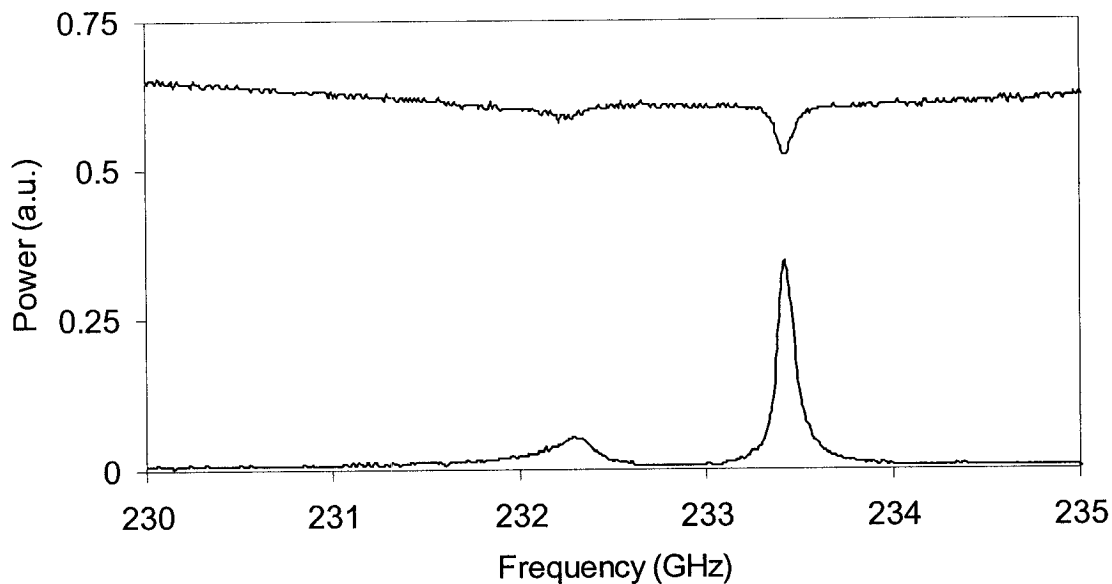


Figure II.2 c) Described on previous page.

2. Ring Cavity Model

(a) Theory

When examining the electric field and intensity there are three main areas of interest pertaining to the microsphere: (1) The point where the light exiting the microsphere is the same as where the incident light enters the microsphere, referred to as the reflected light or microsphere reflection, (2) inside the cavity, (3) a point where the light exiting the microsphere is other than point (1), referred to as the transmitted light or microsphere transmission.

A simple model of the energy coupled in and out of microspheres is constructed using a simple four-mirror ring cavity as shown in Figure II.3. The model cavity is designed using four flat mirrors, each associated with an electric field reflection coefficient ($\Gamma_{1,2,3,4}$). Although the microsphere confines the WGMs with its curved surface, using curved mirrors in the model will not add any significant results while

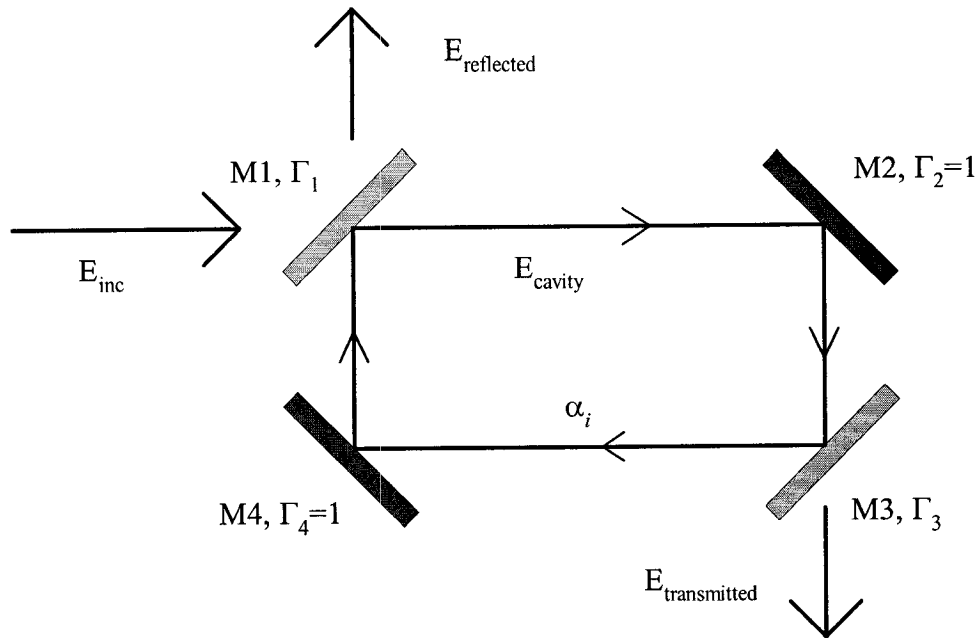


Figure II.3 Model of four-mirror ring cavity. Mirror 1 (M1) is the input mirror and has a reflectivity slightly less than 1. M2 and M4 are assumed perfect reflectors, while M3 can be a high reflector or another output mirror. The loss coefficient (α_i) is constant throughout the path length. The electric fields are labeled at the points of interest.

increasing the complexity. There is only one transverse mode of this plane-wave cavity, the fundamental mode, but the model is applicable to any mode of a microsphere. The external electric field source is partially transmitted through mirror number one (M1) and is assumed to be a uniform plane wave with a limited spatial dimension transverse to the propagation direction.

The incident electric field, E_{inc} , is assumed monochromatic, of frequency $\nu = \omega/2\pi$ and vacuum wavelength λ . The strength of the field transmitted into the cavity, E_0 , is dependent on Γ_1 and is related to E_{inc} by

$$E_0 = E_{inc} \sqrt{1 - \Gamma_1^2} \quad (II.6)$$

As the light propagates a distance equal to one round trip inside the cavity, it

encounters losses from mirror transmissions, cavity medium absorption, scattering, and other less significant losses. This is unlike a conventional resonator in the sense that the intrinsic cavity losses cannot be neglected. The light also undergoes a phase shift due to reflections, with the end result that at M1, the reflected incident light and the light exiting the cavity are out of phase by π (180 degrees) on resonance.

The field inside the cavity can be described by summing the field remaining after each successive round trip. The electric field strength and phase after $m+1$ round trips is compared to the m^{th} round trip by

$$E_{m+1} = E_m \Gamma_1 \Gamma_2 \Gamma_3 \Gamma_4 e^{\frac{-\alpha_i L}{2}} e^{iLk}, \quad (\text{II.7})$$

where L is the physical round trip length, not the optical path length, $k = \omega n_{\text{eff}}/c$ is the wave number, n_{eff} is the effective index of refraction of the cavity, and $\alpha_i = \alpha_{\text{abs}} + \alpha_{\text{scat}}$ is the absorption and scattering loss coefficient combined into one intrinsic loss term.

At this point, it is advantageous to simplify the mirror losses. Assume that two of the mirrors, Γ_1 and Γ_3 , are partially transmitting and the other mirrors are 100% reflective, i.e. $\Gamma_2 = \Gamma_4 = 1$. This is analogous to a microsphere with two couplers. Both mirrors couple out of the microsphere, but only one has incident power coupling into the microsphere. If Γ_3 is also equal to one, this is analogous to a single coupler coupling light in and out of the microsphere.

The total field inside the cavity immediately after M1 becomes

$$E_{\text{int}} = \sum_{m=0}^{\infty} E_m = \frac{(1 - \Gamma_1^2)^{\frac{1}{2}}}{1 - \Gamma_1 \Gamma_3 e^{\frac{-\alpha_i L}{2}} e^{iLk}} E_{\text{inc}}. \quad (\text{II.8})$$

As the field exits the cavity at M1 it combines with the light that is reflected from M1.

Assuming reflection coefficients near unity and a π phase shift between the two fields on resonance, summing gives the total electric field reflected

$$E_{reflected} = \frac{\Gamma_1 - \Gamma_3 e^{\frac{-\alpha_i L}{2}} e^{iLk}}{1 - \Gamma_1 \Gamma_3 e^{\frac{-\alpha_i L}{2}} e^{iLk}} E_{inc}. \quad (\text{II.9})$$

The electric field in the cavity, immediately before M3, and the electric field transmitted through the cavity, out M3 are respectively

$$E_{cavity} = \frac{\left(1 - \Gamma_1^2\right)^{\frac{1}{2}} e^{\frac{-\alpha_i L}{4}} e^{i\frac{Lk}{2}}}{1 - \Gamma_1 \Gamma_3 e^{\frac{-\alpha_i L}{2}} e^{iLk}} E_{inc}, \quad (\text{II.10})$$

$$E_{transmitted} = \frac{\left(1 - \Gamma_1^2\right)^{\frac{1}{2}} \left(1 - \Gamma_3^2\right)^{\frac{1}{2}} e^{\frac{-\alpha_i L}{4}} e^{i\frac{Lk}{2}}}{1 - \Gamma_1 \Gamma_3 e^{\frac{-\alpha_i L}{2}} e^{iLk}} E_{inc}. \quad (\text{II.11})$$

Optical detectors perform the task of making physical measurements of radiation, measuring the power or intensity of light radiation and not the strength of the electric field. The intensity is related to the electric field by

$$I = \frac{1}{2\eta} |E|^2, \quad (\text{II.12})$$

where $\eta = 1/n_{eff} \epsilon_0 c$ is the wave impedance. Using equation (II.12) and a few approximations to be described below, the reflection, intracavity, and transmission intensities become respectively,

$$I_{reflected} = \frac{(T_1 - T_3 - \alpha_i L)^2 + 4\phi^2}{(T_1 + T_3 + \alpha_i L)^2 + 4\phi^2} I_{inc}, \quad (\text{II.13})$$

$$I_{cavity} = \frac{4T_1}{(T_1 + T_3 + \alpha_i L)^2 + 4\phi^2} I_{inc}, \quad (\text{II.14})$$

$$I_{transmitted} = \frac{4T_1T_3}{(T_1 + T_3 + \alpha_i L)^2 + 4\phi^2} I_{inc}. \quad (\text{II.15})$$

The following definitions are employed when writing these results,

$$T_x = 1 - \Gamma_x^2 \quad (\text{II.16})$$

$$\text{and } \phi = L(k - k_0), \quad (\text{II.17})$$

where T_x is the intensity transmission coefficient of mirror Mx and ϕ is the round trip phase shift relative to that of a resonance (mode) of wave number k_0 and frequency ν_0 . From this point on, the term transmission coefficient will refer to the intensity transmission coefficient unless otherwise stated. The approximations made assume that the loss per round trip due to absorption ($\alpha_{abs}L$) and scattering ($\alpha_{scat}L$), the transmission coefficients (T_x), and $\phi/2\pi$ are all very small compared to 1. Making the assumption that ϕ is small implies that the frequency detuning of the light from cavity resonance is much less than one FSR. All of these assumptions are extremely valid for the microsphere.

Equation (II.14) gives an intracavity enhancement factor

$$\frac{4T_1}{(T_1 + T_3 + \alpha_i L)^2 + 4\phi^2} \quad (\text{II.18})$$

that determines the intensity inside the cavity compared to the incident intensity. This factor is important when determining loss coefficients and nonlinear effects. It can also be used to define the intracavity path length, which is associated with the power lost due to the intrinsic loss of the microsphere. This path length is defined as the resonant intracavity enhancement times the round trip distance,

$$L_{loss} = \frac{I_{cavity}}{I_{inc}} L = \frac{4T_1 L}{(T_1 + T_3 + \alpha L)^2} = \frac{T_1}{L} \left(\frac{Q\lambda}{\pi n_{eff}} \right)^2. \quad (\text{II.19})$$

The quality factor (Q) of the cavity can be determined from equations (II.13)-(II.15). The linewidth of the cavity, $\Delta\nu = \nu_+ - \nu_-$, must be found since it is related to Q by

$$Q = \frac{\nu}{\Delta\nu}. \quad (\text{II.20})$$

ν_+ and ν_- are the frequency values when the intensity dip or peak is one-half of the maximum dip or peak value. Using equation (II.13) to illustrate this,

$$\frac{I_{inc} - I_{reflected}(\phi)}{I_{inc} - I_{reflected}(\phi = 0)} = \frac{1 - \frac{x^2 + 4\phi^2}{y^2 + 4\phi^2}}{1 - \frac{x^2}{y^2}} = \frac{y^2}{y^2 + 4\phi^2} = \frac{1}{2}, \quad (\text{II.21})$$

where $x = T_1 - T_3 - \alpha L$ and $y = T_1 + T_3 + \alpha L$. As expected, the same functional form as the last equality in equation (II.21) comes about when using the peaks of equations (II.14) and (II.15). Notice this result is independent of the definition of x and depends only on y and ϕ . This equality yields

$$\phi_{\pm} = \frac{2\pi n_{eff} L (\nu_{\pm} - \nu_0)}{c} = \pm \frac{1}{2} (T_1 + T_3 + \alpha_i L). \quad (\text{II.22})$$

Solving for $\Delta\nu$ and writing α_i explicitly as the sum of the absorption and scattering coefficients, the Q of the cavity can most conveniently be expressed in the form

$$\frac{1}{Q} = \frac{\lambda T_1}{2\pi n_{eff} L} + \frac{\lambda T_3}{2\pi n_{eff} L} + \frac{\lambda \alpha_{abs} L}{2\pi n_{eff} L} + \frac{\lambda \alpha_{scat} L}{2\pi n_{eff} L} \quad (\text{II.23})$$

$$\text{or } \frac{1}{Q} = \frac{1}{Q_{T_1}} + \frac{1}{Q_{T_3}} + \frac{1}{Q_{abs}} + \frac{1}{Q_{scat}} + \left(\frac{1}{Q_{rad}} \right). \quad (\text{II.24})$$

Q_{rad} is not derived here, but is the radiation loss due to photon tunneling from the whispering-gallery mode into free space. It is many orders of magnitude larger than any

of the other Q terms, unless working with spheres that are comparable to the size of the wavelength, and is therefore negligible in this work. When written in this form, Q can be separated into the Q due to coupling, Q_{T_1} and Q_{T_3} , and the intrinsic Q of the cavity, $(Q_{abs}^{-1} + Q_{scat}^{-1})^{-1}$. The intrinsic Q , Q_i , is the Q value of the cavity with no external losses, namely no coupling losses. This value is important when performing absorption measurements for intracavity trace gas and liquid chemical sensing.

The lineshape of the dip from the reflection spectrum is one minus a Lorentzian function. This can be seen by rewriting equation (II.13) as

$$I_{reflected} = \left(1 - M \frac{\left(\frac{\Delta\phi}{2} \right)^2}{\left(\frac{\Delta\phi}{2} \right)^2 + \phi^2} \right) I_{inc} \quad (\text{II.25})$$

where $\Delta\phi = \phi_+ - \phi_-$ is the linewidth that is obtained from equation (II.22) and M is the normalized on-resonance dip depth given by

$$M = \frac{T_1(T_3 + \alpha_i L)}{\left(\frac{T_1 + T_3 + \alpha_i L}{2} \right)^2}. \quad (\text{II.26})$$

In a similar fashion, the intracavity and transmission intensities can be written as Lorentzian functions.

(b) Solutions and Physical Interpretation

In the ring cavity model, there are three unknowns that cannot be directly measured or inferred. The wavelength can be measured with a monochromator, the path length can be estimated with minimal uncertainty, and the index of refraction of fused silica is easily obtainable from the literature. T_1 , T_3 , and α_i are dependent on the physical

parameters of the experimental setup and can vary by several orders of magnitude. For microspheres, variables such as gap distance between the coupler and microsphere, surface roughness, and contaminants such as water and dust deposited on the surface of the microsphere are not always easily measurable or controllable. By using the maximum dip depth of the reflection, the maximum transmission value, and the Q value with equations (II.13), (II.15), and (II.23) these three values can be determined. However, it is easily noticed that the equations contain quadratics and will give two separate solutions. The cases for the possible solutions are discussed below.

At “critical coupling” the maximum (on resonance) dip depth, 100%, occurs when the light leaving the cavity at M1 is equal to the reflected light not entering the cavity at M1. The lack of signal arises from the fact that the two are out of phase with each other by π and destructively interfere. In terms of the coupling and loss coefficients, critical coupling occurs when $T_1 = T_3 + \alpha_i L$. When $T_1 > T_3 + \alpha_i L$ the cavity is said to be “overcoupled”. In the overcoupled case, the light leaving the cavity at M1 is more intense than the reflected light not entering the cavity at M1. When $T_1 < T_3 + \alpha_i L$ the cavity is said to be “undercoupled”. Conversely, in the undercoupled case the light leaving the cavity at M1 is less intense than the reflected light not entering the cavity at M1. Given the same cavity Q , the intracavity intensity is higher in the overcoupled case.

Empirical observations suggest it is more likely to achieve overcoupling with tapered fiber coupling than with prism coupling when exciting whispering-gallery modes in a microsphere. Determining if a microsphere is overcoupled or undercoupled is possible with ring-up/ring-down measurements, which are not described in this dissertation.

It is interesting to note that in all of the three cases listed above, the intensity inside the cavity is never zero, and the light transmitted through the cavity is only zero if T_3 is zero. In addition, the transmission is maximum, 100%, only when there is no intrinsic loss and $T_1 = T_3$. Such an observation places limitations on transmission intensity and is very important when examining the potential of microspheres as add/drop filters for fiber optic applications.

Equation (II.19) shows that of the two possible solutions for a given Q and dip depth, the overcoupled case has a longer intracavity path length than the undercoupled case. The total power lost is the same for each case, with the difference in intracavity path lengths attributed to more power being coupled into the cavity for the overcoupled case. This is also seen in the fact that the overcoupled case has a smaller loss coefficient than the undercoupled case for the same Q and dip depth.

Other factors not included in this model that must be taken into account when analyzing real data include polarization, mode matching characteristics, and the tapered fiber mode coupling which is presented in the next chapter and leads to the modified ring cavity model in the Appendix. This statement becomes evident when looking at the data for the intracavity absorption sensing data in Chapter VI.

CHAPTER III

GENERAL EXPERIMENTAL PROCEDURES

1. Introduction

Many of the experiments presented in this dissertation have common elements. For example, they all contain microspheres, lasers, and optical fibers and they all use some form of evanescent coupling. This chapter serves as a basis for the experimental methods and techniques used for all the experiments presented here, as well as most, if not all, of the microsphere experiments performed in the lab.

Microsphere fabrication can be quite difficult at times and has been described as “an art form” on several occasions. In this chapter, the general methodology of both microsphere and tapered fiber fabrication is described along with properties of tapered fiber transmission. Prism and fiber coupling techniques are reviewed. Two tunable lasers are used to excite the WGMs: a cw Ti:sapphire laser in the 770-860 nm wavelength range and a diode laser in the 1508-1584 nm range. Basic assumptions about laser tuning rates and linearity, especially with the tunable diode laser (TDL), have proven to be a source of error on a number of occasions. Therefore, basic laser specifications and properties that are relevant to data interpretation are included in this chapter. To demonstrate the experimental limits imposed by the lasers and tapered fibers, the coupling properties of a single WGM are examined as the gap distance between the microsphere and coupler is varied.

2. Microsphere Fabrication

Generally speaking, microspheres have been fabricated from many different materials, including liquid droplets,^[17] polystyrene,^[18] LiNbO₃,^[19] and fused silica.^[20] When ultra-high Q factors are necessary, microsphere cavity losses must be minimized. This makes fused silica ideal for working in the visible and near infrared region of the spectrum, with its very small optical loss in this range.^[21] It also has the benefit of being abundant and easy to work with. The telecommunications industry must be acknowledged for the extensive development of low loss, low OH, fused silica optical fibers. The optical loss in fused silica is primarily due to Rayleigh scattering, followed by absorption. A few values of the total loss, for wavelength regions accessible by the lasers used for these experiments, are listed in Table III.1. Typically, the absorption loss will be less than 15% of the total loss. The scattering loss of the material is not to be confused with the surface scattering that a microsphere also experiences, but rather the Rayleigh scattering of the material.^[22] Likewise, the absorption is the intrinsic ultraviolet, infrared, and impurity absorption of fused silica, not that from impurities or water on the surface of a microsphere. The power absorbed in the thermal bistability experiments in Chapter V is attributed to the surface absorption, not the material absorption.

Table III.1 Loss coefficient of fused silica at selected wavelengths

Wavelength (nm)	Total Loss (m ⁻¹) ^{[21],[23]}
830	4.6×10^{-4}
1500	6.9×10^{-5}
1550	5.06×10^{-5}
1600	5.8×10^{-5}

For the experimental work performed in this dissertation, the fused silica was obtained from Corning single mode optical fiber, SMF-28. Hence, throughout this dissertation, the term “microsphere” implies a microsphere fabricated from single mode optical fiber. It is clearly visible during fabrication that the fiber core remains confined to the center and polar regions of the microsphere. The difference in index of refraction causes the core to appear brighter than the cladding when heated to the melting temperature. Therefore, the WGMs, which are confined near the surface of the equatorial region, are not affected by the difference between the index of refractions of the core and cladding.

The microspheres are typically fabricated by melting the fused silica fiber with a hydrogen-oxygen (H-O) torch^[24, 25] or with a CO₂ laser.^[26-28] The H-O torch is the only method used for the research presented in this dissertation. The torch used is a commercially available jeweler’s torch with a gas hole diameter of approximately 250 μm . The compressed hydrogen and oxygen gases are purchased from Sooner Airgas, a commercial supplier. During fabrication, the microsphere is observed through a 25-mm focal length lens or a 45 \times microscope.

To prepare the fiber for microsphere fabrication, the plastic jacket surrounding the fiber must be stripped away. Following this, the bare fiber is cleaned with methanol to remove the majority of surface contaminants. The 125- μm fiber diameter is sufficient for producing microspheres of diameter 300 μm or more. If smaller microspheres are needed or a smaller stem diameter is required, the fiber is drawn out with the H-O torch to a smaller diameter. The prepared fiber is inserted perpendicularly into the flame to form the microsphere. This results in a 90-degree bend, where the bent portion becomes the

microsphere and stem, and the non-bent portion is used for mounting. The torch's gas flow rate controls the amount of upward pressure on the forming microsphere. Adjusting the pressure can cause the microsphere to draw out and thin the stem or cause it to consume part of the stem below it. Changing the gas flow rate during fabrication gives control over the microsphere and stem size. Additionally, the H-O ratio controls the temperature of the flame, producing flames that are hotter or colder. Adjusting these parameters and the position of the microsphere in the flame controls the size of the stem, and the shape and orientation of the microsphere.

During fabrication, surface tension pulls the molten silica into a nearly perfect sphere with an extremely smooth surface.^[29, 30] The gas rushing past the microsphere generally causes it to be prolate, with a different resulting eccentricity for each microsphere. A result of this is a different WGM mode spectrum for every microsphere. Reported eccentricities (ϵ) by other research groups include 0.01,^[31] 0.16,^[32] and 0.26.^[13] Examples of typical microsphere eccentricities in our lab, where no special care has been taken to minimize the eccentricity, can be seen from the microsphere spectrum in Chapter II, 0.26, and from the two microspheres used for thermal experiments in Chapter V, 0.45 and 0.65. It has been demonstrated by Ilchenko, et al. that by making the microspheres extremely oblate, the dense spectrum of modes is reduced to as little as two modes per nominal free spectral range with a Q of 1×10^7 at 1550 nm.^[33] The fabrication method involved appears to be difficult and requires the use of a CO₂ laser and low-melting silica glass held between two cleaved fibers.

Another possible method of removing excess modes from the spectrum of a WGM microresonator is to use a cylinder rather than a sphere. Using optical fibers as

cylinders, preliminary studies have been performed to assess the feasibility of using these modes. The plastic jacket was removed from the fiber by soaking the fiber in acetone until it was soft enough to be gently pulled off. This ensured that no unnecessary scratches were introduced by the normal metal stripping tool. The stripped fiber was wiped with acetone, followed by methanol. The best results with bi-tapered fiber coupling, with the two fibers in contact, gave a Q of 5×10^6 . A periodic mode spectrum of only two modes per free spectral range per polarization was found, presumably modes of different radial number. Heating the cylindrical fiber and stretching it to a small diameter proved unsuccessful, but slightly heating the surface yielded higher Q values of 1×10^7 , and significantly increased the number of modes excited. The extra modes are assumed to be a product of a slight curvature of the fiber surface, making it act as an extremely prolate microsphere. The deepest dip depths observed were approximately 30%, but a detailed study of under/overcoupling and maximization of the dip depth was not performed. These cylinder WGMs have the potential to be used as add/drop filters and spectral analysis devices.

Using the fabrication technique described above for nearly spherical microspheres, Q values of up to 5×10^8 at 830 nm and 5×10^7 at 1550 nm were achievable with bi-tapered fiber coupling techniques, where the fiber was in contact with the microsphere. Taking into account loss due to water adsorbed on the surface of the microsphere, these values are only an order of magnitude lower than some of the highest Q s recorded where prism coupling is employed and careful gap separation is needed to minimize coupling losses.^[26, 29, 30] In at least some of these cases, steps not taken in our lab have been used to ensure ultra-high Q s.^[25] These steps include special cleaning

methods for the fused silica before microsphere fabrication and using a dry box to contain the torch and sphere. Additionally, at least two of the research groups, those of Kimble and Ilchenko, use low O-H fused silica obtained directly from manufacturers to which they apply the cleaning techniques to remove surface contaminants.^[34]

Microsphere fabrication with a CO₂ laser was attempted on several occasions by placing the fiber in the beam path near a focal point. The fiber tip was introduced perpendicularly into the beam. With a very high absorption coefficient in the 10- μ m wavelength range, the power was readily absorbed by the fused silica fiber. Too readily in fact, resulting in uneven heating of the fiber and causing the melting fiber to be pulled towards the direction of the incident beam. Functional microspheres were created using this technique, but the procedure was more difficult than the H-O torch method. Controlling the size and shape of the microsphere was not possible, and therefore was not pursued further. Other research groups have developed better methods of creating microspheres with CO₂ lasers. These include placing the microsphere at the focal points of counter-propagating beams,^[26-28] and placing the fiber lengthwise into a strongly focused beam so the intensity is only high enough to melt the fiber near the focal point.^[27]

3. Coupling Techniques

Coupling techniques include the use of prisms^[13, 20, 26, 29-31, 35, 36], tapered fibers,^[5, 18, 37-40] half-block couplers,^[41, 42] angle-polished fibers,^[43, 44] and silica-based strip-line pedestals antiresonant reflecting waveguides (SPARROW).^[16, 45] Prism and tapered fiber coupling are the two most popular coupling methods due to ease of construction and use.

Both use evanescent coupling to the microsphere WGMs and both have advantages and disadvantages. The ease of use of the fiber coupling technique while maintaining relatively high Q values has moved more of our experiments in this direction. Although almost all of the experiments in this dissertation use fiber coupling, both methods have been used in the lab and both will be described.

Figure III.1 shows a diagram of prism and fiber coupling and Table III.2 is a comparative list of some of the properties for each. The reflection spectrum can be observed by using only one prism or fiber. By bringing a second prism or fiber next to the microsphere on the opposite side (any combination will work) the transmission spectrum can be observed. Using a single prism as a coupler has the advantage that both the reflection and transmission spectrum can be observed with precessing modes.^[31] With reflection, the WGM signal dip must be compared to the off-resonance signal, making shallow dips on the order of a percent hard to detect. The advantage of the transmission spectrum is that the signal to noise ratio is small, where the WGMs are detected as peaks with no background. Since there is no background signal, the limit of the detectable transmission signal is determined by the detector. The disadvantages of using a second coupler are limited access to the microsphere, increased complexity, and a smaller Q from the extra loss. It should also be noted that precessing modes also have losses from the reflected and transmitted signals, but a single gap distance can control the intracavity loss from both.

During prism coupling, light undergoes total internal reflection (TIR) off a face of the prism creating an evanescent field at the point of reflection. When this overlaps with

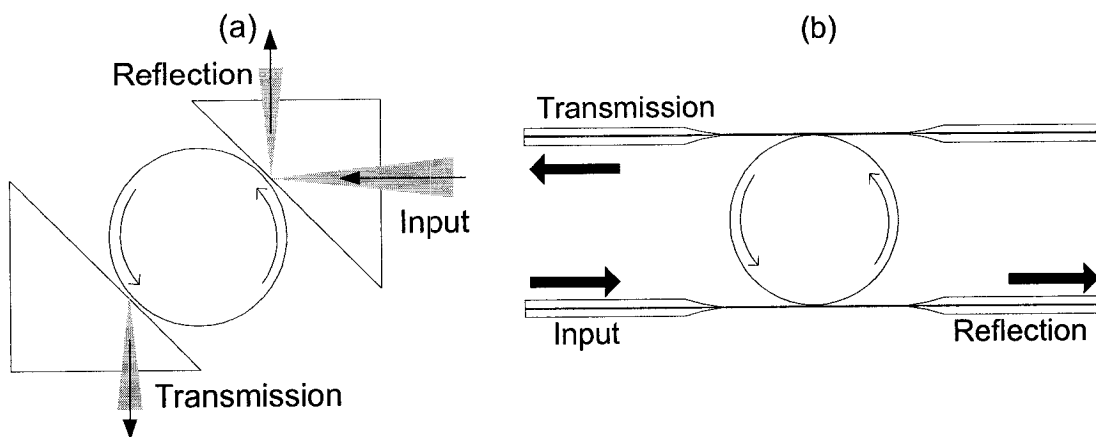


Figure III.1 Input and output coupling to a WGM using (a) prisms and (b) tapered fiber coupling, demonstrating reflection and transmission signals.

Table III.2 Summary of prism and fiber coupling properties.

Prism Coupling	Tapered Fiber Coupling
Alignment of incident angle in two directions. Beam waist must be positioned correctly.	Fiber taper need only be aligned with the equator of the microsphere.
Visual inspection of the TIR spot is necessary. Difficult in the 1500 – 1600 nm range.	Visual inspection of fiber position is necessary. This can be done at any wavelength.
Reflection and transmission are observed with one prism for precessing modes.	Need two fibers to observe transmission signals.
Polarization controlled by half waveplates and polarizers in the beam path.	An inline fiber polarization controller easily changes polarization.
Collecting all the light is more difficult.	Light collection is easy at the fiber end.
All of the light reflected is available for collection.	Light can be lost to other fiber modes in fiber taper region. (See Appendix)
Reflected signal can never go to zero.	Reflected signal can go to zero.
Adjusting the gap distance between the prism and microsphere changes the transmission coefficient (T_I).	Adjusting the taper diameter and gap distance changes the transmission coefficient (T_I).
Alignment issues make it hard to integrate into systems.	Easily integrated into current fiber optic systems.

the evanescent field of a WGM, coupling light in and out of the microsphere is possible.

Mode matching the evanescent beam with the WGM evanescent field is necessary in order to couple light into the microsphere efficiently. This includes both spatial mode matching and phase matching. Spatial mode matching can be maximized by using mirrors and lenses to control the alignment of the incident beam angle in both the horizontal and vertical planes, as well as ensuring the focused beam waist is incident on the prism face at the TIR point. The equations for the angle parameters are given in Reference [31]. In short, they predict that in order to excite the lowest order WGMs, the incident angle at the prism coupling face should be close to the critical angle between the prism and microsphere.

For a given microsphere WGM and prism, phase matching is controlled at the TIR point of the prism by adjusting the angle of the incident beam.^[46] In terms of ray propagation, there are an infinite number of incident angles within a focused beam, making perfect phase matching using a prism and lens impossible. The deepest dips recorded in our lab with prism coupling are 40%. The maximum recorded dip depth with prism coupling, where measures were taken to maximize the mode matching, is 80%.^[36] Here, the main mode matching optimization was the minimization of astigmatic distortions of the input beam. Imperfect mode matching results in the reflected signal not going to zero at critical coupling, leaving some offset value that must be accounted for when using the dip depth and Q to determine the intrinsic loss of the microsphere.

After the WGM spectrum has been found and maximized, the microsphere is backed away from the prism to reduce the coupling loss.^[36] This causes the dip depth to change and the Q to increase. In the literature where extremely high Q values are

recorded,^[30] the microsphere is not allowed to contact the prism and measurements are performed in the first minute after fabrication, before water can adsorb to the microsphere surface.

In our lab, a short focal length aspherical lens is used in order to obtain a smallest possible spot size. The short focal length is necessary since the spot size is proportional to the focal length, and the asphere is used to avoid spherical aberration. This means shortly after the prism another lens is needed to collimate the beam for detection before it expands to a size that is too large to collect. Due to imperfect mode matching, the reflected intensity pattern from the microsphere is not uniform over the entire beam. Therefore, the entire beam must be collected for detection to get the true WGM spectrum. Additionally, precessing mode output with a single prism has both transmission and reflection signals that should be separated from each other.

4. Tapered Fiber Fabrication and Coupling

Using tapered fibers for evanescent coupling to microspheres has the advantage of ease of coupling over the prism setup. To employ fiber coupling the tapered fiber must be placed near (a fraction of a wavelength) or in contact with a microsphere. To avoid back reflection into the laser from the fiber face, an optical isolator is used or the fiber face is angle polished. Coupling light into the fiber is almost trivial and so is aligning the fiber and microsphere. Alignment is aided by use of a 45× microscope, or in some cases a biological microscope with magnifications of 100×, 200×, 400×, and 1000×. Creating a taper with optimal parameters for coupling is more difficult. If the taper is too thick, there will be no coupling to the microsphere. As the taper diameter is reduced, the

effective coupling coefficient T_l becomes larger, reducing the loaded Q value and making overcoupling a possibility.

Mode matching must be considered for tapered fiber coupling as well. Coupling between the tapered fiber and the microsphere is similar to that between any two waveguides. The advantage of fiber coupling over prism coupling is that there are not an infinite number of wave vector values to consider. Rather, the input signal is guided by the fiber, making the wave vector the same for all the beam paths. Reducing the diameter of the taper allows more of the propagating electric field to be evanescent, lowering the effective index of the fiber and hence changing the wave vector. This change will be in the right direction since the WGM of the microsphere has an effective index that is slightly lower than that of the bulk fused silica from which it is fabricated. By controlling the taper diameter, phase matching between the microsphere and taper can be achieved.^[37, 42, 47] Changing the diameter of the fiber also affects the field-overlap contribution to the effective transmission coefficient, making the matter nontrivial. However, this point seems to be not as critical as it first appears. In our lab, WGM dip depths of over 95% have been achieved on numerous occasions, without any special tailoring to maximize phase matching, and the best recorded dip depths exceed 99.8%.^[39] Empirically speaking, tapered fiber coupling appears to excite more WGMs than expected, many more than with prism coupling.

The tapers can either be single tapers, where the fiber terminates as a taper, or bi-tapers or biconical tapers, where the tapered region makes a transition back to the normal unaltered fiber. The preferred method is the bi-taper since both ends can be held fixed in place, making the tapered region immobile. Light collection is easy with the bi-taper, but

as described later in this chapter, the total recollection of light can be a problem since tapered fiber mode coupling can cause all but the fundamental fiber mode to be lost. Luckily, there are only two fiber modes that need be considered. Single tapers are not recommended for observing microsphere reflection signals, since light collection out of the fiber taper is difficult. However, single tapers are a good choice when collecting the microsphere transmission signal, where the signal exiting the fiber is at a cleaved face. They are also capable of accessing the microsphere when space is limited and a bi-taper is impractical or too cumbersome. The only problem is that the single tapered fiber end is not held fixed in position and is not very stable.

A common tapered fiber fabrication technique is heating the fiber while using translation stages to elongate it, where heating is performed by a stationary or traveling burner.^[48] The method developed in our lab is similar to this. The fiber, with the buffer jacket removed, is suspended with a mass attached to the bottom. Next, a small flame from the H-O torch is passed over the same spot on the fiber several times, heating it slowly as the fiber elongates. Diameters of five microns or less are obtainable using this method. After stretching, the end regions of the taper are usually fixed with epoxy or superglue to a microscope slide with cover slips superglued to them, as demonstrated in Figure III.2 (a). While drying, superglue tends pull the fiber from its prealigned position, placing transverse pressure on the taper. This makes epoxy the preferred adhesive. After the bi-taper is fixed in position, it can be used to excite WGMs. If the taper diameter is not small enough, hydrofluoric (HF) acid etching is used to further reduce the taper diameter. An acid concentration of 48% HF or a 50-50 solution of this and water is used

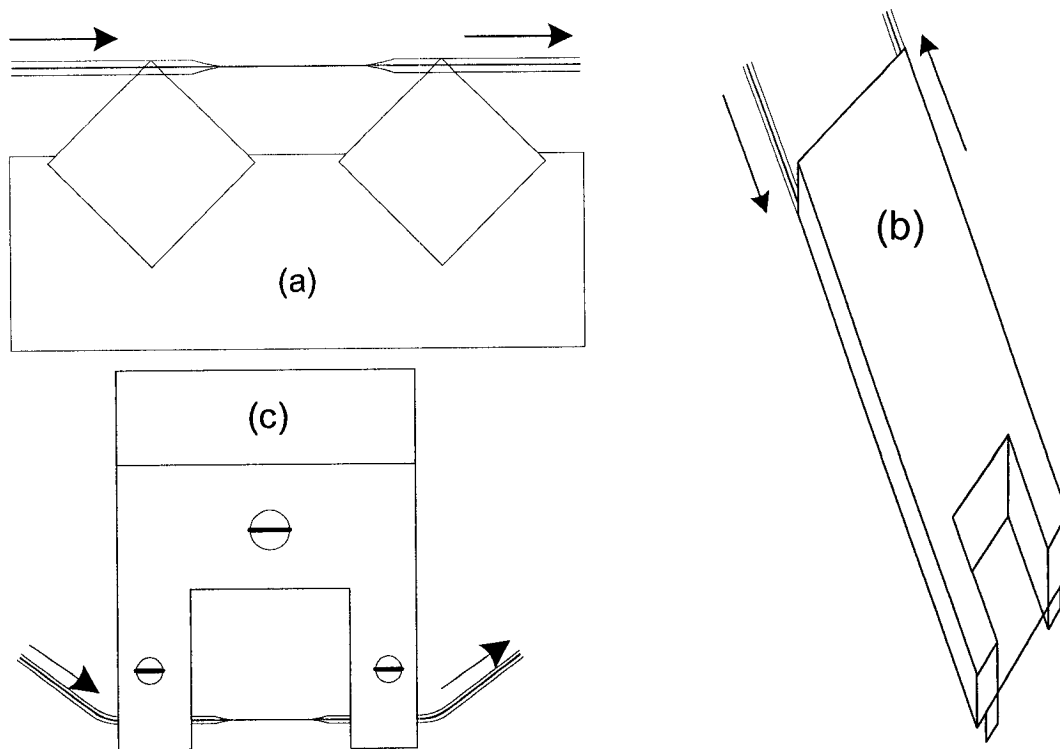


Figure III.2 Methods for mounting bi-tapered fibers. (a) Glass slide and cover slips, (b) Delrin U-shaped tension mounting apparatus, (c) Delrin U-shaped compression mounting apparatus.

for etching. To etch only the tapered region, a drop of acid is placed on a suitable material that does not react with HF, followed by placing the bi-tapered region inside the droplet. It is allowed to etch several seconds to several minutes until the desired diameter is reached. The etching process alone can be used to create a taper,^[40] but the fabrication time is significantly lengthened without much, if any, change in the end results. The etching progress can be monitored by the 45 \times microscope and by passing a laser signal through the fiber while monitoring the output. The latter is described later in the fiber mode coupling section of this chapter.

Two other devices have been constructed from Delrin to hold tapered fibers. Their principal use is for coupling in liquid. They are designed so that no epoxy or glue

need be immersed in the liquid to contaminate the sphere or the liquid. Figure III.2 (b) shows the design that was used for the intracavity liquid sensing experiment in Chapter VI. After the fiber is stretched to a diameter that is small enough that coupling can be employed without etching the fiber, the fiber is wrapped around the two prongs at the bottom of the apparatus. The two ends of the fiber are fastened to the upper portion of the holder with epoxy or super glue. The advantage of this design is when the only the lower portion is immersed in liquid, none of the adhesive encounters the liquid. This particular design works extremely well for placing a bi-taper on each side of the microsphere to observe reflection and transmission. The disadvantages are the bend losses are high and etching the taper is not possible. Just bringing the fiber close to the acid causes it to break, presumably from acid vapor getting into small fractures in the fiber bend. Figure III.2(c) shows the third design. In this case, the fiber is made immobile by clamping it between two pieces, while not placing enough pressure on the fiber to damage it. With this third design, no adhesive is used, the fiber can be etched, and no extra losses due to bending occur; however, only one side of the microsphere can be accessed.

5. Limitations

(a) Experimental Test of Ring Cavity Model

A simple and interesting example of how data can be readily analyzed using the ring cavity model is provided by scanning the laser frequency while varying the gap distance between the tapered fiber and the microsphere. The experimental setup uses a typical bi-tapered fiber that is stretched to a diameter that allows coupling between the

fiber and the microsphere and is mounted in the usual way, as shown in Figure III.2(a). The fiber taper is not etched with HF acid in the experimental results given here. In an initial experiment a bi-tapered fiber constructed by heat stretching followed by HF acid etching was used. There appears to be little difference between the results so only one of the cases is presented here. Only one bi-taper was used; that is, there was no transmission fiber, only a reflection signal. The 360- μm -diameter microsphere is held fixed in position while the fiber is mounted on a three-dimensional translation stage with sub-micron actuators. In this instance, the microsphere and fiber are observed under a microscope, 100 \times to 1000 \times . Since the laboratory is not equipped to perform sub-micron measurements, the actual gap distance cannot be measured. However, a varying gap distance can be readily observed. When the fiber is pulled away from the microsphere, the effective transmission coefficient T_l is reduced and the Q and dip depth change.

The TDL is used for this experiment at a wavelength of 1570 nm and a scan frequency of 100 Hz over a 6 GHz scan range. Figure III.3 shows a 400-MHz section of the scan range and includes nine individual scans of the same WGM at varying gap distances. The deeper the dip depth, the closer the fiber is to the microsphere. The power has been normalized to illustrate the percent of dip depth. The actual power collected at the output end of the fiber is on the order of a milliwatt. The scanning speed and incident power are such that there should be no thermal effects associated with the WGM.

Taking the value of the dip depth and Q from the data in Figure III.3 for each scan and using equations (II.13) and (II.23) with $T_3 = 0$ and $\phi = 0$ the values of T_l and α_i are calculated. From the two sets of possible solutions, the set that corresponds to the overcoupled case can immediately be dismissed. The fact that as the gap distance is

closed the mode decreases in depth and never increases, that is, it never passes through critical coupling, makes it obvious the mode is consistently undercoupled for at least the first seven traces (dark curves). The other two traces (light curves) could potentially be overcoupled, but are most likely undercoupled. These two traces are not included in the analysis below since the neighboring WGM overlaps with the WGM that is being analyzed, centered at 660 MHz. It is interesting to note that the two WGMs are shifted relative to each other as the gap distance is closed. This is attributed to a difference in the change in effective index of refraction between the two WGMs due to the presence of the tapered fiber.

The transmission coefficient and intrinsic loss values for the seven analyzed scans are listed in Table III.3. When the coupling fiber is closer to the microsphere, the overlap of the evanescent fields of the fiber and microsphere is greater. Therefore, it is to be expected that as the gap distance is closed, the values for the transmission coefficient increase. However, the results show that the intrinsic loss of the microsphere also increases significantly as the gap distance is closed. This result is somewhat surprising. Both the microsphere and tapered fiber are made of the same material, so the fiber should not significantly increase the intrinsic loss, which is dominated by scattering and water absorption. Possible factors that can increase the intrinsic loss include contaminants on the surface of the fiber and increased scattering from the fiber due to it being in the evanescent portion of the WGM. When this phenomenon was first observed with a heat stretched and HF acid etched fiber, it was thought that the acid etching could possibly leave contaminants on the fiber or leave small pits, increasing the surface roughness of the fiber. However, when the fiber is prepared without etching, as presented here, similar

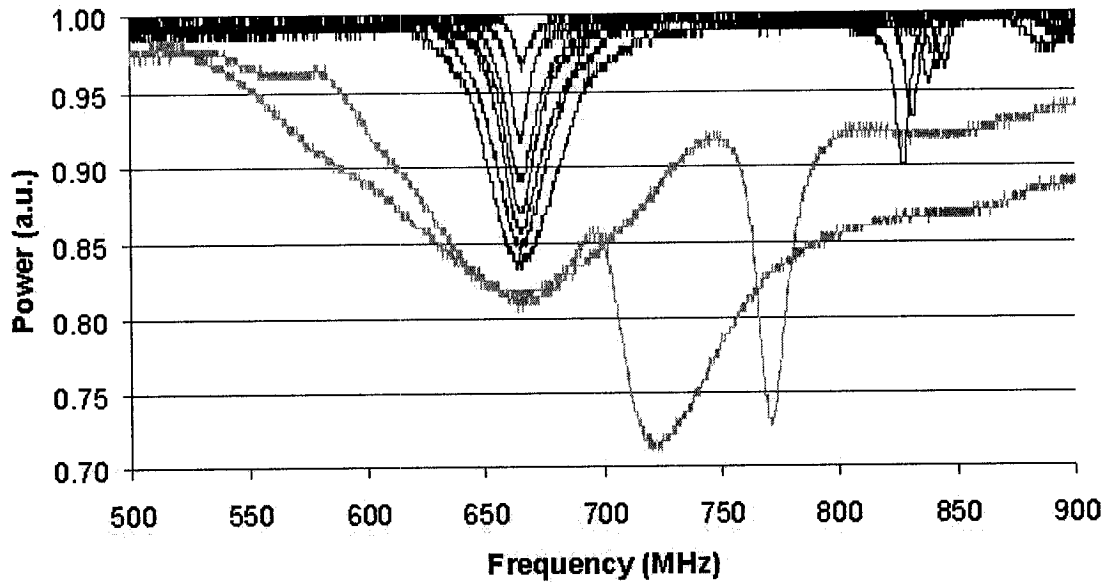


Figure III.3 Scans of the same WGM of a 360- μm diameter microsphere performed at varied gap distances between the tapered fiber and the microsphere. The frequency axis represents the change in laser frequency. The deeper the dip depth, the smaller the gap distance. The darker curves centered at 660 MHz are examined in Table III.3. The two lighter curves are distorted by the neighboring mode and therefore not used.

Table III.3 Calculated values of T_l and α_i from the measured dip depth and Q at varied gap distances between the tapered fiber and microsphere for the seven dark curves in Figure III.3.

Dip Depth (%)	Q	T_l	α_i (m^{-1})
96.8	2.49×10^7	2.1×10^{-6}	0.23
91.6	1.99×10^7	7.1×10^{-6}	0.29
89.1	1.21×10^7	15×10^{-6}	0.47
87.0	0.97×10^7	23×10^{-6}	0.58
86.1	0.92×10^7	26×10^{-6}	0.60
84.8	0.72×10^7	36×10^{-6}	0.77
83.8	0.55×10^7	51×10^{-6}	1.00

results were achieved.

This example is important to understanding practical applications of microsphere WGMs. This result affects the microsphere's ability to be used as a sensor. A high intrinsic loss coefficient is detrimental when employing microspheres for this type of application and is an important variable that directly determines the sensitivity of the detection level.

(b) Fiber Mode Coupling

The disadvantage of using a bi-taper is that fiber mode coupling results in a strong wavelength dependence of the fiber transmission. This is shown in Figure III.4 where the top curve is the laser power in free space and the bottom curve is the laser power transmitted through a tapered fiber. The vertical scale of the two curves is not necessarily the same. The small modulation on the fiber transmission signal is obviously due to the nonlinear power of the laser and the large modulation is a result of tapered fiber transmission. The transmission value of the larger modulation varies by up to 70% of the maximum transmitted signal.

A representation of the bi-tapered fiber coupling is shown in Figure III.5. When moving from the untapered to tapered region of the fiber, the core and cladding diameters decrease, making the fiber incapable of supporting the lowest order mode in the core. At this transition point the fiber becomes cladding-guided, allowing many possible modes to propagate due to the large index contrast between the cladding and surrounding medium. However, only taper-induced coupling between the HE_{11} cladding guided mode and the HE_{12} mode is the most prominent since both modes have similar azimuthal symmetry and minimal phase mismatch.^[49, 50] At the transition point after the taper, further HE_{11} - HE_{12}

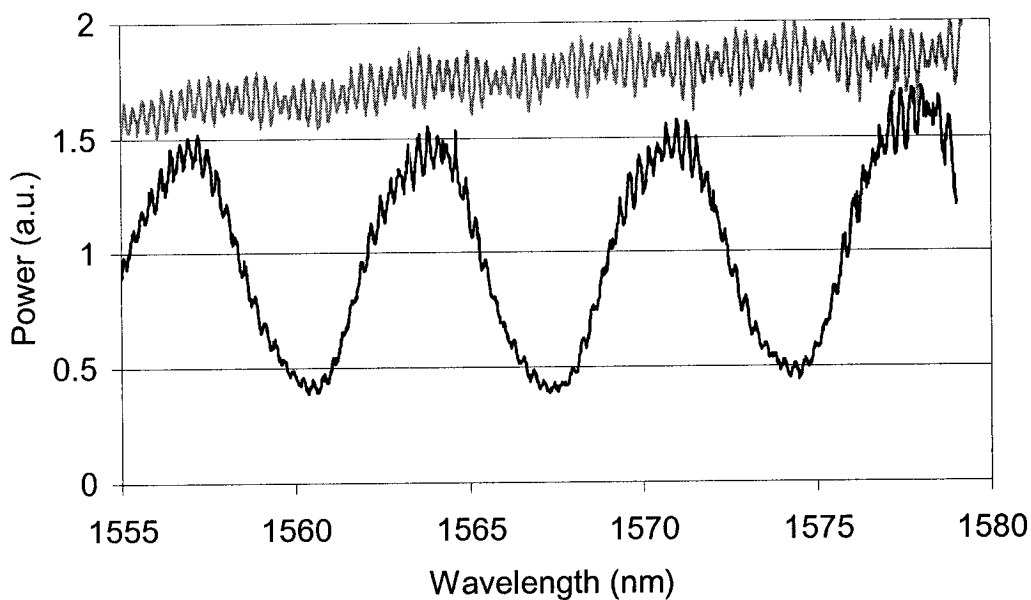


Figure III.4 Laser power as a function of wavelength through a tapered fiber (bottom curve), and in free space (top curve). The large oscillations in fiber transmission are due to fiber mode coupling.

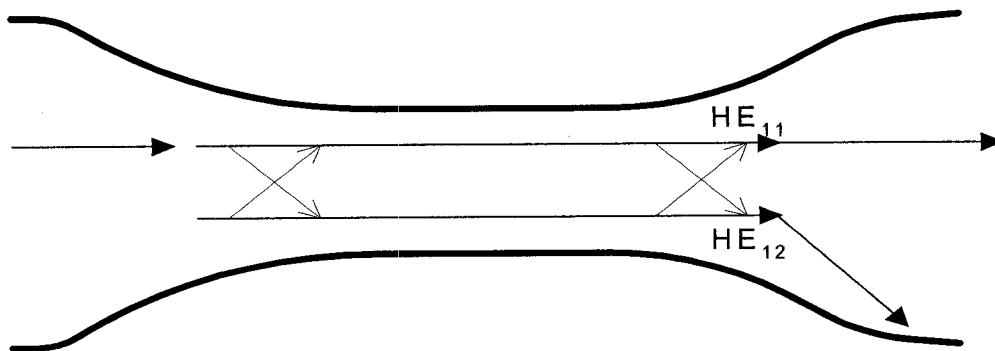


Figure III.5 Representation of mode coupling between two of the lowest order modes of a tapered fiber fabricated from a single-mode fiber. The light in the HE_{12} mode is lost as the tapered fiber returns to single-mode fiber.

coupling may occur, but only the HE_{11} mode will be recaptured by the fiber core and the HE_{12} mode will be lost.

The coupling between these two modes is dependent upon the phase mismatch, making the taper transmission wavelength-dependent in a sinusoidal manner, with the period of oscillation decreasing with decreasing radius.^[50] The effect of slope and radius can be seen in Figure III.6 where the transmission of the Ti:sapphire laser at a constant 830 nm is displayed as a bi-tapered fiber is etched in a 50% solution of HF. The top curve is the earliest in time with each curve below it progressing later in time, where the time between curves is on the order of seconds. The fact that the period of oscillation is decreasing suggests that the diameter of the taper can be monitored by the period of the

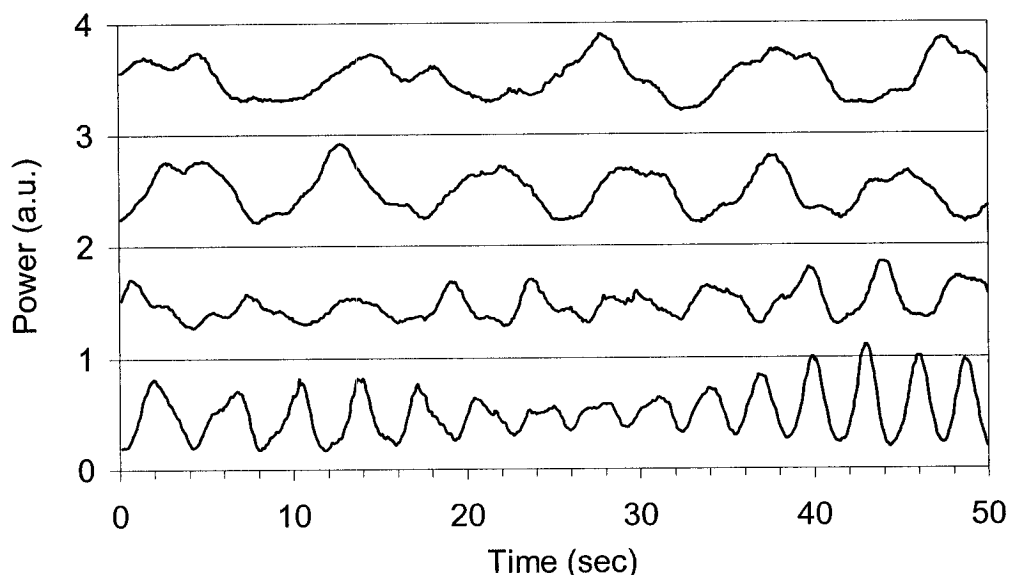


Figure III.6 Ti:sapphire laser power at constant 830 nm wavelength through a tapered fiber while HF acid etching the fiber taper. Each successive curve is vertically shifted by 1 unit, making its baseline the grid line immediately below it. The top curve is earliest in time and progressing downward for later times. The time between curves is several seconds.

oscillation. It is also interesting to note that it is possible for the maximum power transmitted to get larger as the taper diameter becomes smaller. This suggests that at the local maximum, not all of the power is in the lowest-order fiber mode. This observation is experimentally verified in the Appendix. This signal can be used when attempting to maximize the transmission of a particular wavelength, as is the case when trying to match the wavelength to a molecular resonance. However, it must be realized that the fiber mode coupling also depends on the index contrast between the fiber and surrounding medium. Meaning, a maximum in transmission while immersed in the acid is not necessarily a maximum when air is the external medium.

Adiabatic changes in the fiber diameter are desirable since the mode-mode coupling is also proportional to the slope and inversely proportional to the radius.^[49] Fiber mode coupling can be reduced by making the taper more adiabatic by etching the fiber before stretching.^[50] In practice, this does not eliminate mode coupling or the fact that the taper supports many modes. No matter how close the taper is to being adiabatic, light coupled out of a microsphere WGM, excited by the HE_{11} mode, can still be coupled to the HE_{12} mode. This mode coupling is the basis for the model in the Appendix, where two modes are allowed to propagate in the tapered region and couple to the microsphere WGMs. For all of the experiments performed in this dissertation the fiber was not etched prior to heat stretching.

6. Laser Properties

Three lasers were used to perform experiments. The Millennium laser from Spectra Physics is a diode-pumped non-tunable cw frequency doubled Nd:YVO₄ laser. The

operational wavelength is 532 nm with a maximum output power of 5.5 W. Its primary purpose is to pump the cw Ti:sapphire laser, model MBR-110 from Microlase (now Coherent Scotland). At peak power the Ti:sapphire laser is capable of output powers in the range of 400-500 mW. It is continuously tunable over 40 GHz at a maximum internal scan frequency of 0.1 Hz and can be externally scanned at a scan frequency of about 1 Hz. The laser frequency tuning appears to be linear with an applied signal voltage. The operational wavelength range is 770 nm to 860 nm with the primary mirror set. By changing to one of two other mirror sets, the wavelength range can be changed to 690 nm to 800 nm and 860 nm to 930 nm, although the latter gives a significant reduction in laser power. Changing mirror sets is not done on a regular basis since aligning the laser is non-trivial.

The Velocity 6328 laser system from New Focus is a tunable diode laser with an operational wavelength range from 1508 nm to 1584 nm. The peak power is approximately 10 mW at 1550 nm and falls off to half this value as the laser is tuned toward the minimum and maximum wavelengths. As demonstrated in the top curve of Figure III.4, where the constant power setting on the laser control unit is enabled, the laser power output is oscillatory over large tuning ranges. This is largely due to reflections from an imperfect anti-reflection coating on the diode face inside the laser cavity, making it impossible to remove these oscillations. Over short scanning ranges, the power appears to be linear with a small slope; over larger ranges, it is necessary to use a beam splitter to obtain a reference signal to remove the laser frequency dependence. In constant power mode, it is recommended by the laser manual to scan at 1/100 of the laser's maximum scanning speed for best results and does not guarantee to remove

oscillations smaller than 5%.

The Velocity laser is capable of continuous scanning over a fine-tuning range of 30 GHz, with the scan range falling off significantly with scan frequencies above a couple hundred hertz. The laser scan distance is plotted as a function of the scanning frequency for peak-to-peak voltages of 2, 4, and 6 volts in Figure III.7. The fine-tuning is controlled by a piezo-electric actuator (PZT) and PZTs are notorious for hysteresis effects. Knowledge of this effect is important when a constant scan rate is required and when bi-directional scan comparison is used. Examples of these cases are seen throughout experiments in this dissertation, including temperature sensing, thermal bistability, and frequency locking the microsphere to the laser. The laser frequency versus the applied voltage is plotted in Figure III.8, where the data used to produce the plots was collected using a confocal optical spectrum analyzer with a 2 GHz FSR. The results for peak-to-peak voltages of 2, 4, and 6 volts are plotted for a 0.10 Hz scan. The graphs show that the hysteresis is more prominent over a larger scanning range. Ideally, linearizing the scan is desirable, but an active control method would be the best solution since the scan range and hysteresis are not constant with scan rate and applied voltage.

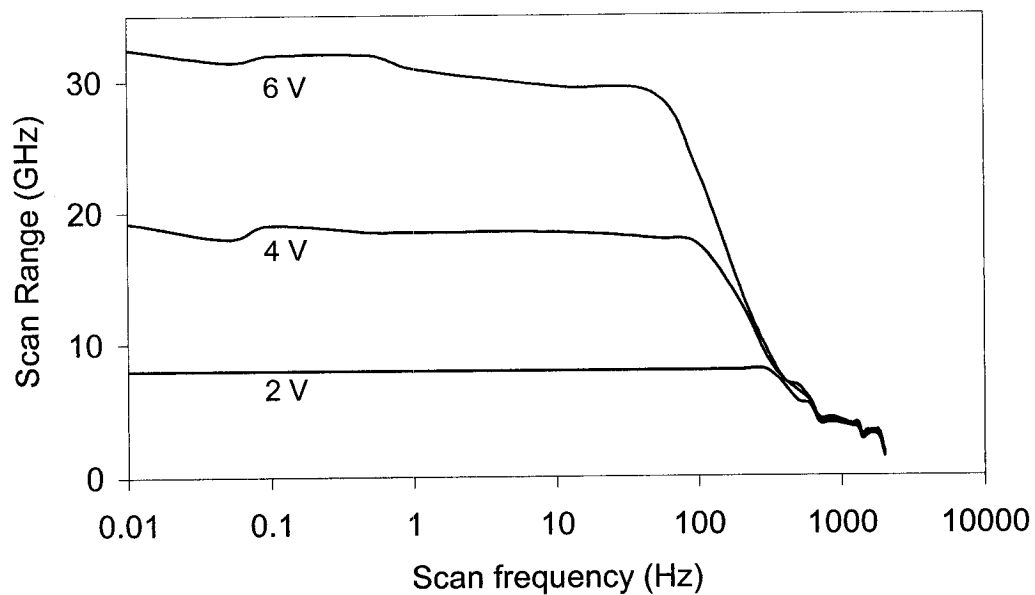


Figure III.7 Velocity TDL scan range as a function the scan frequency. The three lines represent a peak-to-peak voltage of 2, 4, and 6 volts from lower to higher, respectively.

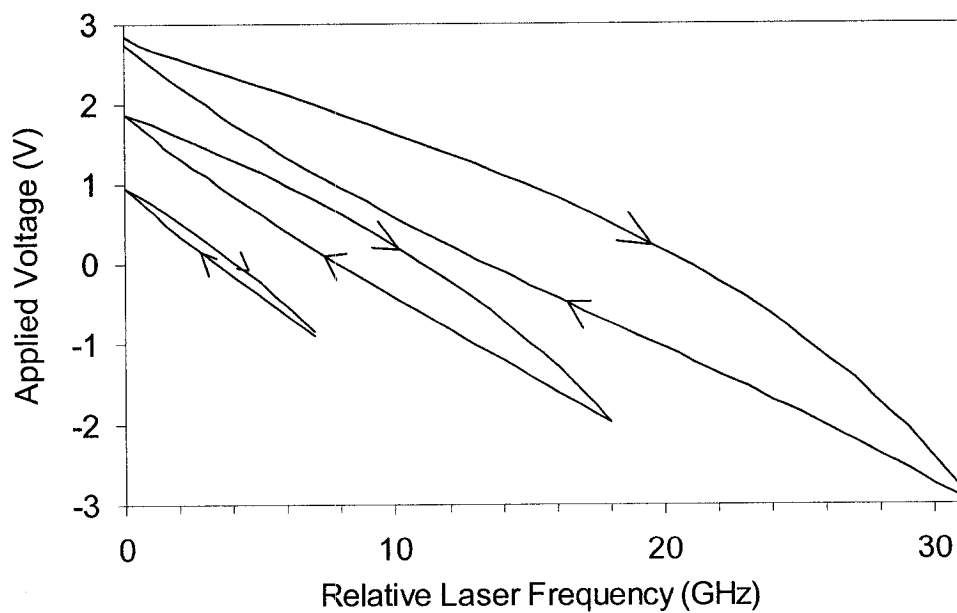


Figure III.8 Hysteresis of Velocity TDL frequency with applied voltage for frequency fine-tuning. All scans are performed at 0.10 Hz. The arrows indicate the direction of the laser scan.

CHAPTER IV

COMPRESSION TUNING AND LASER FREQUENCY TRACKING

1. Introduction

The resonance frequency of a particular WGM, as given by equation (II.5), is dependent on the nominal free spectral range (δ), the eccentricity, and a polarization-dependent index of refraction term. Changing any of these values tunes the resonance frequency of the selected mode. δ is varied with changing index of refraction or equatorial radius, the eccentricity is dependent on the axial and equatorial radii, and the polarization shift is dependent on the index of refraction.

One method for tuning the resonance frequency of WGMs is changing the temperature of the microsphere. Temperature tuning is dominated by the change in index of refraction and the tuning rate is limited by thermal relaxation times. This form of tuning is examined in detail in Chapter V. A more efficient method of tuning is axial compression^[32] or stretching^[27, 51] of the microsphere. In this case, the primary tuning effect is the change in the physical equatorial path length, enabling fast tuning up to an entire free spectral range (FSR). The focus of this chapter is controlled compression tuning and active locking of a WGM resonance to a tunable laser source, and it describes the theory, compression tuning device, and tuning and locking results.

The application of compression tuning was first demonstrated by Il'chenko, et

al^[32] where they successfully tuned WGMs of a 160- μm -diameter microsphere over 150 GHz, 1/3 of a FSR, at a wavelength of 807 nm with their own compression tuning device. Their device had a tuning speed of 10 GHz/ms at a 400-Hz modulation rate, and they did not demonstrate locking the microsphere to a laser source.

The work presented in this chapter introduces a new compression tuning device that improves the fractional FSR fine tuning, adds a tuning screw that enables coarse tuning over several FSRs, and increases the modulation rate by over an order of magnitude, and an experimental setup that allows for actively locking a WGM to a tunable laser source^[52, 53]. Since this work was completed, Il'chenko has presented work on stretch tuning a microsphere,^[27, 51] where a fiber was connected at the top and bottom of the microsphere. This novel approach is commendable and has advantages, namely accessibility for prism coupling; however, tuning over more than a FSR is still not possible and appears to be limited by the microsphere-fiber tension limit. In addition, the construction technique is performed with a CO₂ laser and appears to be more difficult.

2. Theory

The amount of tuning due to axial compression is calculated from the frequency equation (II.5),

$$v_{q\ell m}^{TE(M)} = \delta \left(\ell + 1/2 - a_q \left(\frac{\ell + 1/2}{2} \right) - \Delta^{TE(M)} \pm \varepsilon^2 \left(\frac{\ell - |m|}{2} \right) \right),$$

where the higher order terms have been dropped. When compressed, the axial and equatorial radii (a_a , a_e) change along with the index of refraction, which changes due to the photoelastic effect. Differentiating with respect to these three variables results in the expression,

$$\frac{\Delta v}{v} = -\frac{\Delta a_e}{a} - \frac{\Delta n_s}{n_s} + \frac{\delta(1-\varepsilon_0^2)}{v} \left(\frac{\ell - |m|}{a} \right) (\Delta a_e - \Delta a_a) \quad (\text{IV.1})$$

where ε_0 is the original eccentricity. The first two terms on the right-hand side come from the fractional change in δ , and the last term results from the change in eccentricity; tuning due to the change in the $\Delta^{\text{TE(M)}}$ term is negligible and is therefore not included. After differentiation, it is assumed that a_e and a_a are equivalent and set equal to a .

For large spheres, such as the sizes that are used for all the compression tuning experiments, it is convenient to use the approximation that ℓ is large compared to all of the other bracketed terms in equation (II.5). This, along with the assumption that $\varepsilon_0^2 \ll 1$, simplifies equation (IV.1) to

$$\frac{\Delta v}{v} = -\frac{\Delta a_e}{a} - \frac{\Delta n_s}{n_s} + \frac{\ell - |m|}{\ell a} (\Delta a_e - \Delta a_a). \quad (\text{IV.2})$$

In terms of the fractional change in axial radius, the above expression for tuning can be written as

$$\frac{\Delta v}{v} = -\frac{\Delta a_a}{a} \mu \left[1 + b^{\text{TE(M)}} - \left(\frac{1 + \mu}{\mu} \right) \frac{\ell - |m|}{\ell} \right], \quad (\text{IV.3})$$

where $\mu = -(\Delta a_e / \Delta a_a)$. Because the tuner's contact-surface configuration is not too different from that of Reference [32], their strain results are used to estimate the relative contributions of the terms, specifically, that $\mu = 0.11$ (rather than the fused-silica Poisson ratio of 0.17), and that the photoelastic contribution is $b^{\text{TE}} = -0.14$ or $b^{\text{TM}} = 0.07$. Since $\ell \approx 1500$ for the 550- μm -diameter sphere used at 1570 nm, the last term in equation (IV.3) contributes -0.16 for $\ell - |m| = 24$, and so the physical path length change given by the first term is the dominant tuning effect. The value of $\ell - |m| = 24$ is

an estimate for the maximum observed here, as very long frequency scans showed families of 20-25 modes with ~ 1 GHz spacing, each with a bandhead that is probably the $|m| = \ell$ mode.

3. Experimental Setup

Both the TDL and the Ti:sapphire laser were used for this experiment. Light, from one of the two tunable lasers, was injected into an angle polished fiber that was tapered to allow coupling between the fiber and the microsphere. The taper was constructed by heat stretching followed by HF acid etching a single-mode fiber. Angle polishing the fiber minimizes the effect of back reflection into the laser source, which causes it to become unstable by operating on more than one mode or causing frequency instability while scanning. After this experiment an optical isolator was purchased to stop back reflected light from entering the TDL. The use of a quarter waveplate and polarizer creates an effective isolator for the Ti:sapphire laser.

A sketch of the experimental setup is shown in Figure IV.1. An inline fiber polarization controller, placed before the tapered region, is used to control the polarization in the fiber. This allows TE and/or TM WGMs to be excited in the microsphere, depending upon the polarization in the tapered region of the fiber. When the light exits the fiber, the detector sends a signal to a commercial lock-in stabilizer that is designed for CO₂ laser stabilization. A voltage signal, composed of a bias and modulation signal, that controls the microsphere tuning is sent from the lock-in stabilizer to the compression tuner. The maximum bias signal output from the stabilizer is -1600 V. A capacitive voltage divider, shown in Figure IV.2, is used to reduce the voltage to

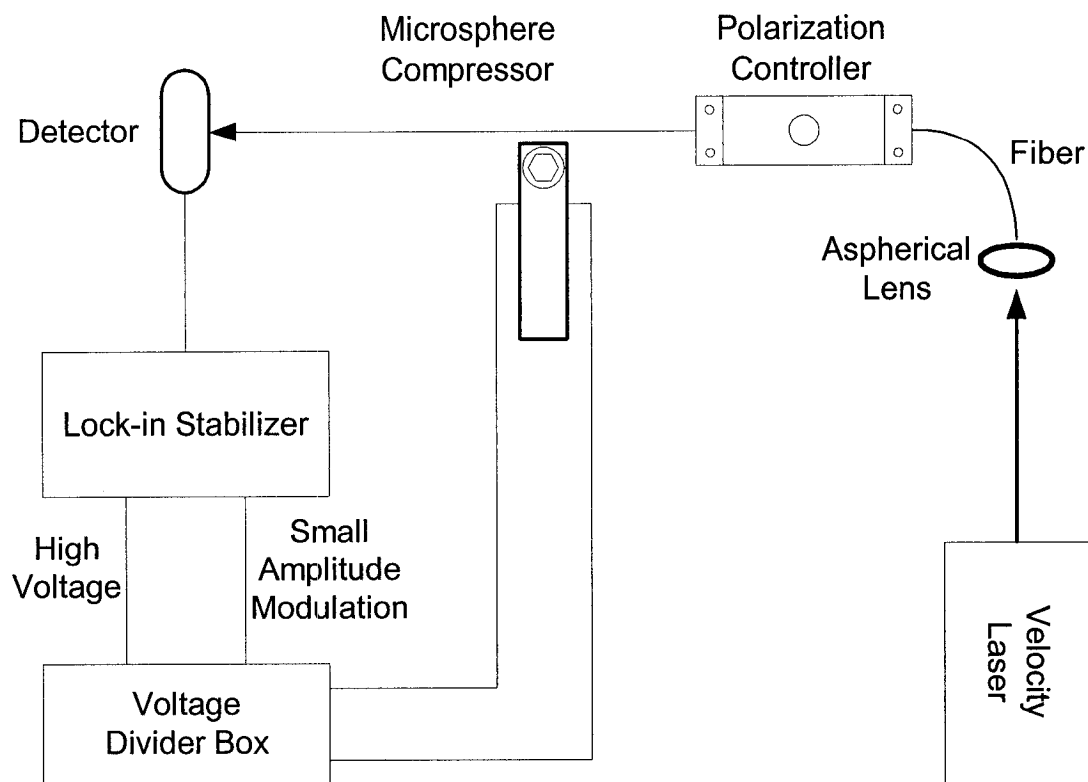


Figure IV.1 Experimental setup. The lock-in stabilizer can use the detector signal to lock a WGM to the laser, or it may simply be used to apply a dc bias voltage to the compression tuner's PZT.

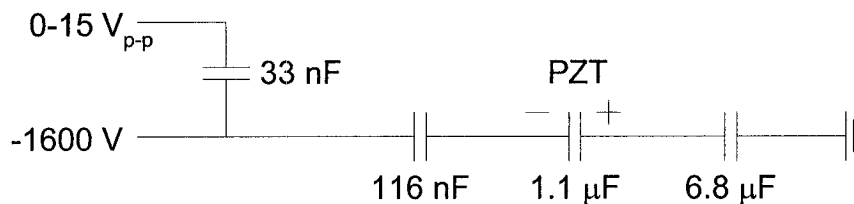


Figure IV.2 Capacitive voltage divider used to combine DC bias and modulation signal from the lock-in stabilizer for application to the PZT in the microsphere compressor.

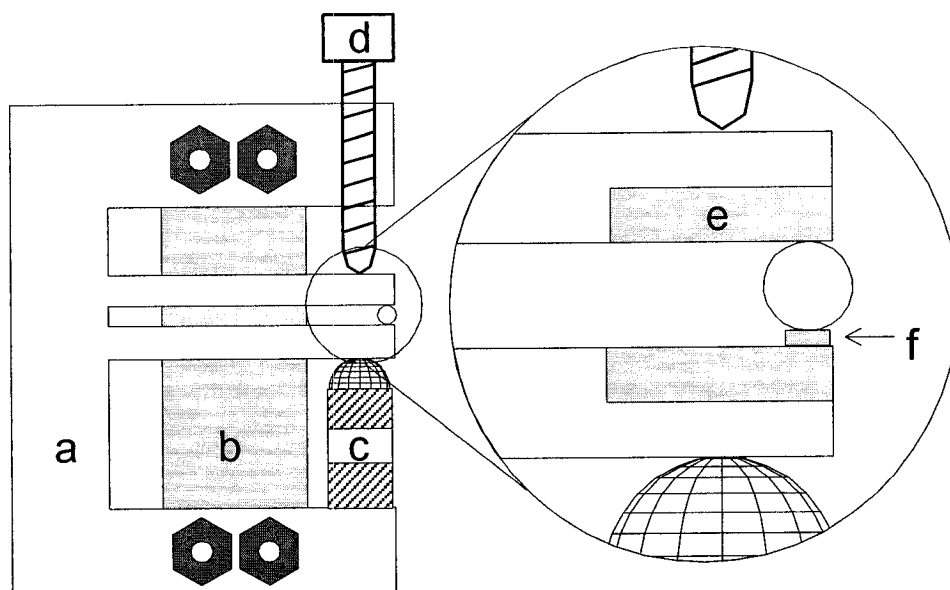


Figure IV.3 Compression tuner. (a) Main body is 44×38×6-mm aluminum. (b) Stainless steel brace minimizes flexing of main body. (c) Piezoelectric actuator. (d) Manual tuning screw. (e) Hardened steel compression pad. (f) Stainless steel hypodermic tubing, inserted into hole in lower steel pad.

150 V when the stabilizer is set at the maximum bias. This reduced signal is applied to the PZT in the compression tuner. The small voltage modulation is used to actively lock a WGM resonance to the laser. Its maximum 15-V peak-to-peak voltage is also reduced by the voltage divider before being sent to the PZT. The modulation signal will be described later in this chapter.

The tuner has six important parts in its design, labeled (a)-(f) in Figure IV.3. The main body is constructed from a ¼ inch (6 mm) aluminum sheet cut 1.7" (44 mm) high by 1.5 inches (38 mm) in length; 1.0-inch length middle arms allow tuning at high frequency rates. Constructing the main body from aluminum minimizes the moving mass and maximizes the tuner's response speed. The resulting flexibility of the upper

compression arm allows the design to accommodate a large range of microsphere sizes, while the lower arm applies a preload force to the PZT. The downside of using aluminum is that the main body is flexible, reducing the efficiency of the force exerted to tune the microsphere. For this reason a rigid stainless steel brace, connected by two bolts at the top and bottom, is used to minimize the flexing and improve the tuning range by over an order of magnitude.

The PZT is a low voltage multiple layer stack with no outer casing, part number PSt-150/5×5/7, from Piezo Mech. The stack has dimensions 5×5×7 mm, with the optional 5-mm-diameter ceramic spherical top piece added. The extension is 7 μm with an applied voltage of 150 V. It has a 70-kHz resonance frequency and an optimum compression load range (stiffness) of 120 N/ μm . In order not to damage a PZT, a preload force must be placed in the direction of expansion before use. The lower middle arm of the main body supplies this preload force. After preloading the PZT in the compressor, the microsphere can be loaded.

The microsphere was fabricated in the usual way with a hydrogen-oxygen torch, with the microsphere stem diameter smaller than the 50- μm inner diameter of the hypodermic tubing that the microsphere is mounted in. When fabricating microspheres with the torch, an upside down teardrop shape is usually formed in the transition region between stem and microsphere due to gas rushing past the forming microsphere. If the stem diameter is not small enough and the transition region is too large, the teardrop shape forms a wedge that can damage the hypodermic tubing when the microsphere is compressed. To avoid this, the stem diameter is made much smaller than the inner diameter of the tubing and great care is taken to ensure the transition region is sufficiently

small. After fabrication, excess stem is removed and the microsphere is only handled at the stem with tweezers. This ensures no unnecessary contaminants or scratches are imparted on the surface of the microsphere that might degrade the Q .

A short length of stainless steel hypodermic tubing is used for mounting for the same reason the upper compression pad is made of hardened stainless steel. If the upper and lower contact surfaces are a soft material, such as aluminum, much of the microsphere compression force is used to deform the aluminum and sink the microsphere into it. For stability, the ratio of the 300- μm outer diameter to the length of the tubing is approximately 1:5. When this is inserted into the 300- μm precision hole drilled in the $\frac{1}{4}$ " \times $\frac{1}{4}$ " \times 0.1" removable lower pad, the ratio of outer diameter and the exposed tubing is approximately 1:1 or less, making bending deformation of the tubing nearly impossible.

Although the smallest microsphere that has been mounted in the tuner is 200 μm , the tubing's 50- μm inner diameter makes 100 μm the practical lower limit on the microsphere diameter for this tuner. Fiber coupling was used for convenience, but prism coupling could be employed for spheres of diameter greater than 300 μm by using tubing above as well as below the sphere or by placing the microsphere close to the edge of the upper compression pad.

The function of the manual tuning screw is twofold, mounting (preloading) and coarse tuning. Once the microsphere is mounted in the tubing and placed in the tuner, the manual tuning screw is lowered to impart a force on the upper compression arm, which in turn places a force on the microsphere. It is lowered until a sufficient amount of force is placed on the microsphere to preload it and allow PZT tuning. While the PZT offers fine tuning over a range limited to one FSR or less, the manual tuning screw compresses the

microsphere over a much greater range, but with less accuracy. The tuning screw was a 4-40 pitch; to gain more control over the manual tuning a finer pitch screw could have been used, such as an 80 TPI screw.

4. Tuning Results

Using the fact that the change in physical path length is the dominant tuning effect, the equation

$$\frac{\Delta\nu}{\text{FSR}} \approx \mu \frac{\lambda \Delta a_a}{2\pi n_s} \quad (\text{IV.4})$$

shows the ratio of the tuning range to the FSR is independent of sphere size and depends on the free space wavelength (λ) and the axial compression. This makes the ratio a good choice as a figure of merit for comparison of compression-tuning results of different microspheres.

The experimental results given in this chapter are for a 550- μm diameter microsphere that had a nominal FSR of 120 GHz. The FSR value is only weakly wavelength-dependent, so the same value applies both at the primary experimental wavelength of 1570 nm and also at 830 nm, which was used for comparison with earlier published results. Adjustment of the tuner's manual tuning screw allows coarse tuning over several free spectral ranges, permitting a choice of which set of modes to make accessible to PZT tuning. The manual tuning range was approximately 500 GHz (4.2 nm) at 1570 nm and 1 THz (2.2 nm) at 830 nm. Applying PZT voltages up to the specified maximum of 150 V gave a fine-tuning range of 36 GHz (0.3 nm) at 1570 nm and 80 GHz (0.18 nm) at 830 nm. The latter value, two-thirds of a FSR, is nearly a factor of two greater than previously reported for compression tuning,^[32] and also better than

reported for stretch tuning.^[27, 51] The observed PZT tuning ranges correspond to an axial diameter compression of approximately 1 μm . This is a fraction of the 7 μm PZT extension for a 150-V bias, but is a larger fraction than in previous work. This improvement is most likely due to the use of harder contacting materials. With other microspheres, PZT tuning of two-thirds of a FSR at 1570 nm, which would correspond to about 1.2 FSRs at 830 nm, has been achieved.

Scanning the laser and noting the displacement of WGMs with PZT bias measured the tuning ranges. This will be described in the next section (Figure IV.6). The frequency scale was calibrated using a commercial confocal optical spectrum analyzer with a FSR of 2 GHz. Increasing the preload compression increases the PZT tuning range; however, the amount of strain the microsphere can endure before structural failure occurs is limited.

The tuning speed was measured by applying a 5-V peak-to-peak sine wave to the PZT; the resulting scan range is shown in Figure IV.4 as a function of the frequency of the applied voltage signal. Using this method, the maximum tuning speed found was at least 16 GHz/ms, as seen in Figure IV.5. This shows that significant tuning at a modulation rate of up to 13 kHz is possible. The linear dependence of scan range on the modulation rate is a surprising result and there is no obvious explanation, but is probably due to the added influence of driving the PZT through an effective low-pass filter, by connecting it directly to the function generator.

It is important to point out the limitation, that during compression tuning of some microspheres, the dip depth of individual WGMs changed by as much as 50% of the total signal. This change is observable over the PZT tuning range, but is relatively smooth

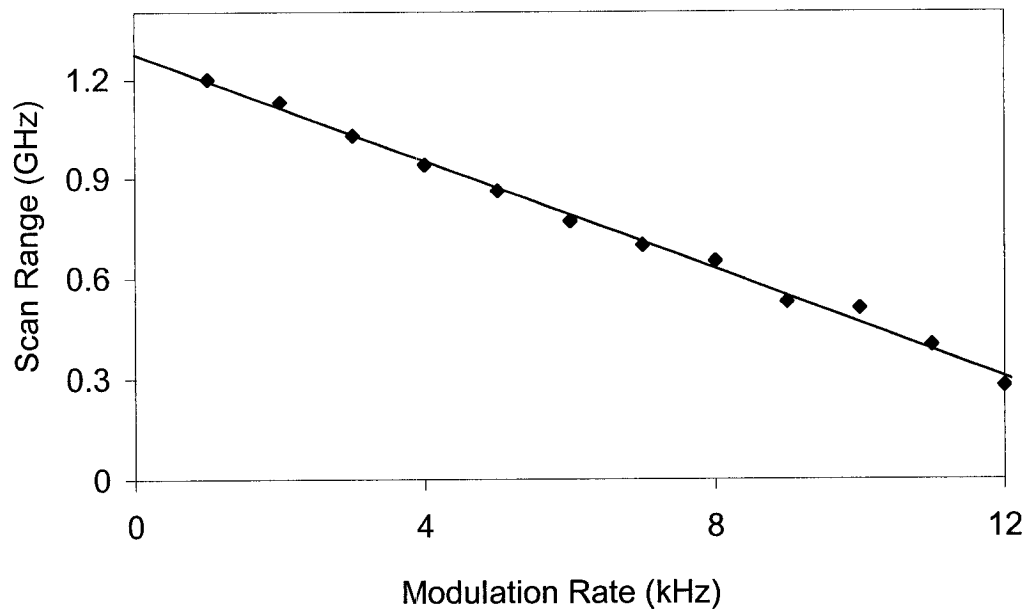


Figure IV.4 Scan range, for a 2.5-V amplitude sinusoidal voltage applied to the PZT, versus frequency.

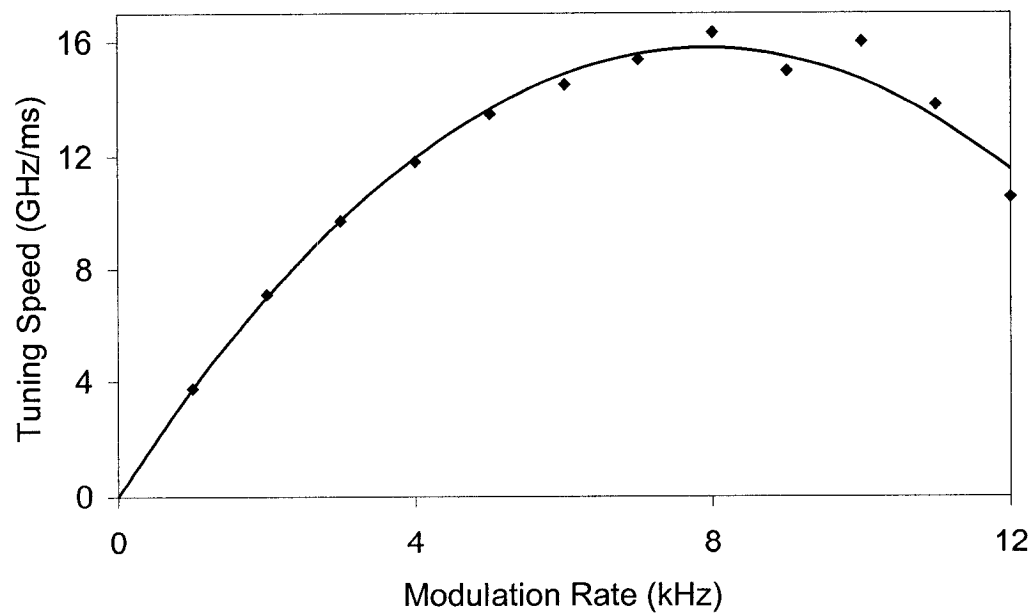


Figure IV.5 Maximum tuning speed, calculated from the scan range data shown in Figure IV.4.

with little or no discontinuity in the dip depth versus frequency. This change does not occur while temperature tuning the WGMs; therefore, this phenomenon is attributed to off-axis compression of the microsphere, causing changes in the microsphere that can change the coupling and loss conditions. This can be avoided if the microsphere is loaded correctly in the compression tuner.

5. Locking Results

When locking a WGM to a laser, the purpose of the lock-in stabilizer is more than just manually tuning the PZT bias. Its fixed 518-Hz modulation signal and dc bias are combined in a capacitive voltage divider, shown in Figure IV.2, for application to the PZT. An applied modulation of 30-60 mV_{p-p} to the PZT gave the best locking results in terms of ease of establishing a lock, maintaining the lock while the laser is tuning, and noise level from signal modulation while locked. The locking conditions for the collected data were chosen so as to provide a stringent test of the stability of the technique. One indication of stability was that the microsphere/fiber system did not need to be isolated from air currents or from vibrations; in fact, bumping or banging the table did not necessarily upset or lose the lock. A further demonstration of stability is the fact that even though fiber coupling excites many modes, as seen in Figure IV.6, a continuous lock to an individual mode is maintained.

The four laser frequency scans in traces (a)-(d) of Figure IV.6 are over the same range, with different constant bias voltages (and no locking dither) applied to the PZT. The inline fiber polarization controller assures that all the modes have the same polarization, but there is some variability in their relative positions from (a) to (d)

because of the slightly different tuning rates for modes of different m . The deepest dip, indicating about 20% power loss to a mode with $Q = 2 \times 10^6$, is the one locked to the laser.

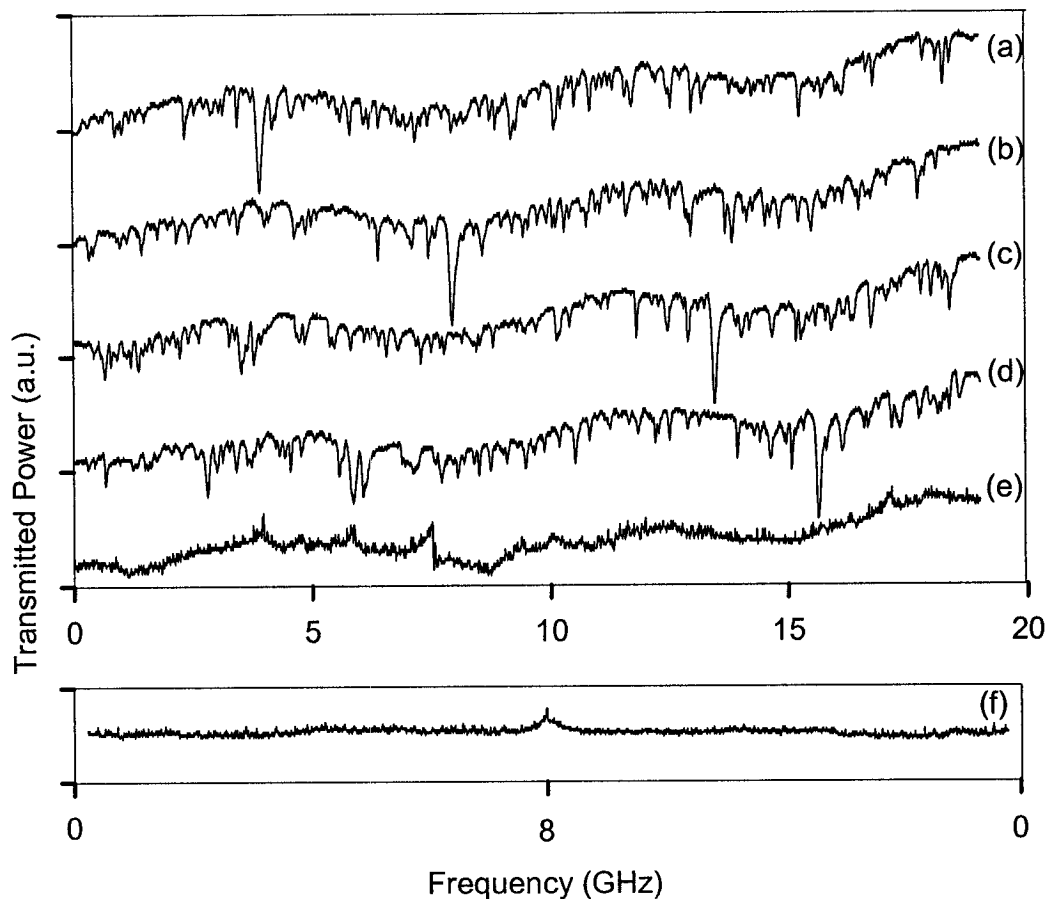


Figure IV.6 Unlocked and locked frequency scans at 1570 nm. (a)-(d) Unlocked: WGM mode spectrum observed as the laser is scanned over a 19 GHz range; an increasing frequency shift is seen for PZT bias voltages of 68 V, 88 V, 118 V, and 130 V, respectively. The baseline for trace (a) is at the frequency axis, and successive traces have been displaced vertically. (e) Locked: frequency scan where the WGM with the deepest dip in (a)-(d) is locked to the laser. The baseline is the same as for trace (d). No mode hops are observed. (f) Another locked frequency scan at 1570 nm. The laser scans 8 GHz and returns. The vertical scale is the same as in (a)-(e). The baseline is offset and again the locked transmission is about 80% of its off-resonance value. No mode hops are observed.

A scan over the same range while the 20% dip is locked to the laser is shown in Figure IV.6(e). Note that the slow power variation with frequency due to the tapered fiber transmission properties is the same in (a)-(e). From (e), it is evident that the locking never switches to another mode, because doing so would result in an obvious displacement of the trace; the larger fluctuations may indicate temporary overlap of a differentially-tuning mode with the locked mode. The signal was repeatable as the laser scanned over its range several times. The noise level on this trace is consistent with the approximately 150-mV peak-to-peak noise on the PZT bias. As a result of this noise, the effective lock point fluctuates with amplitude of about one-fifth of the 90-MHz WGM linewidth. Figure IV.6(f) shows a scan over 8 GHz, first increasing then decreasing the frequency, under conditions of more uniform fiber transmission, illustrating the constancy of the locked mode power throughput that is achievable with this locking method.

Another verification of the robustness of WGM locking and tracking is shown in Figure IV.7, where the PZT bias that is keeping a WGM locked to the 1570-nm laser is plotted as the tuning signal applied to the laser's frequency-modulation input is ramped up and down. This is the same 19 GHz tracking range shown in Figure IV.6 and this data was taken simultaneously with the data in Figure IV.6(e), ensuring that any signs of mode jumping or unlocking will be displayed in both data sets at the same point. The lighter, smooth curve in Figure IV.7 is the bias predicted from the laser frequency tuning as observed with an optical spectrum analyzer. Comparison of the two curves in Figure IV.7 shows that most of the hysteresis seen in the bias is actually hysteresis in the laser tuning, with only a small contribution coming from the slight nonlinearity of the

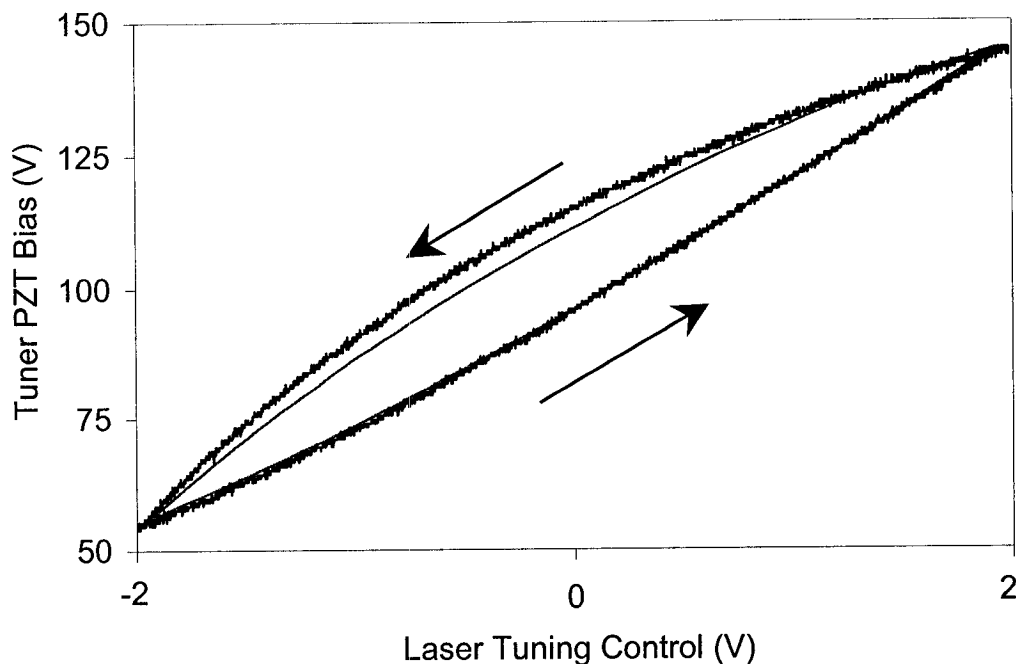


Figure IV.7 Locked tuner PZT bias as it follows a 19-GHz frequency scan (and return) of the 1570-nm laser. Heavier (rough) curve: PZT bias; no mode hops are observed. Lighter (smooth) curve: bias predicted from observed laser tuning hysteresis, assuming linear tuner PZT response.

compression tuner's PZT. A mode jump would appear as a displacement of the bias curve by an amount on the order of ten times the noise level, and none are seen. The locking and tracking range shown in Figs. IV.6(a)-(e) and IV.7 is 19 GHz, but locked tracking was also possible over 30 GHz, the maximum scan range of the 1570-nm laser.

In other cases using fiber coupling, WGMs at 1570 nm with Q s better than 10^7 and dip depths over 90% have been locked to the laser. Locking at 830 nm with the Ti:sapphire laser worked just as well, and again the maximum tracking range was limited only by that laser's frequency scan range of 40 GHz. At 830 nm the WGMs typically had Q s of 5×10^6 . Even under the environmentally noisy conditions that were used here, a

WGM would remain locked to either laser for hours, with the laser scanning at rates of up to 2 GHz/s.

Observing the transmission of fixed-frequency 830-nm light while a WGM was locked to the scanning 1570-nm laser also tested the locking behavior. To do this, light from both lasers was simultaneously injected into a bi-tapered fiber. At that fiber's throughput, the 1570-nm signal was detected and used for locking. Additionally, a single tapered fiber was used to observe the microsphere transmission, where the 830-nm transmitted light was detected. As the locked microsphere followed the scanning laser, various modes were successively brought into resonance at 830 nm and their detection produced a WGM mode spectrum at that wavelength, in analogy with a typical scanning optical spectrum analyzer. Inspection of this mode spectrum also showed no obvious evidence of any locking mode hops. The best way to determine this, given the dense spectrum of excited modes, would be to compare the forward-scan and reverse-scan spectra. Unfortunately, the hysteresis in laser tuning made direct comparison difficult; while one-to-one mapping of the spectra onto each other was possible, simply superimposing the two traces could not do this. This difficulty could be overcome by programming an arbitrary waveform generator to provide an asymmetric ramp to the diode laser's frequency-modulation input, so that the laser frequency variation would be linear in time. However, this is difficult since the laser hysteresis is variable with tuning range and speed.

6. Summary and conclusions

Some results for WGM frequency tuning, locking, and tracking are summarized

in Table IV.1. These results, for a microsphere 550 μm in diameter, are representative of what can be achieved with the methods and apparatus described here. As noted above, using a wavelength of 1570 nm and other microspheres, PZT tuning ranges that are an even larger fraction of the FSR have observed. This compression tuner allows for tuning over a greater range, and with faster response, than previously demonstrated.^[27, 32, 51] The ability to lock a high- Q WGM to a laser, and to track the laser as it scans in frequency, will be useful for a number of potential applications of microsphere resonators, including cavity QED,^[10, 27, 51] atom trapping,^[11, 12] and WGM microlaser tuning.^[4, 6, 54] Similarly, the tracking range demonstrated here is more than sufficient for the implementation of wavelength-modulation spectroscopy in WGM evanescent-wave trace gas sensors.^[55] The maximum laser scan rate at which a WGM will remain locked, 2 GHz/s, is determined by the locking dither frequency and the Q value of the WGM. Locked scanning must be slow enough that the frequency change during one dither cycle is small compared to the WGM linewidth. To increase the maximum scan rate, it would be desirable to frequency-modulate the laser output to provide a faster locking dither. Then the locked scan rate would be limited only by the maximum compression tuning speed,

Table IV.1 Tuning ranges for a 550- μm diameter microsphere at two wavelengths.

Range	1570 nm	830 nm
FSR	120 GHz (1.0 nm)	120 GHz (0.27 nm)
Manual	500 GHz (4.2 nm)	1000 GHz (2.2 nm)
PZT	36 GHz (0.30 nm)	80 GHz (0.18 nm)
Locked*	30 GHz (0.24 nm)	40 GHz (0.09 nm)

*Limited by the lasers' continuous tuning ranges

which we found to be at least 16 GHz/ms. Thus locked modes of $Q = 2 \times 10^6$ could follow a scan nearly four orders of magnitude faster, or locked modes of $Q \cong 10^{10}$ could be scanned at the present rate.

CHAPTER V

TEMPERATURE TUNING AND THERMAL BISTABILITY

1. Introduction

Attempting to actively lock a WGM resonance to a laser using temperature tuning would be very difficult since it has the disadvantage that the response is several orders of magnitude slower than that for compression tuning. However, the thermal tuning effects of microspheres can be more interesting than compression tuning. Heating can occur from intracavity material absorption when a WGM is on or near resonance, or from external sources. Intracavity absorption heating leads to the interesting phenomenon of thermal bistability. External sources include such things as a heat gun, thermal contact with other materials, or external radiation from a laser or other light source. In this chapter, an external laser is used to heat a microsphere to determine the thermal decay rate of the microsphere. This is used to determine the thermal conductivity of air as a function of pressure and the accommodation coefficient of air on fused silica. This experimental value of the thermal decay rate is then used to fit further experimental data to a thermal bistability model. The goal of this project is to understand how power dissipated in the microsphere affects observable measurements, determine acceptable power levels and scan rates, and measure material properties of the microsphere and surroundings.

Returning once again to equation (II.5), differentiating both sides with respect to temperature leads to the temperature-dependent frequency tuning result

$$\frac{dv}{dT} = -v \left[\frac{1}{n_s} \frac{dn_s}{dT} + \frac{1}{a} \frac{da}{dT} \right] \quad (\text{V.1})$$

The shift due to the polarization dependent term is negligible compared to the changes in index of refraction and radius terms and is excluded, giving each polarization approximately the same shift. The change in index of refraction with temperature for fused silica, as given in reference [56], is slightly wavelength dependent and the change in radius is given by the coefficient of thermal of expansion of fused silica^[57]. At a wavelength of 1550 nm near room temperature the two values are

$$\frac{1}{a} \frac{da}{dT} = \alpha_{\text{expansion}} = 5.5 \times 10^{-7} / \text{K} \quad \text{and} \quad \frac{dn_s}{dT} = 11.3 \times 10^{-6} / \text{K} \quad (\text{V.2})$$

This results in a WGM frequency shift of 1.6 GHz/K. With an index of approximately 1.45, the shift is dominated by the change in index of refraction, which accounts for over 93% of the shift. The tuning is verified experimentally by observing the frequency shift of WGMs while controlling the temperature of a microsphere. For the scan shown in Figure V.1, a 700- μm diameter microsphere was mounted in a compression tuner with no pressure applied to the microsphere. The tuner used had no upper and lower steel compression pads, only aluminum, for maximum heat transfer between the tuner arms and the microsphere. Heaters were attached to the tuner on the top and bottom compression arms along with a thermocouple that monitors the temperature of the squeezer arms. The temperature is controlled to a set value automatically by a microprocessor-based temperature controller. Fiber coupling is employed with the TDL, which is scanned over 10 GHz at 1550 nm. The initial 85° F

temperature is lowered to 77° F and then raised to 90° F with scans acquired at 1° F intervals. Figure V.1 shows the two 85° F scans are slightly frequency shifted from one another, showing there is some error involved in the process. However, performing a linear fit of temperature versus the WGM frequency position for both the increasing and decreasing temperature yields an average temperature tuning of 1.60 GHz/K, in excellent agreement with the predicted result.

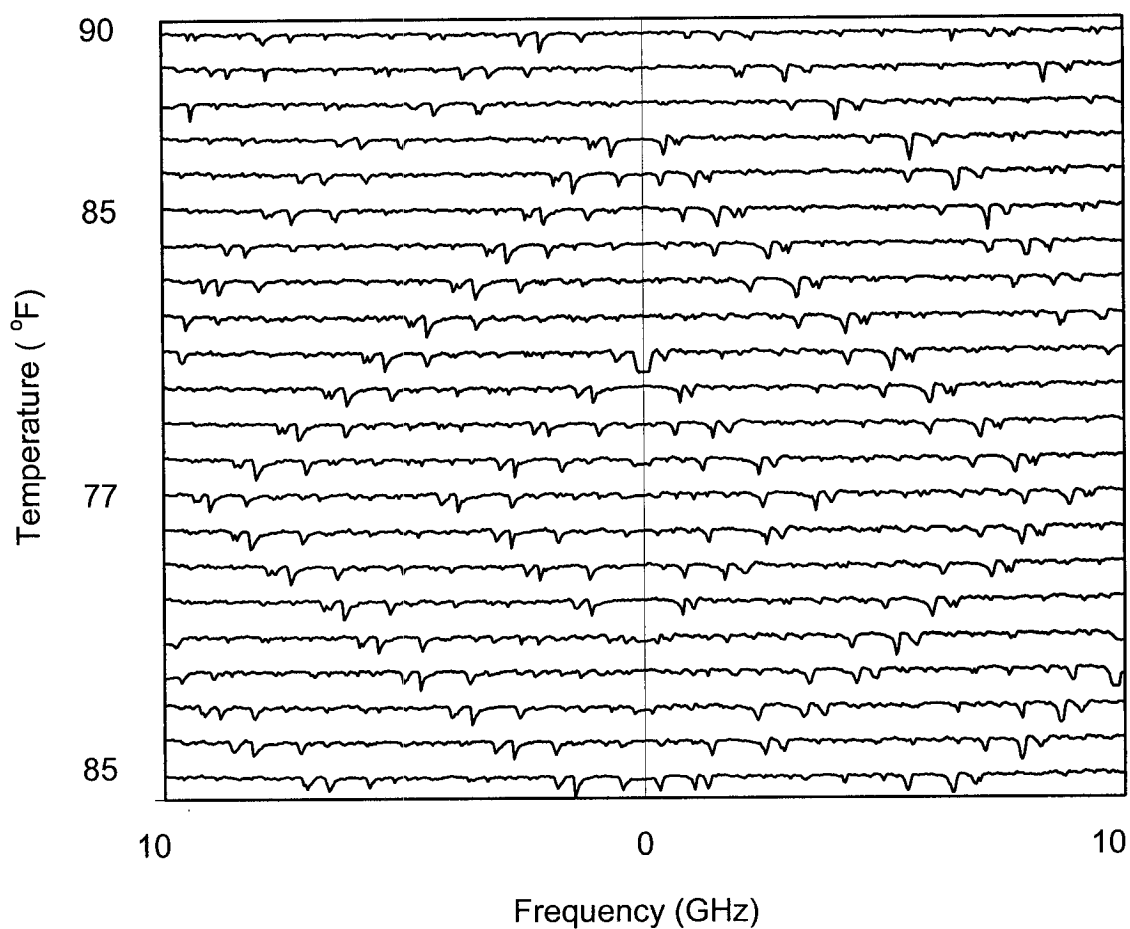


Figure V.1 WGM temperature tuning. Each successive scan is changed by approximately 1° F to show the temperature dependence of WGMs for a 700- μ m diameter microsphere; the baseline for each scan is offset. A 10 GHz scan range is shown, decreasing followed by increasing frequency.

2. Thermal Conductivity of Air

(a) Theory

The theory used in this chapter incorporates two simplifying assumptions. The first is that the temperature of the microsphere is uniform, no matter how it is heated. This is valid, since internal thermal relaxation is so much faster than the cooling processes described below that it can be neglected.^[58] The second assumption is that the microsphere has no eccentricity. As will be seen, the microspheres actually used were quite prolate. Somewhat better agreement between theory and experiment can be achieved by properly accounting for this prolateness, but doing so makes the theory much more complicated. The simpler treatment will be presented in the interest of clarity, and perfect spheres will be assumed.

As the microsphere cools, heat is lost due to convection, conduction into the stem, radiation, and conduction into the air. In contradiction to earlier claims,^[24] convection loss is the smallest of these losses for the temperature range and microsphere sizes used in these experiments,^[59-61] and is therefore ignored. Conduction losses into a small-diameter microsphere stem are also negligible when compared with radiation and air conduction. The rate of heat loss is given by

$$\frac{dQ}{dt} = mc \frac{dT}{dt} = -4\pi a k_{air} T - 4\pi a^2 \sigma \epsilon \left((T + T_{rm})^4 - T_{rm}^4 \right) \quad (\text{V.3})$$

where m is the microsphere mass, $c = 0.741 \text{ J}\cdot\text{g}^{-1}\cdot\text{K}^{-1}$ is the specific heat of fused silica, a is the microsphere radius, k_{air} is the thermal conductivity of air, $\epsilon = 0.87$ is the emissivity of fused silica, T is the microsphere's temperature above room temperature, T_{rm} is room temperature in Kelvin, and σ is the Stefan-Boltzmann constant. The first term on the right hand side of equation (V.3) is the rate of heat loss from thermal conductivity and the

second term is the radiative losses of the microsphere. When $T \ll T_{rm}$, this can be simplified to

$$\frac{dT}{dt} = -\frac{T}{\tau} \quad (\text{V.4})$$

where the thermal relaxation time τ , is given by

$$\tau = \frac{a^2 \rho c}{3k_{air} + 12\pi a \epsilon \sigma T_{rm}^3} \quad (\text{V.5})$$

where ρ is the density ($2.20 \text{ g}\cdot\text{cm}^{-3}$). If the thermal relaxation time is known, the thermal conductivity of air can be determined. The thermal conductivity of air at pressure p is related to that at atmospheric pressure by^[62]

$$k_{air} [p] = \frac{k_{atm}}{1 + \frac{g[p]}{a}} \quad (\text{V.6})$$

where k_{atm} is the thermal conductivity of air at atmospheric pressure ($0.0259 \text{ W}\cdot\text{m}^{-1}\cdot\text{K}^{-1}$), a is the radius of the microsphere, and g is the temperature jump distance given by

$$g[p] = \left(\frac{2-\alpha}{\alpha} \right) \frac{\left(2\pi \frac{R}{M} T_s \right)^{\frac{1}{2}} k_{atm}}{(\gamma+1)c_v p} \quad (\text{V.7})$$

where α is the thermal accommodation coefficient, $\frac{R}{M} = 287 \text{ J}\cdot\text{kg}^{-1}\cdot\text{K}^{-1}$ is the gas constant

for a unit mass of air, $\gamma = \frac{c_p}{c_v}$ is the ratio of heat capacities at constant pressure and

volume, respectively ($\gamma = 1.40$ and $c_p = 1.01 \times 10^3 \text{ J}\cdot\text{kg}^{-1}\cdot\text{K}^{-1}$ for air), $T_s = T + T_{rm}$ is the temperature at the surface of the microsphere, and p is the pressure. The pressure dependence of the thermal conductivity of air is derived for a sphere using the temperature-jump method described in Reference [63]. (Our pressures are not low

enough to reach the free-molecular-flow regime.)

(b) Experimental Setup

To determine the thermal conductivity of air at different pressures it is necessary to heat the microsphere above the ambient air temperature. Theoretical analysis becomes complicated if heating is performed by the thermal heater attached to the microsphere compressor or any other method that requires contact with the microsphere since the cooling rate would depend on the thermal conductivity of air and the contact material. For this reason, microsphere heating was performed by passing a focused beam from the Millennia laser onto the sphere from above. The power ranged from 0.2 watts to 5.5 watts. At lower pressures, shifts of up to 100 K were possible, however the typical shifts used for this experiment were kept in the range of 3-5 K.

In order to determine the thermal decay rate it is necessary to determine the relative temperature of the microsphere at several points in time. Using low incident power levels between 0.2 - 0.3 mW from the TDL to excite WGMs avoids significant internal heating of the microsphere. and allows changes in temperature to be determined from the WGM frequency shift between consecutive scans. Here, the WGM resonances are not the focus of study, but a tool. The dip depth is not important and the linewidth is only important in that it sets the frequency position resolution and therefore the temperature resolution.

Two microspheres were used in the thermal conductivity experiment. Both were prolate and fabricated using the H-O torch. One had an equatorial diameter of 340 μm , an axial diameter of 380 μm , and a stem diameter of 10 μm . The other had an equatorial

diameter of 140 μm , an axial diameter of 185 μm , and a stem diameter of 20 μm . The size parameters were determined by digital photography through a 45 \times microscope and have an error of approximately $\pm 5 \mu\text{m}$.

A vacuum chamber, specially designed for microsphere experiments, was used to perform scans at different pressures. A schematic of the top view of the chamber is shown in Figure V.2. The chamber is constructed from clear Plexiglas. This material was chosen since it is easily machined and permanent components can be epoxied into place. It also makes optical alignment easier since visible inspection of the experimental setup inside the chamber is possible from many different vantage points. A negative aspect of using Plexiglas instead of a metal, such as steel or aluminum, is the rigidity of the system. When air is evacuated from the chamber a larger force is imparted inward on the walls of the chamber, 14.7 lb/in², causing small changes in the shape and position of the chamber walls and components attached to them. A relative scale of the positioning tolerance of the microsphere is the maximum gap distance between it and a coupling prism or tapered fiber, typically a fraction of a micron. When performing experiments that compare effects at different parameter settings, such as pressure, it is crucial that all extraneous variables are minimized, especially position.

The side wall of the chamber is made from a 10-inch outer diameter cylinder that has $\frac{1}{4}$ inch thick walls and is 4 inches high. The $\frac{1}{2}$ inch thick base is permanently fixed to the side wall and is mountable to an optical table with screws that are external to the chamber. A base plate with $\frac{1}{4}$ -20 holes spaced one inch apart is allowed to rest freely on legs inside the chamber. Optical components mounted on this plate do not move with respect to each other as the plate moves. Placing as many components as possible on this

base minimizes the effects of the pressure-dependent positioning problem. The $\frac{1}{4}$ inch thick removable top seals to the chamber with an o-ring and has eight equally spaced screws around the external perimeter to apply pressure for sealing.

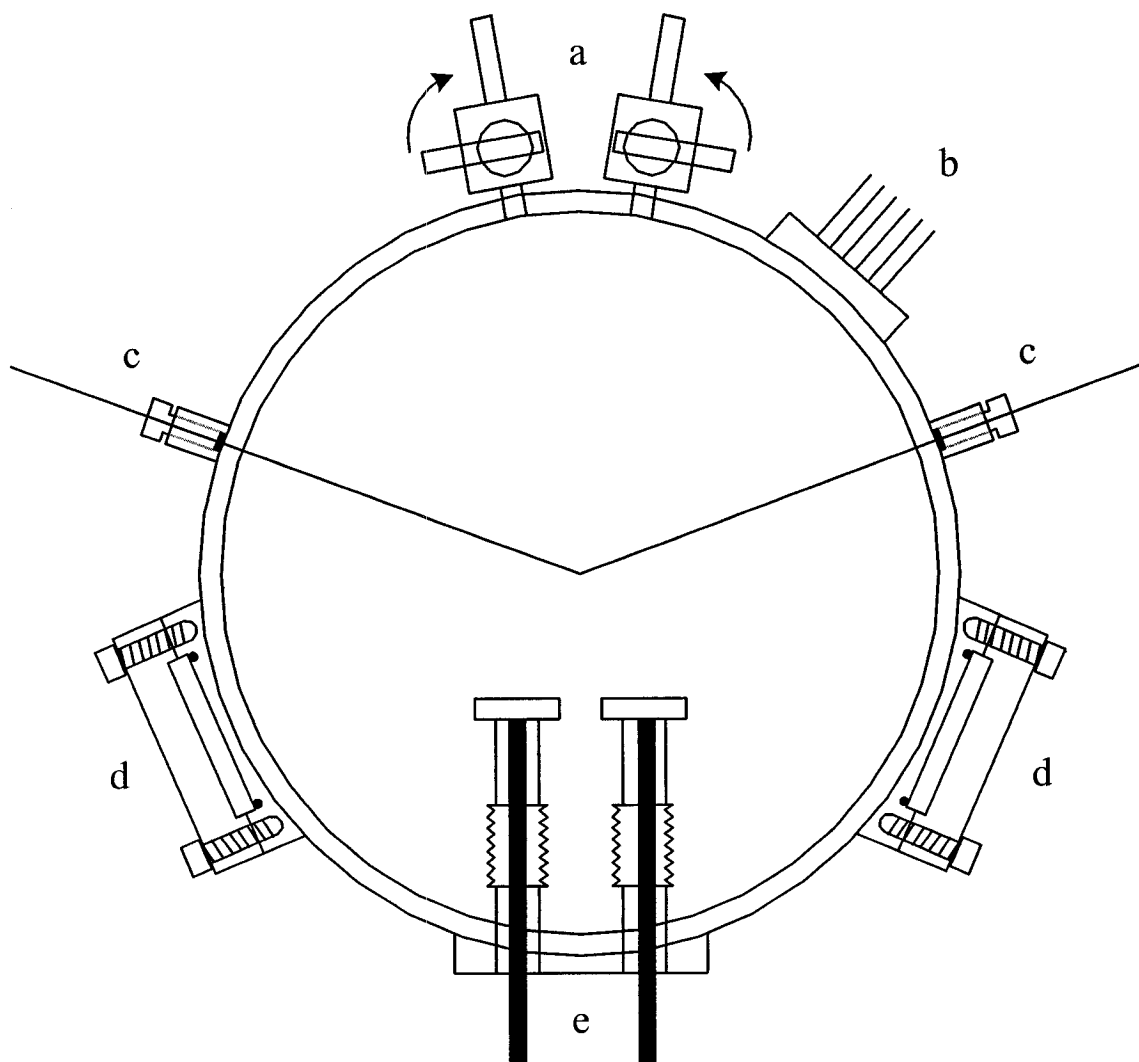


Figure V.2 Top view of the vacuum chamber used for performing pressure-dependent experiments or trace-gas detection. (a) Manual vacuum control valves. (b) Thermocouple and electrical feedthrough. (c) Fiber optic feedthrough. (d) 2" diameter optical windows. (e) Bellows tubing and rods for internal positioning from outside the chamber.

All of the following components are sealed to the chamber with o-rings and removable for repair or replacement if necessary. The chamber includes two optical windows and two fiber optic feed throughs in order to facilitate both prism and fiber coupling. The optical windows are 2 inches in diameter, $\frac{1}{4}$ inch thick, and have no optical coating. The fiber is fed through a $\frac{1}{16}$ inch thick by $\frac{1}{4}$ inch diameter piece of rubber that has a small hole in it. In Swagelok fashion, this piece is compressed by screwing in an outer cap into a part mounted through the chamber wall, making a seal between the fiber and rubber, and the chamber and rubber. There are two valves to regulate the flow of air or gas in and out of the chamber. There is also a section containing thermocouple and electrical feedthroughs for use with the microsphere compressor described in Chapter IV. In order to control the position of objects inside the chamber while sealed, two bellow tubes are mounted to the chamber wall. A rigid rod is connected to the far end of each tube and extends out of the tubing by several inches in order to be connected to a three-dimension translation stage. The flexibility of the bellows tubes allows for three-dimensional control of objects inside the chamber. The original idea was to control the position of the prism or tapered fiber relative to the microsphere; however, due to the fact that a large amount of force is placed on the chamber, the bellows tubing, and the positioning rods when the chamber is under vacuum, a constant position is not possible while varying the pressure. This is remedied by placing a three dimensional translation stage inside the chamber, mounted on the same floating base plate that the microsphere is on, ensuring that changes in the observed WGM signal caused by changes in position are minimized.

With the tapered fiber mounted on the translation stage inside the cavity, both

ends of the fiber are passed through the cavity walls and a microsphere is mounted near the tapered fiber. The chamber lid is sealed after the microsphere and taper are placed in contact and WGM resonances are observable at the output signal.

At a set pressure, the Millennia laser is focused on the microsphere, raising the temperature several degrees above room temperature. The TDL is scanned over a range of 8 GHz at a frequency of 5, 10, or 20 Hz. To begin recording at the moment the microsphere begins to cool, data recording is triggered when the heating laser is turned off. The maximum number of points collected during a scan is limited to 250,000. With decay times on the order of a second there is a tradeoff between frequency resolution and scan rate. Typically, as the microsphere cools, the throughput of the fiber is recorded continuously over several scans for a period of 5 or 10 seconds. Figure V.3 is for the larger microsphere at 350 mTorr showing several consecutive scans plotted together as the microsphere cools. The scans are initially decreasing in frequency then, at the center of the plot, the scan direction is reversed. As time progresses, the prominent mode moves toward increasing frequency in both the decreasing and increasing frequency scan directions. The frequency shift decreases exponentially to its equilibrium room temperature value. The frequency shifts are recorded and converted to temperature shifts using the 1.6 GHz/K, giving one set of data for the increasing scan frequency and another for the decreasing scan frequency. The temperature is plotted on a log scale in Figure V.4 as a function of time, where the time for each point is determined from the laser scan frequency and the relative WGM frequency positions between scans. Two different values for the thermal decay rate τ are found for the different data sets. This difference can be mostly, if not entirely, attributed to the laser scan hysteresis; when interpreting the

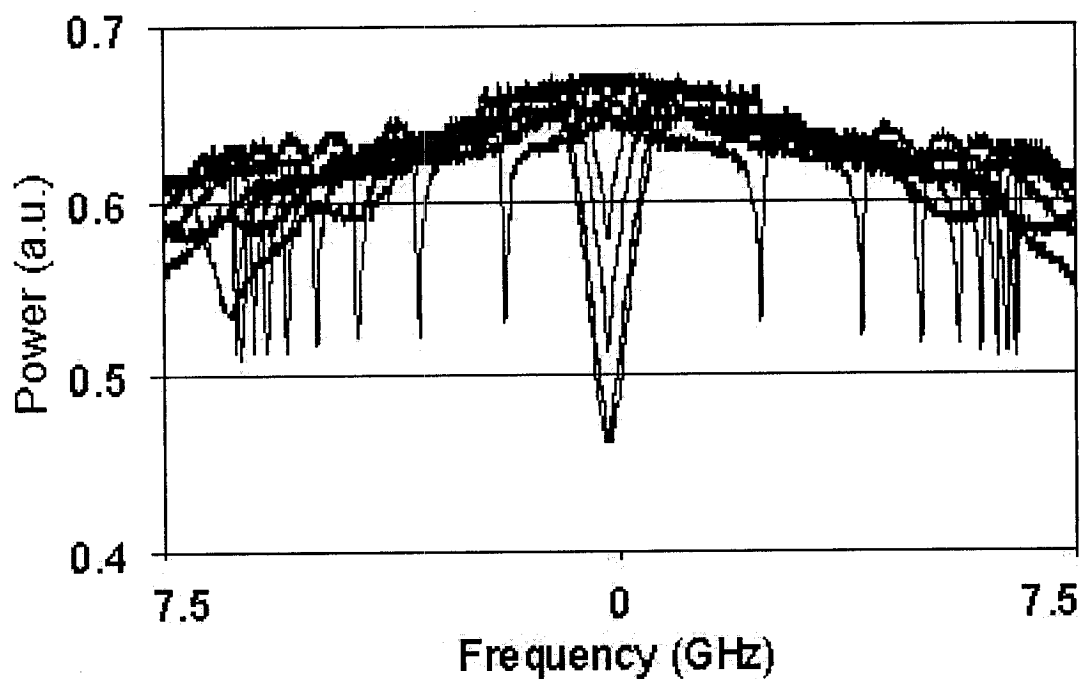


Figure V.3 Consecutive laser scans swept back and forth at a rate of 5 Hz. The shift in resonance frequency is used to determine the rate of change of temperature.

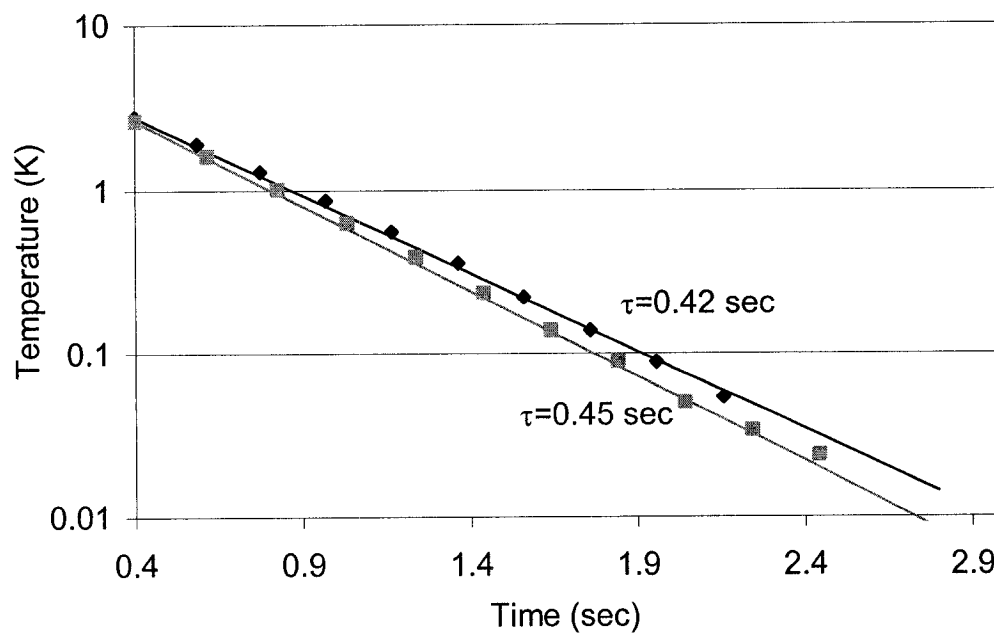


Figure V.4 Log plot of temperature above equilibrium vs. time at 350 mTorr for increasing and decreasing scan direction (light and dark lines respectively). The straight lines are fitted to the data points, and give the thermal decay times, $\tau = 0.45$ sec and $\tau = 0.42$ sec.

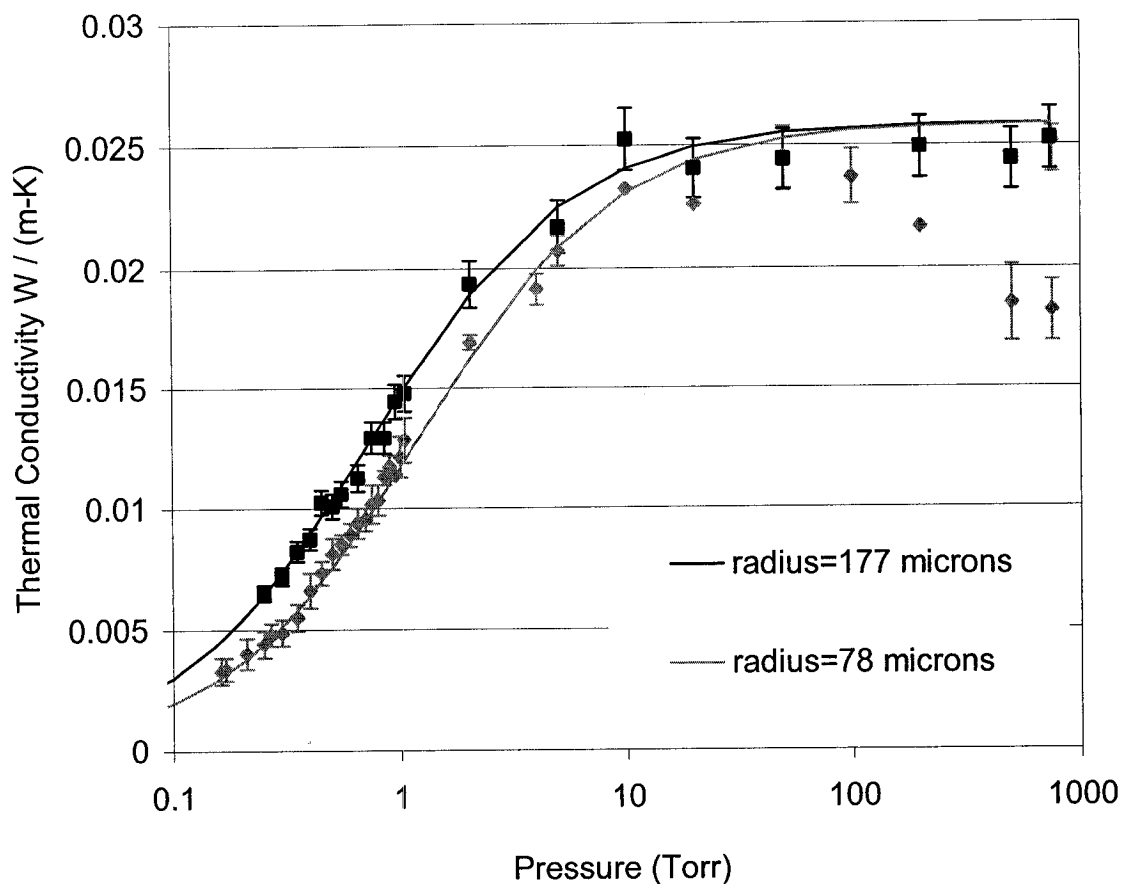


Figure V.5 Pressure vs. thermal conductivity for two different spheres plotted against a theoretical curve.

data it was assumed the laser frequency is scanned linearly in time. Without simultaneously collecting data from a spectrum analyzer, the exact frequency differences are not known. Since the hysteresis curves are in the opposite directions, it is a good estimate to use the average of the high and low values.

The process of determining the thermal decay rate is performed at different pressures in the range of 0.1-760 Torr. Using equation (V.5), the thermal conductivity is determined from the thermal decay rates. The experimental thermal conductivity for both microspheres is plotted along with theoretical curves in Figure V.5. The theoretical

curves are fit by varying the only free parameter; the accommodation coefficient α is determined to be 0.93 and 0.76 for the small and large spheres respectively. It may not be reasonable to compare the two numbers for the different microspheres since the accommodation coefficient is dependent on how the surface of the microsphere is prepared. The typical value range for air on glass is 0.8-0.85, and the value of CO₂ nitrous oxide (NO₂) are the same for fused silica as on glass.^[64] The error bars for the small microsphere are determined by calculating the thermal conductivity using the high and low thermal decay times. The error bars for the larger microsphere are given by $\pm 5\%$, the approximate value of the error bars for the smaller sphere. The data points for the smaller diameter microsphere in the 100 to 1000 Torr region appear to have a lower thermal conductivity value than is predicted. A second data point at the highest pressure value is also present, but is not easily seen because it is roughly the same value as that found for the larger microsphere. The most probable reason for this deviation is that the microsphere stem was heated to a significant temperature when the microsphere was heated. This is possible because the heating laser is incident on the top of the microsphere, opposite the stem, making focusing of the laser beam to a small spot size possible. This extra heat would cause the microsphere to cool slower, making the decay time look longer and the thermal conductivity of air lower.

3. Thermal Bistability

(a) Introduction

The term thermal bistability refers to the microsphere's reflection signal being dependent on the scan direction of the laser frequency due to heating from intracavity

absorption. Presented here is a qualitative description, followed by a model and experimental results.

As depicted in Figure V.6(a), the laser is initially far off resonance with a WGM as it is scanned in the direction of increasing frequency. As the laser frequency approaches the WGM resonance, power is coupled into the microsphere. A fraction of this power is absorbed, heating the microsphere and shifting the resonance frequency downward, as given by equation (V.1), opposite the scan direction. The resonance frequency will continue to shift downward until the amount of power absorbed is less than the heat lost, occurring at or past resonance. After this point, the microsphere cools and the resonance frequency shifts upward, following the direction of the laser. This creates an asymmetric dip with an apparent linewidth that is smaller than the actual linewidth. This effect is seen in the experimental results presented later in this chapter.

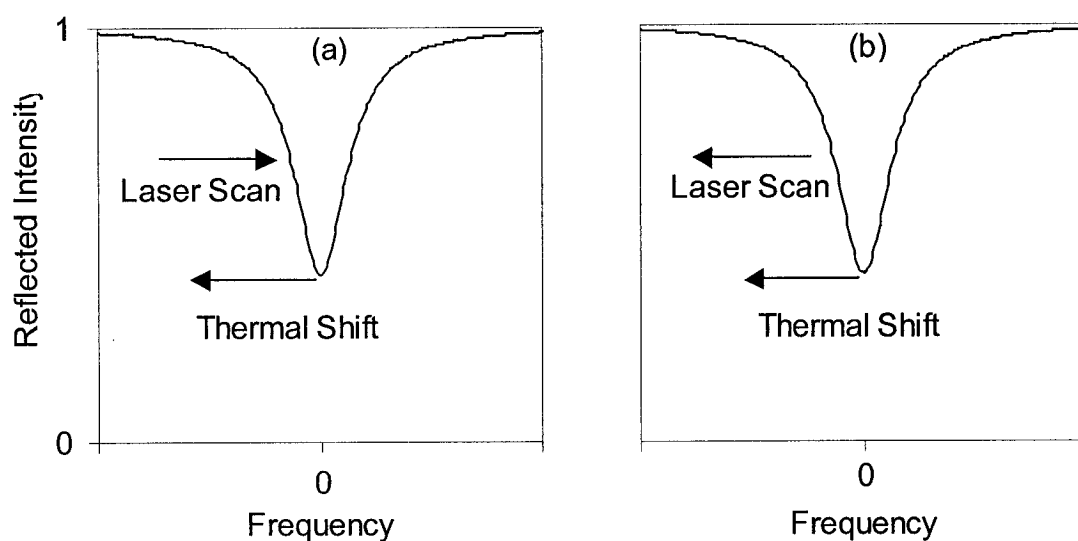


Figure V.6 Representation of thermal bistability for different scan directions. (a) The laser scan direction and WGM resonance shift are in opposite directions. (b) Same direction.

After passing completely through the WGM resonance, the laser scan direction is reversed to scan in the direction of decreasing frequency, as shown in Figure V.6(b). Once again, as the laser nears the WGM resonance, a portion of the power coupled into the microsphere is absorbed, shifting the resonance frequency in the same direction as the laser scan, extending the observed mode over a larger frequency range. Eventually, the rate at which the microsphere absorbs heat becomes less than the rate at which it dissipates it. When this occurs, the microsphere cools and the resonance frequency shifts upward, back to its original frequency. The dip is again asymmetric, but more visible since the apparent linewidth is larger than the actual linewidth. This effect is also seen in the experimental results presented later in this chapter.

(b) Theory

The thermal bistability can be modeled and tested experimentally with minimal free parameters. Equation (II.25) shows the reflection signal of a WGM can be described as one minus constant times a Lorentzian, where the Lorentzian corresponds to the total loss of the signal. In terms of power, this can be expressed as

$$P_{reflected} = P_{inc} - P_{lost}[\nu] \quad (V.8)$$

The power lost written as a Lorentzian is

$$P_{lost}[\nu] = P_o \frac{\left(\frac{\Delta\nu}{2}\right)^2}{(\nu - \nu_0[T])^2 + \left(\frac{\Delta\nu}{2}\right)^2} \quad (V.9)$$

where P_o is the maximum power lost, $\Delta\nu$ is the WGM linewidth, and ν_0 is the resonance frequency that is a function of temperature. Setting the initial resonance frequency to

zero makes ν a measure of how far the laser is from the resonance frequency if no heating took place. This makes $\nu_0[T] = -bT$, where T is the temperature change of the microsphere from the initial equilibrium temperature and $b = 1.6$ GHz/K at 1550 nm. Both the laser frequency and the temperature are time dependent. The laser frequency is assumed to be driven by a triangle wave and scanned linearly, as defined by

$$\nu[t] = \pm \left(2Aft + \frac{A}{2} \right), \quad (\text{V.10})$$

where A is the frequency scan distance, f is the laser scan frequency, and the sign indicates the scan direction.

The difference between the heat flow into and out of the microsphere gives the total change in heat,

$$\frac{dQ}{dt} = mc \frac{dT}{dt} = P_{\text{absorbed}} - 4\pi a k_{\text{air}} T - 4\pi a^2 \sigma \varepsilon \left((T + T_{\text{rm}})^4 - T_{\text{rm}}^4 \right) \quad (\text{V.11})$$

The first term on the far right hand side is from the heat gained per unit time, the second term is the rate of heat loss from thermal conductivity, and the third term is the radiative losses of the microsphere. From this, the time dependence of the microsphere's temperature is expressed as

$$\frac{dT}{dt} = \frac{\beta P_{\text{lost}}[\nu]}{mc} - \frac{B}{mc} T \quad (\text{V.12})$$

where β is the fraction of the lost power absorbed, as opposed to scattered, and B is the rate of heat loss per unit temperature, where for small changes in temperature

$$B = \frac{mc}{\tau} = 4\pi a k_{\text{air}} + 16\pi a^2 \sigma \varepsilon T_{\text{rm}}^3 \quad (\text{V.13})$$

Substituting equations (V.9) and (V.10) into equation (V.12) yields the single differential equation

$$\frac{dT}{dt} = \frac{\beta P_o}{mc} \frac{\left(\frac{\Delta\nu}{2}\right)^2}{\left(bT \pm \left(2Aft + \frac{A}{2}\right)\right)^2 + \left(\frac{\Delta\nu}{2}\right)^2} - \frac{BT}{mc}. \quad (\text{V.14})$$

Once a solution to this equation is obtained, the temperature value at a given time is substituted into equation (V.9) to give the power loss at that time. The easiest method of obtaining a solution to equation (V.14) is numerically. The theoretical fits to the collected data in the next section are performed numerically with the mathematical computation program Mathematica.

(c) Experimental Setup and Results

Once again, the experiment was performed using fiber coupling inside the vacuum chamber in order to control the pressure and further test the results of the thermal conductivity measurements. Controlling the power (P_o), laser scan distance (A), laser scan frequency (f), and using a WGM with a known linewidth ($\Delta\nu$), leaves only two free parameters in equation (V.14), B and β . Using the same 350- μm diameter microsphere as in the thermal conductivity experiment makes it possible to use the experimental value of B determined above leaving only one free parameter to fit. It is worth noting that by using the experimentally determined value of B , any effects of heat loss through the stem or any other methods are included. This means that any error in fitting the thermal conductivity is not important here. By finding the value of β , the amount of power lost due to absorption compared to that of scattering will be known, and hence the effective absorption coefficient of the microsphere will be known. The absorption coefficient need not be that for fused silica. Contaminants introduced during fabrication are a concern,

along with those introduced afterwards, such as dust and water vapor adsorption to the microsphere surface.

Figures V.7 and V.8 are scans of the same WGM at a wavelength of 1575 nm, but with different combinations of pressure and laser scan rate, as given in Tables V.1 and V.2 respectively. The dark smooth curves are theoretical fits to the collected data which are the lighter curves. The data is plotted as a function of the laser frequency, where zero is the resonance frequency position if no heating took place. Arrows next to the scans indicate the laser scan direction. The reflected power is plotted in milliwatts, where the baseline of each data set has been shifted downward so the top data set in each figure is at zero and each subsequent data set is further offset downward by 0.15 mW. The total power transmitted through the tapered fiber without a microsphere present was 2.0 mW. The 43 MHz linewidth of the mode is found by rapidly scanning the laser so no thermal effects are present to change the apparent linewidth, as in Figure V.8(d). The B , and hence k , value is taken from the thermal conductivity experiment.

The three data sets displayed in Figure V.7 are acquired at different pressures with the same scan rate. Here, the increased thermal decay time, due to the thermal conductivity dependence on pressure, is seen as a larger hysteresis at lower pressure. Notice the single free parameter, β , varies by only six percent. The predicted resonance frequency shift to lower frequencies for both scan directions is easily seen in all three of the scans.

The four data sets displayed in Figure V.8 are acquired at the same pressure and different scan rates. By comparing data set (a) to (d) the change in apparent linewidth is obvious, narrower when the laser is scanning in the direction of increasing frequency and

wider in the direction of decreasing frequency.

The intrinsic loss coefficient (α_i) and transmission coefficient (T_l) are determined from the Q and dip depth using the model in Chapter II. There are two possible solutions, 1.29 m^{-1} and 0.0213 m^{-1} , for the undercoupled and overcoupled cases respectively. The large difference between the possible solutions is expected since the overcoupled case has a much higher intracavity power, especially since the mode is grossly overcoupled or undercoupled. The intrinsic loss coefficient and the absorption coefficient of the microsphere are related to each other by $\alpha_{abs} = \beta\alpha_i$. Using $\beta=0.087$ the absorption coefficient is either 0.11 m^{-1} or 0.0018 m^{-1} . Comparing these to the absorption coefficient of fused silica given in Table III.1, shows that both solutions are possible with the overcoupled solution being two orders of magnitude larger. By looking at the dip depth of the surrounding modes and considering that the transmission coefficient of an overcoupled mode would have to be very large for such a shallow dip, it is most likely that the mode is undercoupled. This leaves the problem that the absorption coefficient is about five orders of magnitude larger than the material absorption of fused silica.

Water adsorption to the microsphere surface must be considered as a contributing factor to the large absorption coefficient. Reference [30] gives the equation

$$Q_w \sim \sqrt{\frac{\pi}{8n^3} \frac{Diameter^{1/2}}{\delta\lambda^{1/2}\beta_w(\lambda)}} \quad (\text{V.15})$$

where δ is the water layer thickness, and $\beta_w(\lambda)$ is the bulk water absorption coefficient at the specified wavelength. With the Q dominated by this water loss, an estimate gives $Q \sim 3 \times 10^7$ and an effective loss coefficient of 0.18 m^{-1} for the $350 \text{ }\mu\text{m}$ diameter microsphere at 1570 nm , $\delta = 0.2 \text{ nm}^{[29]}$ corresponds to one to two monolayers, and $\beta_w \sim 800 \text{ m}^{-1}$ for

bulk water^[65, 66] at this wavelength. It is pointed out in Reference [25] that this model for the limiting Q value attributed to water absorption is not accurate for all wavelengths, but works reasonably well for the 1319 nm range. Reference [30] includes two experimental points of reference for water-limited Q s as $Q \sim 10^9$ at 670 nm with $\beta_w \sim 0.4 \text{ m}^{-1}$ and $Q \sim 10^8$ at 1319 nm with $\beta_w \sim 500 \text{ m}^{-1}$. This demonstrates the absorption coefficient result for the undercoupled case is not as bad an estimate as first believed. On the other hand, using our own method for estimating Q_w gives a value of α_{abs} for single-monolayer water coverage that is consistent with the value found assuming overcoupling. In either case, the value found here places a practical limit on the Q of microspheres that have no special steps taken to protect them from water vapor.

The significance of the results presented in this chapter is in their ability to characterize surface properties of the microsphere. The method of determining the thermal accommodation coefficient that is presented here has never been used before. This coefficient characterizes the interaction of ambient gas molecules with the surface. The observation of thermal bistability allows us to determine how much of the total loss results from absorption, and find the adsorbed water coverage.

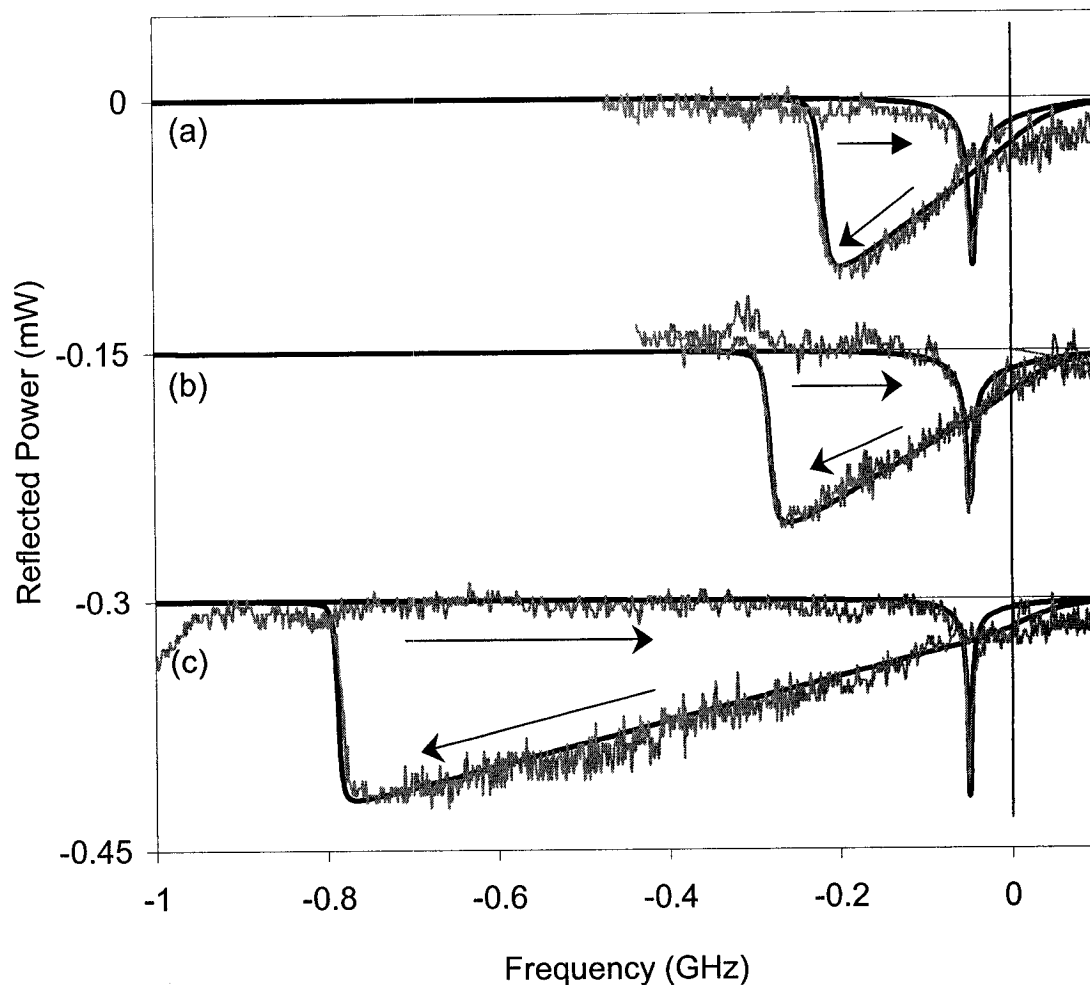


Figure V.7 Thermal bistability of the same WGM at the same laser scan frequency at varying pressure. The parameters are listed in Table V.2. The linewidth of the WGM is 43 MHz. The arrows indicate the direction of the scan. The dark curves are theoretical fits to the lighter experimental data.

Table V.1 Summary of parameters for Figure V.7.

Scan	f (Hz)	p (Torr)	k ($\text{W m}^{-1} \text{K}^{-1}$)	B (W m K^{-1})	β
a	.01	10.05	.0253	.0000583	0.084
b	.01	2.05	.0194	.0000451	0.082
c	.01	0.35	.0082	.0000202	0.087

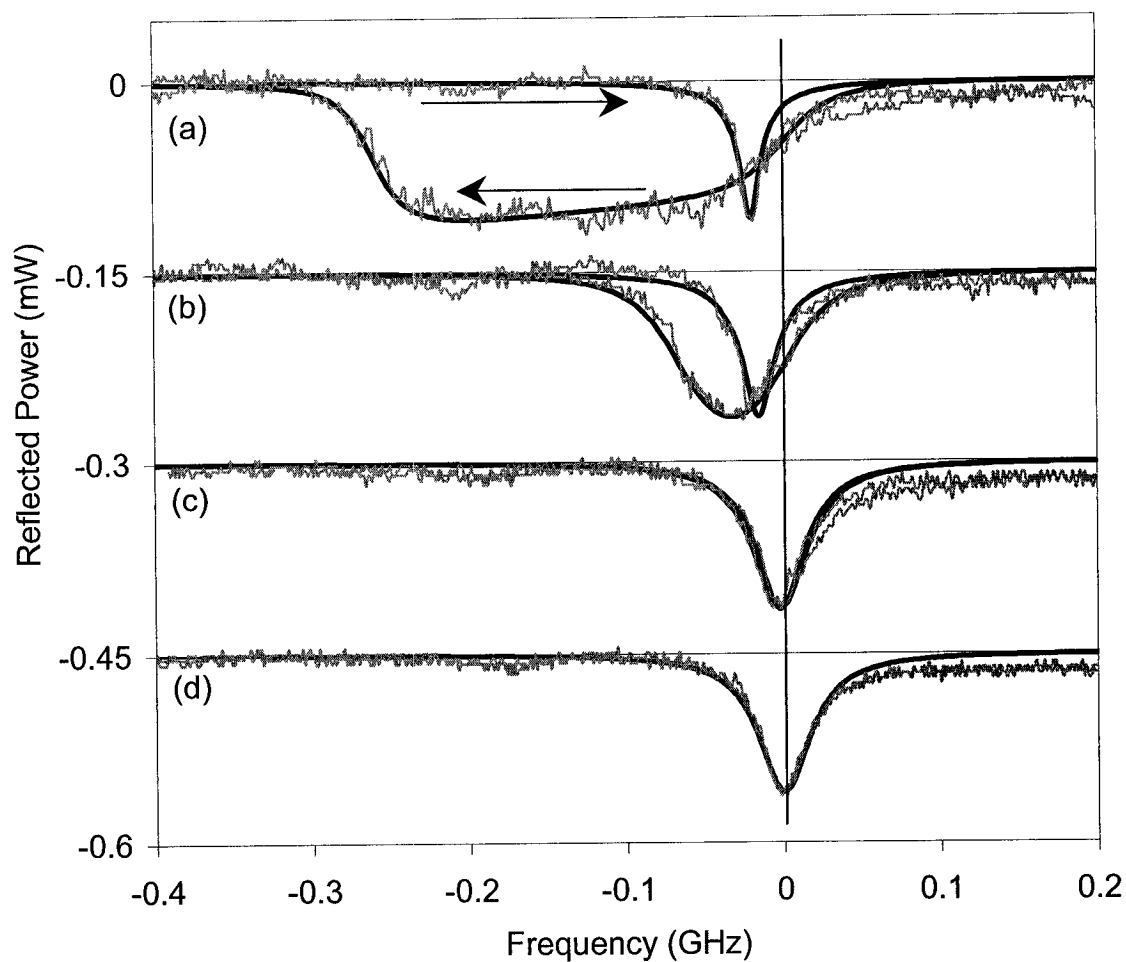


Figure V.8 Thermal bistability at different laser scan frequencies at 0.35 Torr. The parameters are listed in Table V.2. The linewidth of the WGM is 43 MHz. The arrows indicate the direction of the scan. The dark curves are theoretical fits to the lighter experimental data.

Table V.2 Summary of parameters for Figure V.8.

Scan	f (Hz)	p (Torr)	k ($\text{W m}^{-1} \text{K}^{-1}$)	B (W m K^{-1})	β
a	0.05	0.35	.0082	.0000202	.087
b	0.1	0.35	.0082	.0000202	.087
c	1	0.35	.0082	.0000202	.087
d	100	0.35	.0082	.0000202	.087

CHAPTER VI

MICROSPHERES AS SENSORS

1. Introduction

It has been shown in Chapter V that microspheres can be used as temperature sensors. When utilizing the highest Q values for microspheres, their sensitivity is on the order of microKelvin and spans a range of hundreds of Kelvin. Sensors also play other roles, including liquid chemical detection and trace gas detection. Examples include monitoring CO₂ and other atmospheric trace gases,^[67-69] industrial pollutants, biological and chemical warfare agents, and water contaminants.

In the previous chapter, the microsphere WGMs were used as a temperature sensor to monitor the microsphere's interaction with the surrounding atmosphere. Once again, a microsphere will be used as a sensor to probe its surroundings, but with a different approach^[55, 70]. If the laser exciting a microsphere WGM is at an absorption resonance frequency of a molecule that enters the evanescent field of the microsphere, the overall effective loss of the microsphere will increase as the concentration of the absorber is increased. This increase in loss causes the Q of the cavity^[71] to decrease and the dip depth to change. The Q is typically determined by measuring the linewidth of the WGM. However, it has been demonstrated that both thermal effects and laser scan hysteresis can influence the apparent linewidth of the cavity. Additionally, methods that utilize the change in cavity decay time to determine the change in Q factor, like cavity-ringdown

measurements, require laser gating and fast detectors, adding another degree of difficulty. Observing changes in dip depth is an alternative that is free from these problems and can be found from one direct measurement.

The use of evanescent waves as optical absorption sensors typically involves total internal reflection^[72, 73] or guided waves, as in the case of tapered fibers.^[55, 72, 74, 75] With the growing popularity of microresonators, their evanescent fields have also been proposed for use as sensors.^[71, 76, 77] Microspheres have several advantages over other detection methods. The large effective path lengths of these submillimeter cavities make microspheres a good alternative to multipass cells, which have path lengths of tens of meters; additionally, small sample volumes are not a problem. One factor in determining the detection sensitivity of microspheres is the change in absorption compared to the actual loss; since the loss coefficient of fused silica is as low as $5 \times 10^{-5} \text{ m}^{-1}$ at 1550 nm, the potential detectable changes in absorption would be at least two orders of magnitude lower than this value for the direct absorption measurement scheme presented here. Unfortunately, the actual intrinsic loss of the microsphere is limited by other factors, like scattering and water adsorption on the surface of the microsphere. With enhanced preparation techniques, these factors can be minimized, making the detectable levels significantly lower than the experimental results presented in this chapter. For atmospheric measurements, such techniques might include heating the microsphere a significant amount, $\Delta T = 400 \text{ K}$,^[29] while keeping it in a dry atmosphere. However, this would not exclude the problem of water vapor introduced with the sample. It has also been suggested that a chemical treatment to prevent surface hydration be applied.^[29]

2. Theory

The theory for the liquid chemical detection and trace gas detection is similar. The following equations assume that there is only one coupler present, meaning there is no microsphere transmission signal. Using equations (II.13) and (II.23) with $T_3 = 0$, the measured dip depth and Q gives two possible solutions for the transmission and intrinsic loss coefficients. Again, the two solutions correspond to the WGM being overcoupled or undercoupled. For an increase in intrinsic loss by $\Delta\alpha$ the change in reflected intensity at $\phi = 0$ is given by

$$\frac{\Delta I_{reflected}}{I_{inc}} = \left(-4LT_1\Delta\alpha \frac{(T_1^2 - \alpha_i^2 L^2 - \alpha_i L^2 \Delta\alpha)}{(T_1 + \alpha_i L)^2 (T_1 + \alpha_i L + \Delta\alpha L)^2} \right). \quad (\text{VI.1})$$

For arbitrarily small changes in absorption, equation (VI.1) can be written as

$$\frac{dI_{reflected}}{d\alpha} = I_{inc} \left(-4LT_1 \frac{(T_1 - \alpha_i L)}{(T_1 + \alpha_i L)^3} \right), \quad (\text{VI.2})$$

where L is the circumference of the microsphere, and $d\alpha$ is the change in absorption experienced by the microsphere. The change in reflected intensity is negative when the WGM is overcoupled and positive when undercoupled, thus, knowing the sign of equation (VI.1) eliminates one of the possible solutions for T_l and α_i . This also leads to the conclusion that when performing experiments, the change in intrinsic loss should be kept small compared to the total intrinsic loss since it may be possible to drive the resonance through critical coupling.

In all of the experiments performed in our lab, the detection of added absorption from resonant molecules occurs in the evanescent mode volume, which is a fraction f of the total mode volume. Therefore, the change in intrinsic loss of the microsphere is the

absorption coefficient of the molecules (α_m) times the external mode fraction. Since f varies with the sphere size and WGM mode numbers, it is difficult to include in general numeric examples. However, the fact that f is larger for smaller microspheres makes smaller spheres the obvious choice for evanescent detection.

To evaluate the detection sensitivity of the microsphere in a more common manner, an effective detection path length is defined next. This path length is different from that defined in Chapter II, where the effective path length was associated with the total intracavity loss. That effective path length definition works well for determining the amount of power lost, however, it is not a good measure of detection sensitivity. Equation (VI.1) shows that at critical coupling the change in dip depth with changing absorption is a minimum. This fact is not represented in equation (II.19); therefore, an effective detection path length is defined. This new definition is a measure of the fractional change in the dip depth as the total loss of the WGM is changed changing the total absorption by a small amount $d\alpha$. This will serve as a measure of the sensitivity of the microsphere, with longer path lengths being more sensitive.

In general, Beer's Law gives the value of the intensity or power of a signal after passing through an absorbing medium of length L and can be written in the functional form

$$I(L) = I(0)e^{-\alpha_m L}, \quad (\text{VI.3})$$

where α_m is the absorption coefficient of the medium and L is the absorption path length.

Differentiating with respect to α_m gives

$$\frac{dI(L)}{d\alpha_m} = -LI(L), \quad (\text{VI.4})$$

which can be related to equation (VI.2). For the reflected signal, the change in the intensity dip depth is the quantity measured. This implies that the dip depth should correspond the $I(L)$ in equation (VI.4), where the dip depth M is given by equation (II.26) with $T_3 = 0$. Rewriting equation (VI.2) in terms of M and incorporating f , then equating it to equation (VI.4), also rewritten in terms of M , yields

$$-L_{det}M = \left(\frac{1}{\alpha_i} \frac{(T_1 - \alpha_i L)}{(T_1 + \alpha_i L)} \right) Mf \quad (VI.5)$$

This gives an effective detection path length

$$L_{det} = \frac{-1}{\alpha_i} \frac{(T_1 - \alpha_i L)}{(T_1 + \alpha_i L)} f \quad (VI.6)$$

Notice at critical coupling L_{det} is zero, making it the least sensitive point for detecting changes in absorption. When the mode is overcoupled, the change in the dip depth is toward a deeper dip, making it possible to have a negative effective path length by this definition. This definition is a better estimate for determining detection sensitivity of the reflected signal than the path length described in Chapter II.

The intracavity and effective detection path lengths along with the on-resonance reflection signal are plotted in Figure VI.1 for a 400- μm diameter microsphere with constant $\alpha_i = 0.01\text{m}^{-1}$. As the mode passes through critical coupling, the effective detection path length goes through zero, making the detection sensitivity nearly zero at this point. It then changes sign from positive to negative as the mode goes from being undercoupled to overcoupled.

Figure VI.2 is also a plot of the effective path lengths for a 400- μm diameter microsphere, where the transmission coefficient is held constant at 0.0015 and the

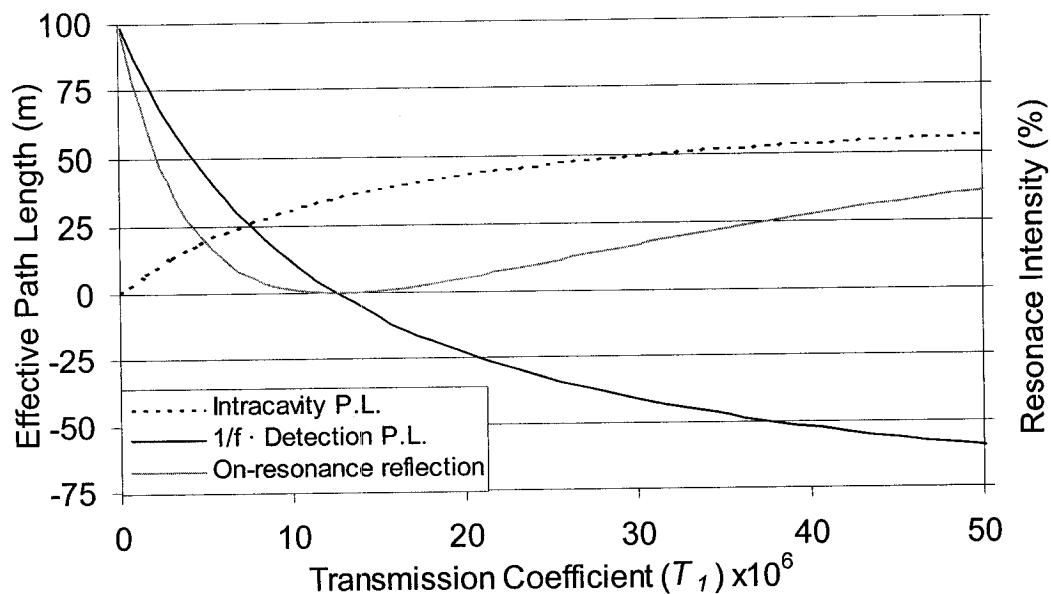


Figure VI.1 The effective path lengths associated with the intracavity path length and effective detection path length of a 400- μm diameter microsphere are plotted on the left hand axis. The detection path length is scaled by the external mode volume fraction. The reflection signal of the on-resonance WGM is plotted on the right hand axis. α_i is fixed at 0.01 m^{-1} .

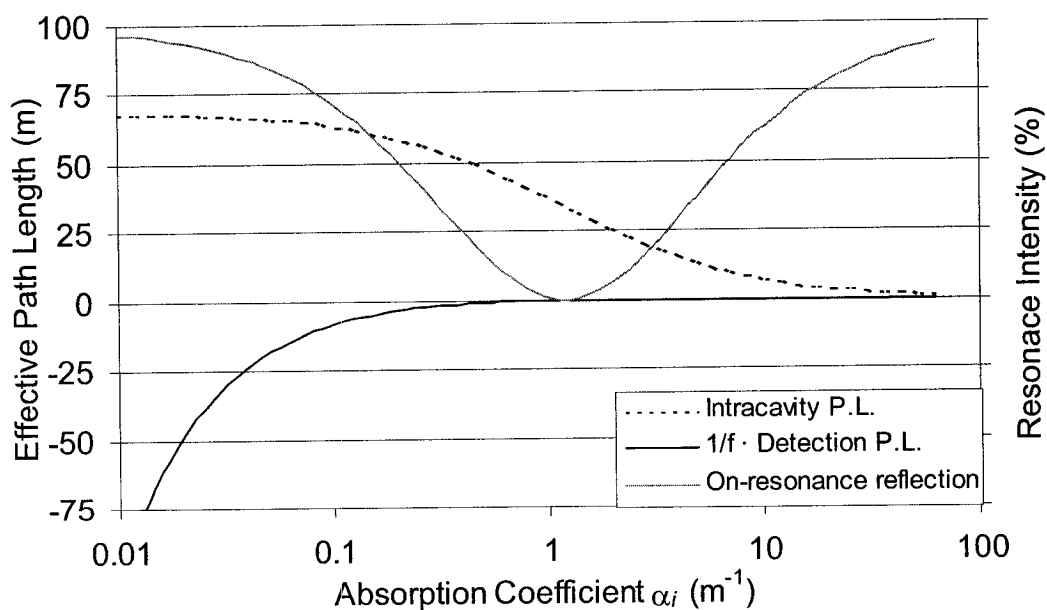


Figure VI.2 Same parameters as in Figure VI.1, only T_l is fixed at 0.0015 while α_i is varied.

intrinsic loss coefficient is allowed to vary. This may be more insightful for the experiments presented later in this chapter where the absorption is varied, as the microsphere and fiber are fixed in place, keeping a constant T_l value. As the loss coefficient is increased, the mode goes from overcoupled to undercoupled. Again, at critical coupling, the detection path length goes through zero. The advantage of this plot is that it shows how the effective detection path length, or detection sensitivity, is decreased as the total loss is increased.

3. Experimental Results

(a) Liquid Chemical Detection

A dye that is absorptive in the wavelength range of the Ti:sapphire or tunable diode laser is necessary to demonstrate liquid chemical detection. Both lasers are in infrared regions where not many dyes are available. Indocyanine green dye (ICG)^[78, 79] has high optical absorption in the near infrared, with the peak absorption around 790 nm, in the range of the Ti:sapphire laser. ICG dissolves in water or methanol, but in methanol, ICG degrades slower and is more stable. Luckily, methanol is not strongly absorptive at this wavelength, making it a good choice for this experiment. Figure VI.3 is the absorption spectrum for ICG at a 1-micromolar concentration. The laser wavelength used for this experiment was 800 nm, near the peak absorption of ICG. Table VI.1 lists several values of the absorption coefficient of ICG in methanol for several concentrations. This table shows that the absorption coefficient of methanol is not linear with concentration, but extrapolation to smaller concentrations should be possible using a factor of 11 for each change in magnitude of concentration.

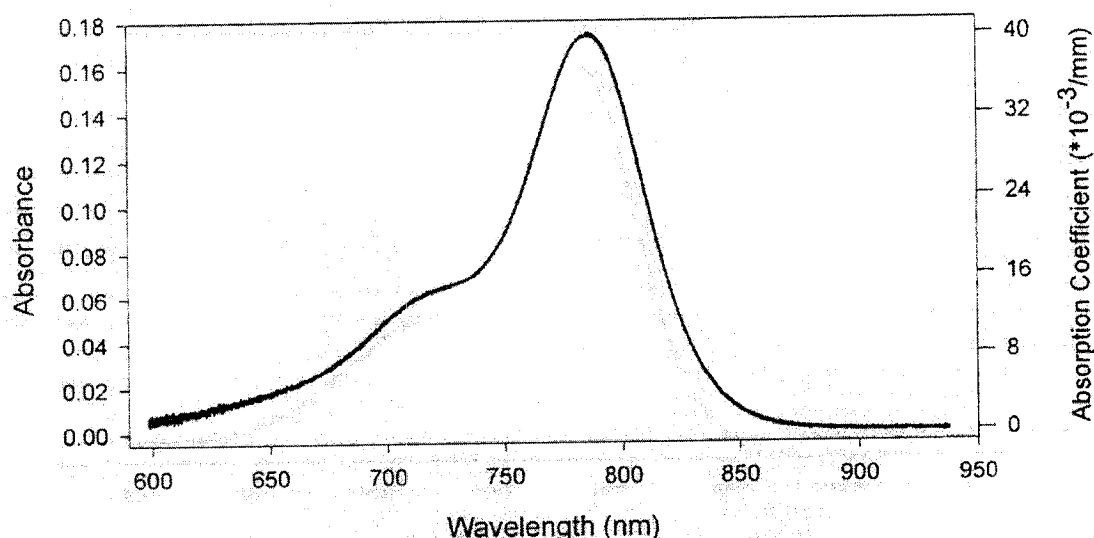


Figure VI.3 Absorption spectrum of ICG in methanol for a 1-micromolar-concentration solution.^[78, 79]

Table VI.1 Absorption coefficient for varying concentrations of ICG in methanol at a wavelength of 800 nm.^[78, 79]

Concentration (μM)	Absorption (m^{-1})
1	35
10	370
100	4000

The microsphere was fabricated using the H-O torch and single bi-tapered fiber coupling was employed. The taper was mounted as described in Chapter III, as shown in Figure III.2 (b). Figure VI.4 shows the reflection spectrum data collected for a 400- μm diameter microsphere that was initially immersed in methanol to which a solution of methanol and ICG was added to increase the absorption. The mode on the far left is with no ICG present and has a Q of 6.7×10^6 . The center resonance frequency of subsequent scans of the same mode has been graphically offset to the right to correspond to the change in ICG concentration surrounding the microsphere. The step size of the change

was initially 1 nanomolar (nM) and increased to 10 nM after the first 10 steps. As the absorption is increased, the dip becomes deeper, indicating that the mode is overcoupled. Between a concentration of 10 and 20 nM, the change in dip depth reverses as the mode is driven through critical coupling. As it does this, the dip does not go all the way to zero. This implies that either there is not perfect mode matching between the tapered fiber and microsphere, that the polarization of light in the taper at the microsphere consists of components that excite TE and TM WGMs, or that the tapered fiber coupling model presented in the Appendix is applicable. For analysis, it is assumed that one of the first two cases given is the correct one since the third case cannot be analyzed due to a lack of information. The dotted line in Figure VI.4 references the offset of the dip. A second, wider, WGM is also present. It appears to be undercoupled since its dip depth decreases with increasing ICG concentration. It will be ignored until the end of this section where it will be addressed.

Plotted in Figure VI.5 is the position of the bottom of the dip, which has been normalized to account for the offset, against the theoretical fit; the theoretical fit is obtained from the information that follows in this paragraph. From the first three points in Figure VI.5, the initial change in dip depth for a change in concentration of 1 nM is 2.3% of the normalized incident power. Using this fact along with $Q = 6.7 \times 10^6$, an on-resonance normalized intensity of 0.17, a wavelength of 800 nm, and equations (II.13), (II.23), and (VI.1), the initial intrinsic loss coefficient of the microsphere in methanol is found to be 0.50 m^{-1} , with total change in absorption of $0.036 \text{ m}^{-1}/\text{nM}$, and an effective transmission coefficient of $T_l = 0.0015$. The theoretical plot in Figure VI.5 is constructed from these three values and equation (II.13), where T_l is held constant and

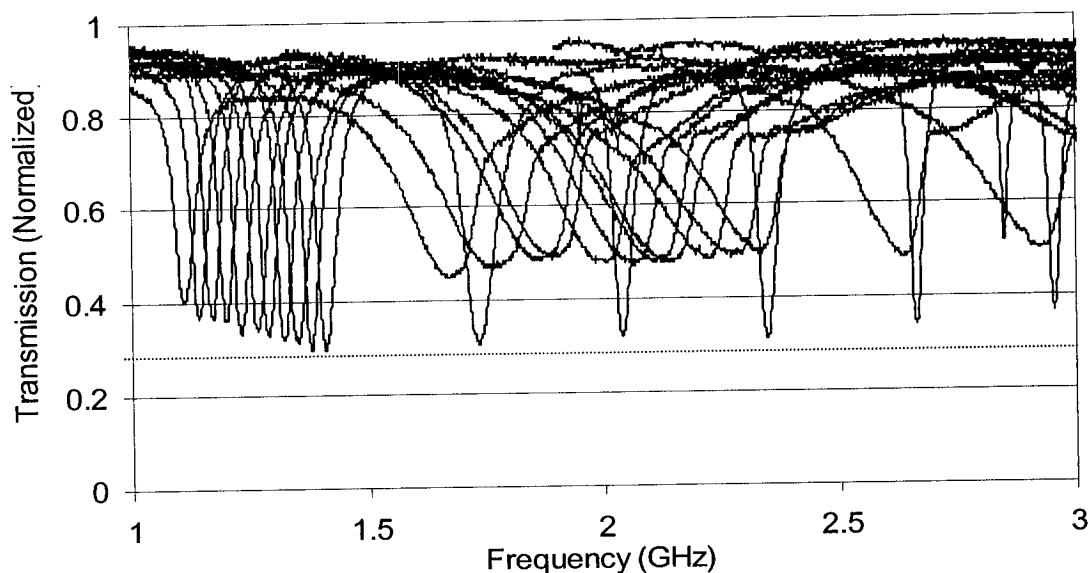


Figure VI.4 Multiple scans of the same WGM at 800 nm of a microsphere immersed in methanol and ICG. The traces are shifted to the right by an amount corresponding to the increase in ICG concentration. The initial concentration is zero followed by 1 nM increases and several 10 nM increases. The higher Q mode, which passes through critical coupling, is analyzed. The dotted line represents the baseline for this mode.

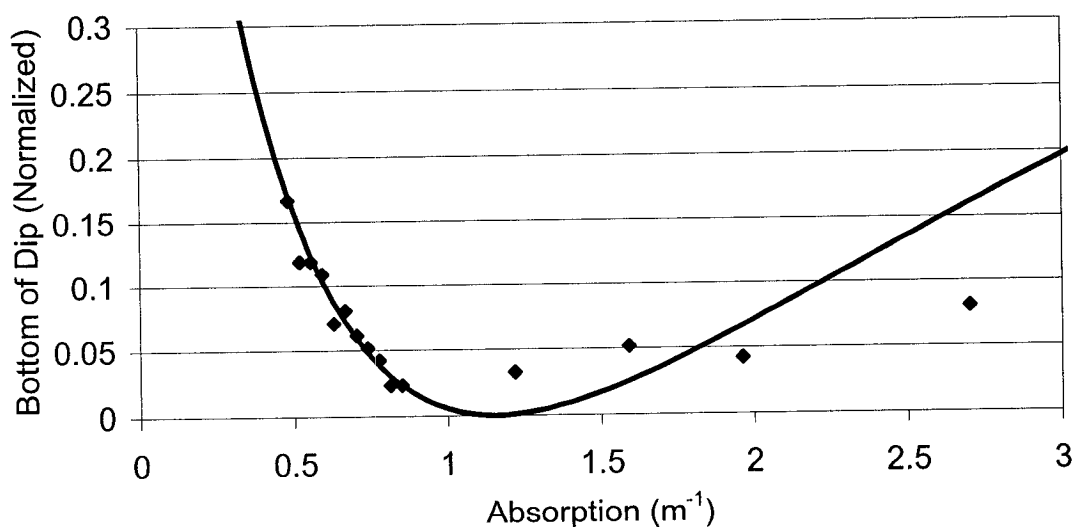


Figure VI.5 Position of dip bottom from Figure VI.4 normalized to account for the baseline offset. The absorption coefficient values are determined from the Q , dip depth, and change in dip depth with increased ICG concentration. The initial intrinsic loss coefficient is 0.50 m^{-1} with an effective change in loss of $0.036 \text{ m}^{-1}/\text{nM}$.

the loss coefficient is changed by an amount that varies linearly with ICG concentration.

Assuming the external mode volume fraction of a 400- μm diameter immersed in methanol is 3% leads to the result that the ICG has an absorption coefficient of 1.2 m^{-1} at a 1-nM concentration. Comparing this to an estimated value of the actual absorption coefficient of 0.026 m^{-1} reveals that the experimental result is almost two orders of magnitude too large, making the microsphere more sensitive than theory predicts and increasing the effective detection path length into the tens of meters.

Turning to the detection path values, an estimate is found by substituting the values of $T_l = 0.0015$, $f = 3\%$ in liquid, and the particular values of α_i into equation (VI.6). As shown in Figure VI.2, which has the same parameters as this experiment, the effective detection path length is not constant for varying values of the intrinsic loss. This leads to a range of detection path lengths from -0.025 m at $\alpha_i = 0.5 \text{ m}^{-1}$ to 0.0042 m at $\alpha_i = 2.66 \text{ m}^{-1}$. These values are the predicted values given the WGM linewidth and dip depth. An experimental detection path length can be determined from equation (VI.4),

$$L_{exp} = -\frac{dM}{M d\alpha_m} \quad (\text{VI.7})$$

where once again M is the dip depth, dM is the change in dip depth, and $d\alpha_m$ is the accepted value for the change in absorption of the medium. This gives an experimental detection path length of -1.06 meters for the first addition of ICG where $\alpha_i = 0.5 \text{ m}^{-1}$.

At this point, attention should be directed to the Appendix, which addresses the issue of fiber taper coupling in which more than one propagation mode of the tapered region couples to the microsphere. This phenomenon modifies the simple ring cavity model that was used to analyze this data and could possibly change the results. This can also explain

why the two modes in Figure VI.4 have approximately the same apparent dip depth in the undercoupled regime and different Q values. Another plausible explanation may be that the ICG adsorbs to the surface of the microsphere, making the ICG concentration higher at the microsphere surface and resulting in an increase in the expected absorption. However, this explanation does not explain the discrepancy in dip depths.

(b) Trace Gas Detection

Trace gas detection is typically performed in the near-infrared region and also in the mid-infrared where the absorption lines are typically stronger, but laser sources and optically transparent materials are less available. Gases with absorption lines in the wavelength region of the tunable diode laser include CO_2 , CO , H_2S , NH_3 , and C_2H_2 ^[80, 81]. Presented here are direct intracavity absorption measurements of CO_2 gas at varying concentrations for the $2\nu_1+2\nu_2+\nu_3$ overtone combination-band absorption line at 1572.4 nm. The gas used in this experiment was a laser mix for a CO_2 laser that contained 9% CO_2 , 15% N_2 , and 76% He . For the CO_2 line that was observed, the spectral line intensity per molecule has a value of $S = 1.84 \times 10^{-23} \text{ cm}^{-1}/(\text{molecule} \cdot \text{cm}^{-2})$ ^[80] and the pressure-broadened linewidth at atmospheric pressure for the laser mix is $\Delta\nu = 0.132 \text{ cm}^{-1}$ (3.97 GHz). These values are related to the resonant molecular absorption coefficient by

$$\alpha_m = \frac{2SN}{\pi\Delta\nu} \quad (\text{VI.8})$$

where $N = 2.7 \times 10^{19} \text{ mol}/(\text{cm}^3 \cdot \text{atm})$ is the total molecular density. At 9% CO_2 this gives a value of $\alpha_m = 2.1 \times 10^{-4} \text{ cm}^{-1}$ or $2.1 \times 10^{-2} \text{ m}^{-1}$. The effective change in loss of the microsphere cavity will be this number times the evanescent volume fraction f of the

WGM, which is typically around 0.25%.

The 500- μm diameter microsphere was fabricated with the H-O torch and tapered fiber coupling was used as shown in the experimental setup in Figure VI.6. As the laser is scanned over a frequency range of 15 GHz at a rate of 100 Hz, the molecular absorption line is detected with the balanced receiver; at the same time, changes in the WGM signal are monitored. The microsphere was housed in the vacuum chamber used

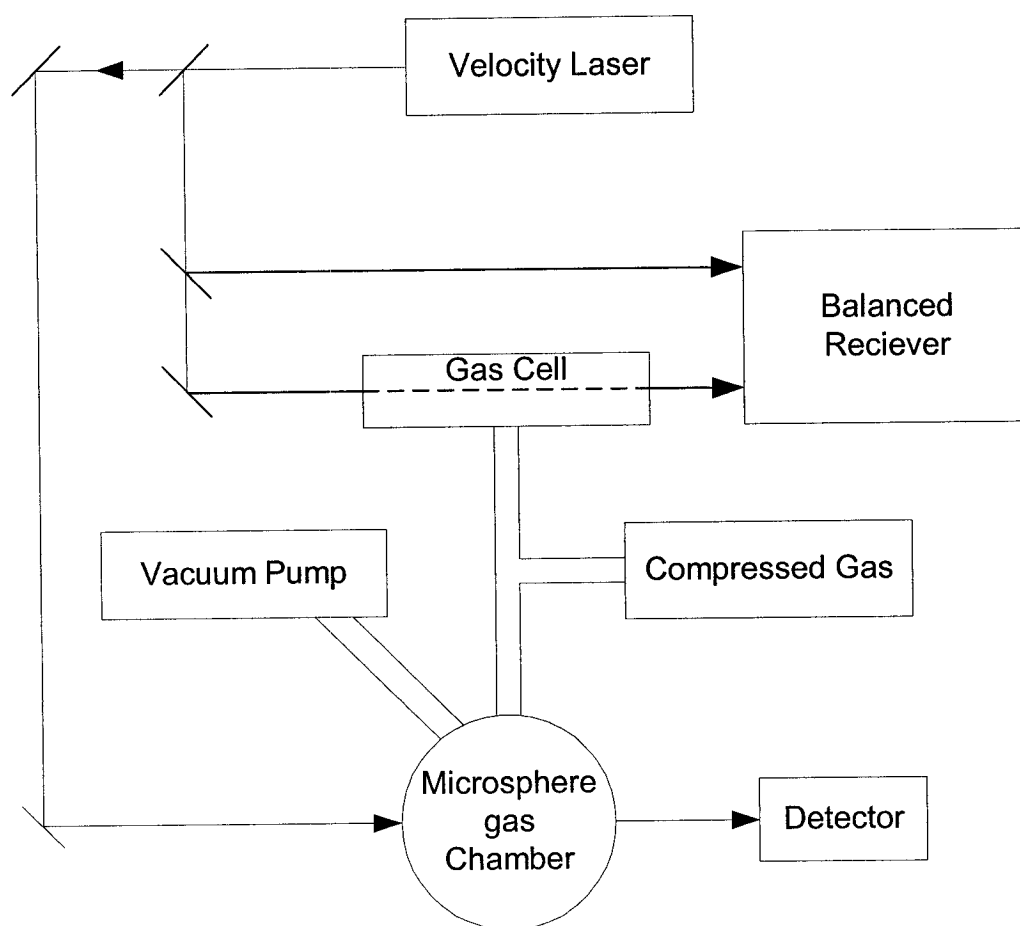


Figure VI.6 Experimental setup for trace gas detection. Absorption lines are found with the gas cell and balanced receiver, while simultaneously performing detection with the microsphere.

for the thermal experiments in Chapter V. Ideally, the microsphere should be mounted in the compression tuner in order to tune a particular WGM over a molecular absorption line. As pointed out in Chapter IV, the coupling, and hence dip depth, can be sensitive to off-axis compression and poses a problem for observing a change in dip depth that corresponds directly to the line shape of the molecular absorption line. Therefore, during this experiment, the microsphere was not mounted in the compression tuner, but rather many WGMs were excited and those that overlapped with the molecular absorption line were examined.

While observing the excited WGMs, the chamber was purged with nitrogen, followed by the addition of the laser mix that contained CO₂. The WGM spectrum at three different CO₂ concentrations at atmospheric pressure is plotted in Figure VI.7, where the traces have been drawn lighter and shifted to the left with increasing concentration. The arrow indicates the CO₂ absorption line center at 1572.4 nm where the absorption linewidth is approximately 4 GHz. The three modes that fall within the region of the molecular absorption line that will be analyzed are labeled 1-3. These modes are all obviously undercoupled since they get shallower with increasing absorption due to the CO₂. Using the WGM linewidth, the loaded Q of the three modes is found to be approximately 3×10^6 .

As was the case for the ICG detection, the possibility of a baseline offset exists. However, there is no way to determine this offset, since the mode does not obviously pass through critical coupling. For CO₂, the absorption coefficient at different concentrations is known; therefore, the analysis of this data will just compare the expected effective detection path length to the experimental detection path length. The

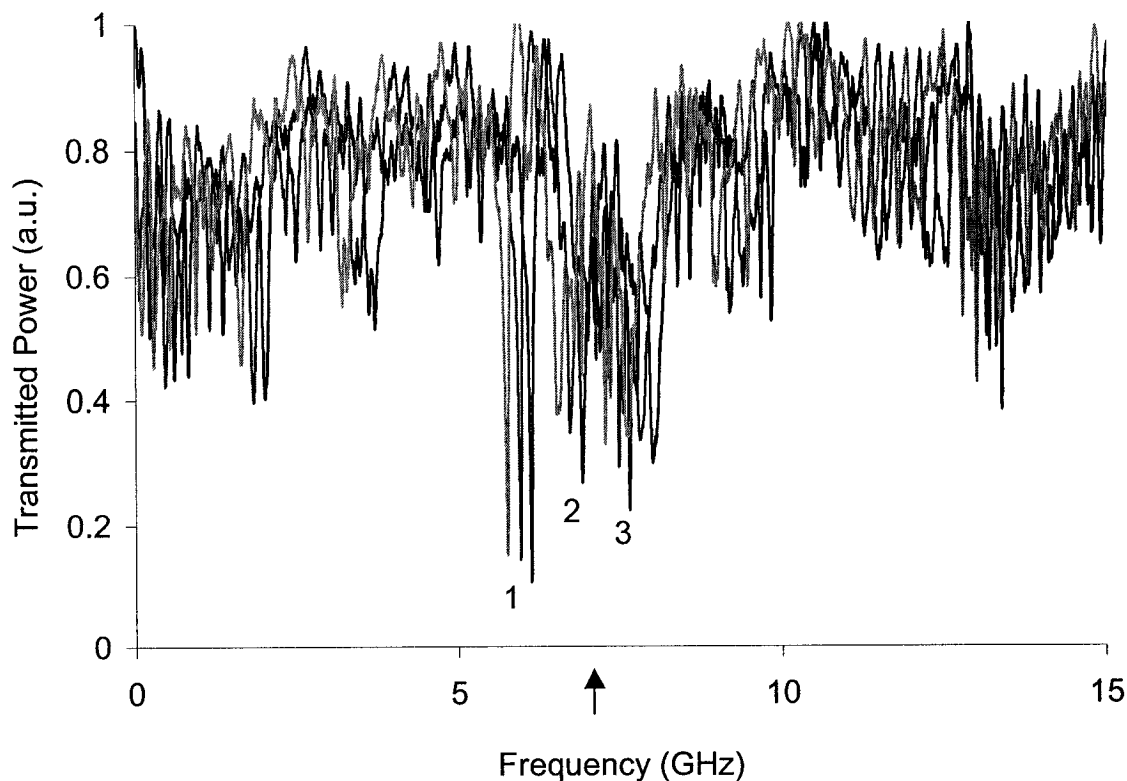


Figure VI.7 WGM spectrum for three different CO₂ concentrations at atmospheric pressure. With increasing concentration, the trace has been drawn lighter and shifted to the left. The arrow indicates the CO₂ absorption line center at 1572.4 nm and the absorption linewidth is approximately 4 GHz. The three numbered modes are analyzed.

first mode is the one that is most clear from structure from other modes and therefore is the one for which numerical values of the dip depth are determined. The other modes appear to overlap with adjacent modes or are in close proximity to other modes, which will affect the measured Q value and baseline. The evanescent mode volume fraction f is taken to be approximately 0.25% in air. All three modes are contained within the molecular linewidth of the CO₂ gas and the exact center of the absorption line is not precisely known, therefore the molecular absorption coefficient will be taken to be the maximum possible value for all three modes. This approximation will vary from the exact amount by a factor of 2 or 3, but the overall magnitude can be determined, which

Table VI.2 Experimental effective detection path length from CO₂ data.

Mode	Initial M	dM (0 to 9% CO ₂)	$d\alpha$ (m ⁻¹)	L_{exp} (m)
1	0.89	0.043	2.1×10^{-2}	23
2	0.733	0.117	2.1×10^{-2}	76
3	0.777	0.111	2.1×10^{-2}	68

Table VI.3 Expected effective detection path length from the observed WGM Q and dip depth.

Mode	Initial M	Q	α_i (m ⁻¹)	T_l	L_{det} (mm)
1	0.89	3×10^6	1.28	0.0010	0.65
2	0.733	3×10^6	1.46	0.0007	0.88
3	0.777	3×10^6	1.42	0.0008	0.83

will be sufficient for this analysis. Table VI.2 gives a summary of the experimental values and the calculated experimental detection path length from equation (VI.7). Table VI.3 gives the expected effective detection path length for the observed WGM, calculated from the measured loaded Q and dip depth using equations (II.13), (II.23), and (VI.6) assuming that the mode is under coupled. It is to our advantage that the data does not agree with the ring cavity model. An intrinsic Q of over 10^{10} would be required for the intensity shift observed using the ring cavity model in Chapter II. Once again, attention should be directed to the Appendix, which could potentially explain the discrepancy. Several attempts to reproduce the data have been unsuccessful, but it is suspected that the experimental parameters need to be adjusted for the modified ring cavity model.

Using the experimental detection path length found here and a limit of $L_{exp}\Delta\alpha > 10^{-3}$ for a detection limit gives a detection level of about 100 ppm for CO₂ at this wavelength.

BIBLIOGRAPHY

1. R.D. Richtmyer, "Dielectric resonators," *J. Appl. Phys.* **10**, 391-398 (1939).
2. J.A. Stratton, *Electromagnetic Theory*, 554-558, (McGraw-Hill, New York, 1941).
3. Y. Yamamoto and R.E. Slusher, *Optical processes in microcavities*, in *Phys. Today* **June** p. 66-73. 1993
4. F. Treussart, N. Dubreuil, J.C. Knight, V. Sandogdhar, J. Hare, V. Lefevre-Seguin, J.-M. Raimond, and S. Haroche, "Microlasers based on silica microspheres," *Ann. Telecommun.* **53**, 557-568 (1997).
5. M. Cai, O. Painter, K.J. Vahala, and P.C. Sercel, "Fiber-coupled microsphere laser," *Opt. Lett.* **25**, 1430-1432 (2000).
6. F. Lissillour, D. Messenger, G. Stephan, and P. Feron, "Whispering-gallery-mode laser at 1.56 μm excited by a fiber taper," *Opt. Lett.* **26**, 1051-1053 (2001).
7. D. Braunstein, A.M. Khazanov, G.A. Koganov, and R. Shuker, "Lowering of threshold conditions for nonlinear effects in microspheres," *Phys. Rev. A* **53**, 3565-3572 (1996).
8. A.N. Oraevsky and D.K. Bandy, "Semiconductor microballs as bistable optical elements," *Opt. Commun.* **129**, 75-80 (1996).
9. A.T. Rosenberger, "Nonlinear optical effects in the whispering-gallery modes of microspheres." in *Operational Characteristics and Crystal Growth of Nonlinear Optical Materials*, R.B. Lal and D.O. Frazier, eds., *Proc. SPIE* **3793**, 179-186, (1999).
10. D.W. Vernooy, A. Furusawa, N. Ph. Georgiades, V.S. Ilchenko, and H.J. Kimble, "Cavity QED with high-Q whispering gallery modes," *Phys. Rev. A* **57**, R2293-R2296 (1998).
11. H. Mabuchi and H.J. Kimble, "Atom galleries for whispering atoms: binding atoms in stable orbits around an optical resonator," *Opt. Lett.* **19**, 749-751 (1994).
12. D.W. Vernooy and H.J. Kimble, "Quantum structure and dynamics for atom galleries," *Phys. Rev. A* **55**, 1239-1261 (1997).
13. V.V. Vassiliev, V.L. Velichansky, V.S. Ilchenko, M.L. Gorodetsky, L. Hollberg, and A.V. Yarovitsky, "Narrow-line-width diode laser with a high-Q microsphere resonator," *Opt. Commun.* **158**, 305-312 (1998).

14. M. Cai, G. Hunziker, and K.J. Vahala, "Fiber-optic add-drop device based on a silica microsphere-whispering gallery mode system," *IEEE Phot. Tech. Lett.* **11**, 686-687 (1999).
15. M. Iodice, G. Cocorullo, F.G. Della Corte, and I. Rendina, "Simple and low-cost technique for wavelength division multiplexing channel monitoring," *Opt. Eng.* **39**, 1704-1711 (2000).
16. J.-P. Laine, B.E. Little, D.R. Lim, L.C. Kimerling, and H.A. Haus, "Planar integrated wavelength-drop device based on pedestal antiresonant reflecting waveguides and high-Q silica microspheres," *Opt. Lett.* **25**, 1636-1638 (2000).
17. H.M. Tzeng, M.B. Long, R.K. Chang and P.W. Barber, "Laser-induced shape distortions of flowing droplets deduced from morphology-dependent resonances in fluorescence spectra," *Opt. Lett.* **10**, 499-502 (1984).
18. A. Serpenguzel, S. Arnold, G. Griffel, and J.A. Lock, "Enhanced coupling to microsphere resonances with optical fibers," *J. Opt. Soc. Am. B.* **14**, 790-795 (1997).
19. L. Maleki, A.F.J. Levi, X.S. Yao, and V. Ilchenko, *Whispering-gallery-mode microspheres as light modulators*, JPL New Technology Report NPO- 21061: NASA Tech Brief. **24** No. 11. 2001.
20. V.B. Braginsky, M.L. Gorodetsky, and V.S. Ilchenko, "Quality-factor and nonlinear properties of optical whispering-gallery modes," *Phys. Lett. A* **137**, 393-397 (1989).
21. D.A. Pinnow, T.C. Rich, F.W. Ostermayer, Jr., and M DiDomenico, Jr., "Fundamental optical attenuation limits in the liquid and glassy state with application to fiber optic waveguide materials," *Appl. Phys. Lett.* **22**, 527 (1973).
22. M.L. Gorodetsky, A.D. Pryamikov, and V.S. Ilchenko, "Rayleigh scattering in high-Q microspheres," *J. Opt. Soc. Am. B.* **17**, 1051-1057 (2000).
23. Govind P. Agrawal, *Fiber-Optic Communication Systems*, 2nd ed, Wiley series in Microwave and Optical Engineering,(John Wiley & Sons, Inc., New York, 1997).
24. V.S. Ilchenko and M.L. Gorodetskii, "Thermal nonlinear effects in optical whispering gallery microresonators", *Laser Physics* **2** 1004-1009 (1992).
25. Erik Streed, Advisor: H. Jeff Kimble, *Spectroscopy of very high Q whispering gallery modes in silica microspheres*, in *Physics*, Caltech No.. p. 26. 1999
26. L. Collot, V. Lefevre-Seguin, M. Brune, J.-M. Raimond and S. Haroche, "Very high-Q whispering-gallery mode resonances observed on fused silica microspheres," *Europhys. Lett.* **23**, 327-334 (1993).
27. W. von Klitzing, R. Long, V. S. Ilchenko, J. Hare, and V. Lefevre-Seguin, "Frequency tuning of the whispering-gallery modes of silica microspheres for cavity quantum electrodynamics and spectroscopy," *Opt. Lett.* **26**, 166-168 (2001).

28. D.S. Weiss, V. Sandoghdar, J. Hare, V. Lefevre-Seguin, J.-M. Raimond, and S. Haroche, "Splitting of high-Q Mie modes induced by light backscattering in silica microspheres," *Opt. Lett.* **20**, 1835-1837 (1995).
29. M.L. Gorodetsky, A.A. Savchenkov, and V.S. Ilchenko, "Ultimate Q of optical microsphere resonators," *Opt. Lett.* **21**, 453-455 (1996).
30. D.W. Vernooy, V.S. Ilchenko, H. Mabuchi, E.W. Streed, and H.J. Kimble, "High-Q measurements of fused-silica microspheres in the near infrared," *Opt. Lett.* **23**, 247-249 (1998).
31. M.L. Gorodetsky and V.S. Ilchenko, "High-Q optical whispering-gallery microresonators: precession approach for spherical mode analysis and emission patterns with prism couplers," *Opt. Commun.* **113**, 133-143 (1994).
32. V.S. Ilchenko, P.S. Volikov, V.L. Velichansky, F. Treussart, V. Lefevre-Seguin, J.-M. Raimond, and S. Haroche, "Strain-tunable high-Q optical microsphere resonator," *Opt. Commun.* **145**, 86-90 (1998).
33. V. S. Ilchenko, M.L. Gorodetsky, X. Steve Yao, and L. Maleki, "Microtorus: a high-finesse microcavity with whispering-gallery modes," *Opt. Lett.* **26**, 256-258 (2001).
34. Kimbles group, at OSA annual meeting (personal communication, 2001)
35. S. Schiller and R.L. Byer, "High-resolution spectroscopy of whispering gallery modes in large dielectric spheres," *Opt. Lett.* **16**, 1138-1140 (1991).
36. M.L. Gorodetsky and V.S. Ilchenko, "Optical microsphere resonators: optimal coupling to high-Q whispering-gallery modes," *J. Opt. Soc. Am. B.* **16**, 147-154 (1999).
37. J.C. Knight, G. Cheung, F. Jacques, and T.A. Birks, "Phase-matched excitation of whispering-gallery-mode resonances by fiber taper," *Opt. Lett.* **22**, 1129-1131 (1997).
38. M. Cai, O. Painter, and K.J. Vahala, "Observation of critical coupling in a fiber taper to a silica-microsphere whispering-gallery mode system," *Phys. Rev. Lett.* **85**, 74-77 (2000).
39. M. Cai and K.J. Vahala, "Highly efficient optical power transfer to whispering-gallery modes by use of a symmetrical dual-coupling configuration," *Opt. Lett.* **25**, 260-262 (2000).
40. J.-P. Laine, B.E. Little, H.A. Haus, "Etch-eroded fiber coupler for whispering-gallery-mode excitation in high-Q silica microspheres," *IEEE Phot. Tech. Lett.* **11**, 1429-1431 (1999).
41. N. Dubreuil, J.C. Knight, D.K. Leventhal, V. Sandoghdar, J. Hare, and V. Lefevre, "Eroded monomode optical fiber for whispering-gallery mode excitation in fused-silica microspheres," *Opt. Lett.* **20**, 813-815 (1995).
42. B.E. Little, J.-P. Laine, and H.A. Haus, "Analytic theory of coupling from tapered fibers and half-blocks into microsphere resonators," *J. Lightwave Technol.* **17**, 704-715 (1999).

43. V.S. Ilchenko, X.S. Yao, and L. Maleki, "Pigtailing the high-Q microsphere cavity: a simple fiber coupler for optical whispering-gallery modes," *Opt. Lett.* **24**, 723-725 (1999).
44. V.S. Ilchenko, X.S. Yao, and L. Maleki, "Microsphere integration in active and passive photonics devices." in *Laser Resonators III*, A.V. Kudryashov and A.H. Paxton, eds., Proc. SPIE **3930**, 154-162, (2000).
45. B.E. Little, J.-P. Laine, D.R. Lim, H.A. Haus, L.C. Kimerling, and S.T. Chu, "Pedestal antiresonant reflecting waveguides for robust coupling to microsphere resonators and for microphotonic circuits," *Opt. Lett.* **25**, 73-75 (2000).
46. Frank L. Pedrotti, S.J. and Leno S. Pedrotti, *Introduction to Optics*, 2nd ed., (Prentice Hall, Englewood Cliffs, New Jersey, 1993).
47. Ying Lu, Ji-You Wang, Xiao-Xuan Xu, Shi-Hong Pan, and Cun-Zhou Zhang, "Optimal conditions of coupling between the propagating mode in a tapered fiber and the given WG mode in a high-Q microsphere," *Optik* **112**, 109-113 (2001).
48. R.P. Kenny, T.A. Birks, and K.P. Oakley, "Control of optical fibre taper shape," *Electron. Lett.* **27**, 1654-1656 (1991).
49. A.W. Snyder, "Coupling of modes on tapered dielectric cylinder," *IEEE Trans. Microwave Theory Tech.* **MTT-18**, 383 (1970).
50. D.T. Cassidy, D.C. Johnson, and K.O. Hill, "Wavelength-dependent transmission of monomode optical fiber tapers," *Appl. Opt.* **24**, 945-950 (1985).
51. W. von Klitzing, R. Long, V.S. Ilchenko, J. Hare, and V. Lefevre-Seguin, "Tunable whispering gallery modes for spectroscopy and CQED experiments," *New Journal of Physics* **3**, 14.1-14.14 (2001).
52. J.P. Rezac and A.T. Rosenberger, "Locking a microsphere whispering-gallery mode to a laser," *Opt. Express* **8**, 605-610 (2001).
53. J.P. Rezac and A.T. Rosenberger, "Locking and laser-frequency tracking of a microsphere whispering-gallery mode." in *Laser Resonators IV*, A.V. Kudryashov and A.H. Paxton, eds., Proc. SPIE **4270**, 112-119, (2001).
54. W. von Klitzing, E. Jahier, R. Long, F. Lissillour, V. Lefevre-Seguin, J. Hare, J.-M. Raimond, and S. Haroche, "Very low threshold green lasing in microspheres by up-conversion of IR photons," *J. Opt. B: Quantum Semiclass. Opt.* **2**, 204-206 (2000).
55. A.T. Rosenberger and J.P. Rezac, "Evanescent-wave sensor using microsphere whispering-gallery modes." in *Laser Resonators III*, A.V. Kudryashov and A.H. Paxton, eds., Proc. SPIE **3930**, 186-192 (2000).
56. I.H. Malitson, "Interspecimen Comparison of the Refractive Index of Fused Silica," *J. Opt. Soc. Am.* **55**, 1205-1209 (1965).
57. *CRC Handbook of Chemistry and Physics*, (1990), pp. F-64.
58. H.S. Carslaw and J.C. Jaeger, *Conduction of Heat in Solids*, (Clarendon, Oxford, 1959).

59. W. R. Foss and E.J. Davis, "Transient Laser Heating of Single Solid Microspheres," *Chem. Eng. Commun.* **152-153**, 113-138 (1996).
60. Sarah Bates, "Non-linear thermal effects in microsphere whispering-gallery modes," *Proc. NCUR* (2001).
61. Seth Koterba, "Observing the thermal conductivity of air with microsphere whispering-gallery modes," REU Project Report, Oklahoma State University (2001).
62. E. H. Kennard, *Kinetic Theory of Gases*, (McGraw-Hill, New York, 1938), Chap. VIII, pp. 291-337.
63. E.H. Kennard, *Kinetic Theory of Gases*, (McGraw-Hill, New York, 1938), pp. 312-315
64. S.C. Saxena and R.K. Joshi, *Thermal accommodation coefficient and adsorption coefficients of gases*, CINDAS data series on material properties, (McGraw-Hill, New York, 1981).
65. G.M. Hale and M.R. Query, "Optical constants of water in the 200-nm to 200- μ m wavelength range," *Appl. Opt.* **12**, 555-563 (1973).
66. D.M. Wieliczka, S. Weng, and M.R. Query, "Wedge shaped cell for highly absorbent liquids: infrared optical constants of water," *Appl. Opt.* **28**, 1714-1719 (1989).
67. V. Weldon, J. O'Gorman, P. Phelan, J. Hegarty, and T. Tanbun-Ek, "H₂S and CO₂ gas sensing using DFB laser diode emitting at 1.57 μ m," *Sensors and Actuators B* **29**, 101-107 (1995).
68. M. Gabrysch, C.Corsi, F.S. Pavone, and M. Inguscio, "Simultaneous detection of CO and CO₂ using a semiconductor DFB diode laser at 1.578 μ m," *Appl. Phys. B* **65**, 75-79 (1997).
69. L-S Ma, Jun Ye, P. Dube, and J. Hall, "Ultrasensitive frequency-modulation spectroscopy enhanced by a high-finesse optical cavity: theory and application to overtone transitions of C₂H₂ and C₂HD," *J. Opt. Soc. Am. B.* **16**, 2255-2268 (1999).
70. A.T. Rosenberger and J.P. Rezac, "Whispering-gallery-mode evanescent-wave microsensor for trace-gas detection." in *Biomedical Instrumentation Based on Micro- and Nanotechnology*, R.P. Mariella and D.V. Nicolau, eds., *Proc. SPIE* **4265**, 102-112 (2001).
71. L. Maleki and V. Ilchenko, *Microsphere and microcavity optical-absorption sensors*, JPL New Technology Report NPO- 21061: NASA Tech Brief **25** No. 4. 2001
72. Thomas Lee, N.A. George, S. P. Sureshkumar, and P. Radhakrishnan, C.P.G. Vallabhan, V.P.N. Nampoori, "Chemical sensing with microbent optical fiber," *Opt. Lett.* **26**, 1541-1543 (2001).

73. A.C.R. Pipino, J.W. Hudgens, and R.E. Huie, "Evanescent wave cavity ring-down spectroscopy with a total-internal-reflection micravity," *Rev. Sci. Instrum.* **68**, 2978-2989, (1997).
74. A.G. Mignani, R. Falciai, and L. Ciaccheri, "Evanescent wave absorption spectroscopy by means of bi-tapered multimode optical fibers," *Appl. Spectr.* **52**, 546-551 (1998).
75. P.N. Moar, S.T. Huntington, J. Katsifolis, L.W. Cahill, A. Roberts and K.A. Nugent, "Fabrication, modeling and direct evanescent field measurement of tapered optical fiber sensors," *J. Appl. Phys.* **85**, 3395-3398 (1999).
76. Robert W. Boyd and John E. Heebner, "Sensitive disk resonator photonic biosensor," *Appl. Opt.* **40**, 5742-5747 (2001).
77. Steve Blair and Yan Chen, "Resonant-enhanced evanescent-wave fluorescence biosensing with cylindrical optical cavities," *Appl. Opt.* **40**, 570-582 (2001).
78. Jason Crull, *Degradation behavior of indocyanine green dye during high intensity laser irradiation*, Masters Thesis, Physics Dept., Oklahoma State University (1994).
79. R. Philip, A. Penzkofer, W. Baumer, R.M. Szeimies, and C. Abels, "Absorption and fluorescence spectroscopic investigation of indocyanine green," *J. Photochem. Photobio.* **96**, 137-148 (1996).
80. L.S. Rothman, C.P. Rinsland, A. Goldman, et al., "The HITRAN molecular spectroscopic database and HAWKS (Hitran Atmospheric Workstation): 1996 edition," *J. Quant. Spect. and Rad. Transfer* **60**, 665-710 (1998).
81. The HITRAN molecular spectroscopic database, (1996).

APPENDIX

MODIFIED RING CAVITY MODEL

The modified model presented here has only recently been developed and is included as an Appendix because it affects almost every chapter in this dissertation. The notation and symbols used in this Appendix are the same as those used to develop the original model in Chapter II. Over the last several years, it has become apparent that there are some inconsistencies with the ring cavity model. Where only dips are expected, peaks, or partial peaks arise. In addition, as the gap distance is adjusted, the transmission and absorption coefficients are inconsistent with expected values. This suggests that the actual intrinsic Q is much higher than that calculated from the dip depth and observed loaded Q value. Agreeing with this conclusion are the gas and liquid chemical detection results from Chapter VI; they yield sample absorption coefficients that are too large, or an intrinsic Q that is much higher than what is observed.

The presence of peaks at WGM resonance frequencies and/or peaks with the same linewidth as a WGM, suggest the phenomenon is more than simple tapered fiber transmission changes due to an index change from the presence of the microsphere. The most obvious, and most plausible, reason for this is the presence of two or more modes propagating through the tapered section of the fiber, with only one recaptured at the other end of the taper. Each fiber mode has a different phase and coupling strength to the microsphere, resulting in the observed phenomena.

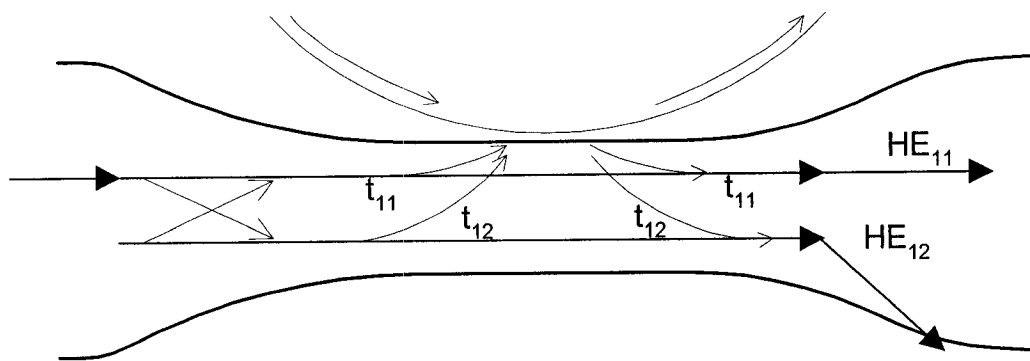


Figure A.1 Representation of the two-mode tapered fiber coupling to the microsphere. The amount of light coupled into the microsphere by each mode is given by the transmission coefficients. For modeling this process, tapered-fiber intermode coupling is ignored in the transition region past the microsphere.

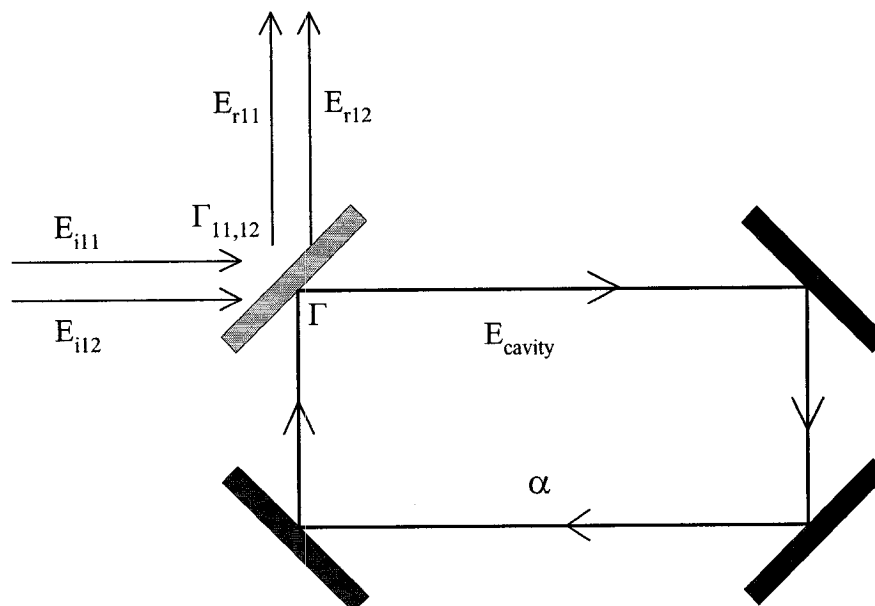


Figure A.2 Modified ring cavity model has two spatially overlapped input beams, each at same frequency, but out of phase with each other by an amount β . The effective transmission coefficients are different for each beam. The internal effective reflectivity of the coupling mirror is given by Γ with no subscripts. For simplicity, transmission signals are ignored.

Figure A.1 shows a schematic of the fiber-microsphere coupling interactions used for the modified model. The effective electric field transmission coefficients for each mode are represented by t_x , with their relationship to the reflection and intensity transmission coefficients given in Equation (A.1). As described in Chapter III, the light in the fiber is single-mode until it reaches the transition region, where it becomes a tapered fiber mode; the tapered fiber is capable of supporting many higher-order cladding-guided modes. As the light propagates in the taper, coupling between the taper fiber modes is possible in the transition regions, where the slope of the taper is not zero. The coupling is predominantly between the two lowest order axial symmetric modes. Both of these modes can couple into and out of the microsphere. After interacting with the microsphere, the reflected light continues to propagate in the tapered fiber and back to the untapered region. More mode coupling will occur (not pictured) in the transition region and all but the lowest order fiber mode will be lost.

All of the literature on tapered fiber coupling to microspheres neglects all fiber modes except for the fundamental. Obviously, this will not always be an accurate representation. Even if the taper transitions are made adiabatic such that there is no coupling between fiber taper modes, the similarity between the HE_{11} and HE_{12} taper modes can result in light coupled out of the microsphere into both modes, and thus coupling into the second mode acts as an extra loss.

The modified four-mirror ring cavity model is shown in Figure A.2. Allowing a second beam that is spatially overlapped with the first to couple to the cavity incorporates the second fiber mode into the model. In this model, the reflection signals from the microsphere are calculated by assuming the light already exists in the two incident

beams. After the microsphere, the two reflected beams could once again couple to each other, resulting in a transfer of power between modes. This would lead to a change in the observed reflection signal. There is no easy way to determine the extent of coupling after the microsphere, so the reflection signals for the fiber modes given in this Appendix are assumed to have no coupling after the microsphere. This limits the model's functionality, and further study of tapered fiber modes to extend this model is most likely necessary if tapered fiber coupling is to be used reliably.

E_{i11} and E_{i12} represent the electric fields for the two beams, where the subscript i , indicating the incident field, will be replaced by r for the reflected field and the 11 and 12 subscripts correspond to the indices of the represented fiber taper modes. Additionally, by using the two-digit indices it is easy to keep this model distinct from that given in Chapter II. The two beams have individual transmission/reflection coefficients that determine the coupling strength of each beam to the cavity. The following relationships are important to the development of the model:

$$\begin{aligned} \Gamma_{11}^2 + t_{11}^2 &= 1 & \Gamma_{12}^2 + t_{12}^2 &= 1 \\ \Gamma^2 + t_{11}^2 + t_{12}^2 &= 1 & t_x^2 &= T_x \end{aligned} \quad (\text{A.1})$$

The reflection coefficient with no index represents the intracavity reflection coefficient of the output mirror. Except for the definition of T_x , the relationships in (A.1) result from the assumption that no power is lost in the coupling mirror and the two incident (or reflected) modes are orthogonal.

The two beams are at the same frequency, but the difference in effective index of refraction between the two modes leads to a phase difference that is dependent on the distance along the taper to the microsphere. Following the same mathematical method as in Chapter II, the electric field inside the cavity, immediately after the input mirror, is

$$E_{cavity} = \frac{t_{11}E_{i11}}{1 - \Gamma e^{\frac{-\alpha_i L}{2}} e^{iLk}} + \frac{t_{12}E_{i12}}{1 - \Gamma e^{\frac{-\alpha_i L}{2}} e^{iLk}} e^{i\beta} \quad (\text{A.2})$$

where β is the phase difference between the two fiber modes and all of the other symbols have their usual meaning. Once inside the microsphere, light is coupled out into either mode. Introducing the symbol m to represent the ratio of E_{i12} to E_{i11} , where $m = 0$ implies no incident energy in the HE_{12} mode, the reflected electric field for the HE_{11} and HE_{12} modes become respectively

$$E_{r11} = \left(-\Gamma_{11} + t_{11} \frac{[t_{11} + t_{12} m e^{i\beta}] e^{\frac{-\alpha_i L}{2}} e^{iLk}}{1 - \Gamma e^{\frac{-\alpha_i L}{2}} e^{iLk}} \right) E_{i11} \quad (\text{A.3})$$

$$E_{r12} = \left(-m \Gamma_{12} e^{i\beta} + t_{12} \frac{[t_{11} + t_{12} m e^{i\beta}] e^{\frac{-\alpha_i L}{2}} e^{iLk}}{1 - \Gamma e^{\frac{-\alpha_i L}{2}} e^{iLk}} \right) E_{i11} \quad (\text{A.4})$$

Since only the HE_{11} mode is recaptured by the fiber after the taper, all experimental data are normalized to its intensity level. Therefore, all of the equations are written with respect to this mode. This has the disadvantage that as the amount of energy in the HE_{11} mode goes to zero, m goes to infinity and a different normalization scheme is needed. Fortunately, this situation never arises experimentally and can be ignored.

By assuming small intracavity and coupling losses, and near-resonance tuning, these approximations apply:

$$e^{\frac{-\alpha_i L}{2}} e^{iLk} \approx 1 - \frac{\alpha_i L}{2} + i\phi \quad \Gamma \approx 1 - \frac{T_{11} + T_{12}}{2}. \quad (\text{A.5})$$

Additionally, by assuming that $t_{11}t_{12}m\alpha_i L$ and $t_{11}t_{12}m\phi$ are much smaller than one, and neglecting-higher order terms, the reflected electric fields are

$$E_{r11} = \frac{(T_{11} - T_{12} - \alpha_i L) + 2\sqrt{T_{11}T_{12}}me^{i\beta} + 2i\phi}{(T_{11} + T_{12} + \alpha_i L) - 2i\phi} E_{i11} \quad (\text{A.6})$$

$$E_{r12} = \frac{2\sqrt{T_{11}T_{12}} + me^{i\beta} [T_{12} - T_{11} - \alpha_i L + 2i\phi]}{(T_{11} + T_{12} + \alpha_i L) - 2i\phi} E_{i11}. \quad (\text{A.7})$$

The intensities calculated from these electric fields are

$$I_{cavity} = I_{i11} \left(\frac{4T_{11} + 4m^2T_{12} + 8\sqrt{T_{11}T_{12}}m \cos \beta}{(T_{11} + T_{12} + \alpha_i L)^2 + 4\phi^2} \right) \quad (\text{A.8})$$

$$I_{r11} = I_{i11} \left(\frac{(T_{11} - T_{12} - \alpha_i L)^2 + 4\phi^2}{(T_{11} + T_{12} + \alpha_i L)^2 + 4\phi^2} + \frac{4m^2T_{11}T_{12} + 4m(T_{11} - T_{12} - \alpha_i L)\sqrt{T_{11}T_{12}} \cos \beta + 8m\phi\sqrt{T_{11}T_{12}} \sin \beta}{(T_{11} + T_{12} + \alpha_i L)^2 + 4\phi^2} \right) \quad (\text{A.9})$$

$$I_{r12} = I_{i11} \left(\frac{4T_{11}T_{12} + 4m^2\phi^2 + m^2(T_{12} - T_{11} - \alpha_i L)^2}{(T_{11} + T_{12} + \alpha_i L)^2 + 4\phi^2} + \frac{4m(T_{12} - T_{11} - \alpha_i L)\sqrt{T_{11}T_{12}} \cos \beta - 8m\phi\sqrt{T_{11}T_{12}} \sin \beta}{(T_{11} + T_{12} + \alpha_i L)^2 + 4\phi^2} \right) \quad (\text{A.10})$$

With no incident power in the HE₁₂ mode ($m = 0$), equations (A.8), (A.9) and (A.10) give the same results as the intracavity, reflection, and transmission intensity results as the original ring cavity model, equations (II.14), (II.13), and (II.15) respectively, where T_{11} takes the place of T_1 and T_{12} takes the place of T_3 . This implies that with $m = 0$, I_{r11} is the same as the reflected signal and I_{r12} is the same as the transmission signal in the original model. This limit is expected since both models will have one input signal and an additional cavity loss signal. This suggests that if perfectly adiabatic fibers are produced, and the HE₁₁ and HE₁₂ tapered fiber modes could be observed separately, reflection and transmission signals could be observed from a single tapered fiber instead of two. The additional terms in equations (A.9) and (A.10), containing m act to raise or lower dip

depth. This makes the actual dip depth different than what would be expected from the original model. Trying to use the dip depth and linewidth to determine T_l and α_i , as was done in Chapter II, becomes inaccurate.

Another obvious, but very important, prediction from equation (A.9) is that the observed dip may be asymmetric. This is not possible in the original model, but the cavity detuning term ϕ in front of the $\sin\beta$ term leads to the transmitted intensity being dependent upon which side of resonance the frequency sits. The magnitude of the asymmetry is determined by m and β , where there is no asymmetry in the $m = 0$ case, and the phase difference between the two tapered fiber modes determines the magnitude and direction of the asymmetry. Little or no observed asymmetry implies either the phase difference between fiber modes is zero or π , or that there is minimal energy in the HE_{12} mode. Equation (A.10) shows that this phenomenon is also present in the uncaptured reflection signal with opposite sign, making it asymmetric in the opposite direction. However, there is no asymmetry in the intracavity intensity. This means the frequency of the maximum intracavity intensity (the true resonance frequency) corresponds to the frequency position of the observed maximum dip depth only when m is zero or β is zero or π .

As mentioned in Chapter II, an alternative way of expressing the lineshapes of the WGM is to write the intensities in terms of a Lorentzian. The intracavity intensity obviously has this lineshape, however, the equations for the reflection intensities are a little less obvious. The observable reflection intensity, I_{r11} , has a one minus a Lorentzian lineshape, with an additional term that makes it asymmetric. It can be written as

$$I_{r11} = I_{i11} \left[1 - U \frac{(\Delta\phi/2)^2}{(\Delta\phi/2)^2 + \phi^2} + V \frac{\phi}{(\Delta\phi/2)^2 + \phi^2} \right] \quad (\text{A.11})$$

where $\Delta\phi = T_{11} + T_{12} + \alpha_i L$ is the linewidth as defined by the intracavity intensity, and the normalized on-resonance dip depth and asymmetry terms are defined respectively as

$$U = \frac{T_{11}(T_{12} + \alpha_i L) - m^2 T_{11} T_{12} + m(T_{11} - T_{12} - \alpha_i L) \sqrt{T_{11} T_{12}} \cos \beta}{\left(\frac{T_{11} + T_{12} + \alpha_i L}{2} \right)^2} \quad (\text{A.12})$$

$$\text{and} \quad V = m \sqrt{T_{11} T_{12}} \sin \beta. \quad (\text{A.13})$$

Here again, it is obvious from equation (A.11) that the maximum observed dip depth is not necessarily at the resonance frequency, due to the asymmetric term. Comparing equation (A.12) to M in equation (II.25) demonstrates how the dip depth is modified from the original model. A similar analysis of the uncaptured reflected intensity can be performed, but since it not observable, it is not presented here.

Shown in Figure A.3 are theoretical plots of the reflection intensities for the two fiber modes when the microsphere is undercoupled ($T_{11} - T_{12} < \alpha_i L$). The left and right hand vertical scales are for the HE₁₁ and HE₁₂ modes, respectively. The intensity values are given relative to I_{i11} , which is the value of I_{r11} in the limit of large detuning. The values of $m = 1.25$, $\alpha_i = 0.22 \text{ m}^{-1}$, $L = 2\pi(180 \text{ }\mu\text{m})$, and $T_{12} = T_{11} = 0.1 \alpha_i L$ were chosen to demonstrates a range of some of the observable lineshapes, including asymmetry and peaks, for the same WGM. The effect of the phase difference between the two fiber modes can be seen as β values of 0, 0.25, 0.5, 0.75, 1.0 π are plotted for each case. Changing the phase difference from 0 to $-\pi$ gives the same results, but with the asymmetry reversed in scan direction. By changing the values of m and the transmission

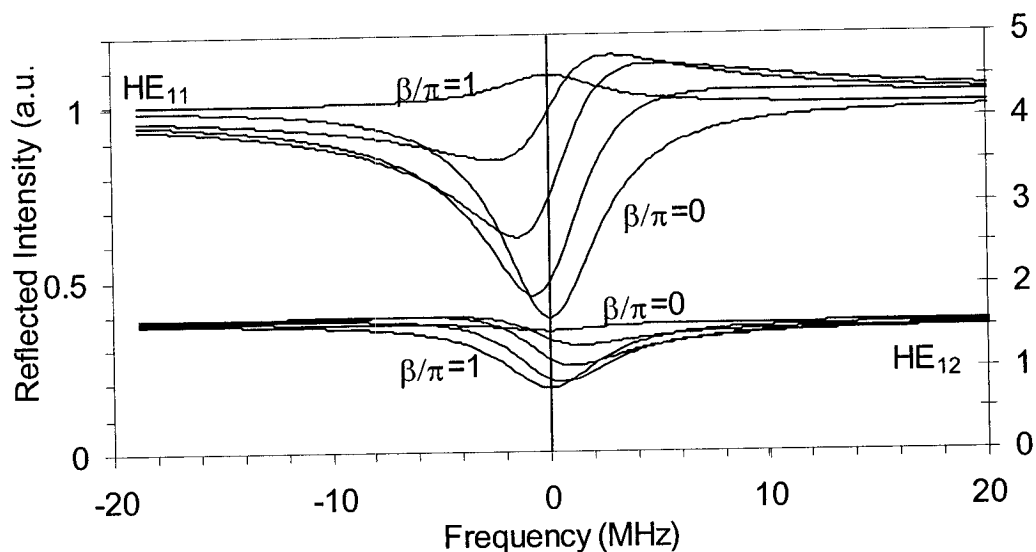
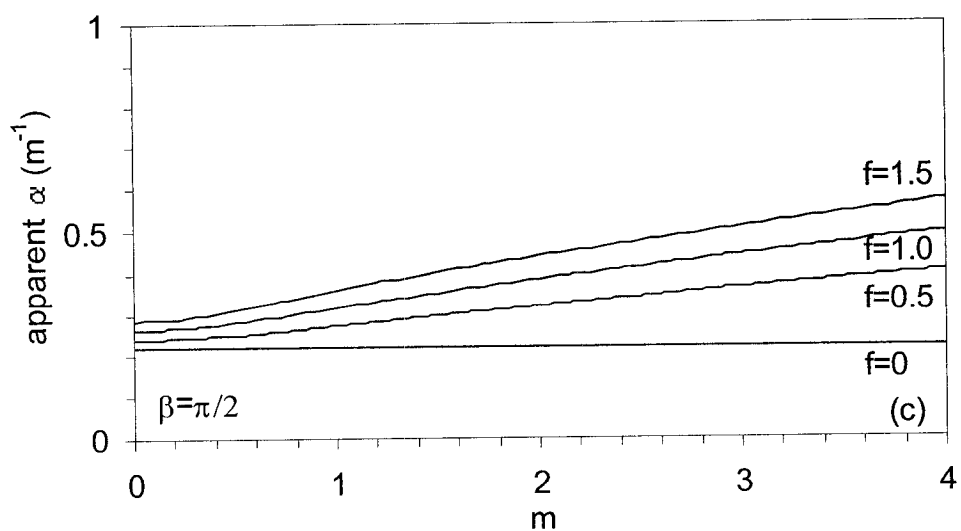
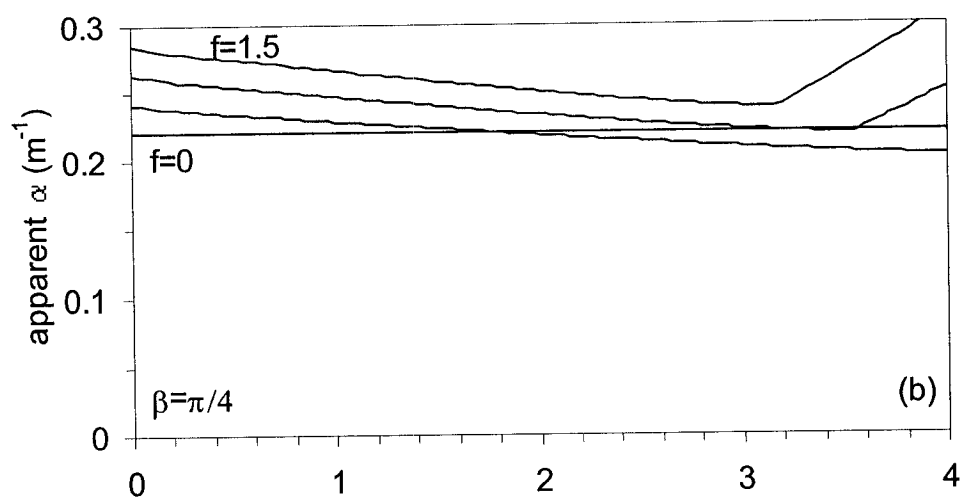
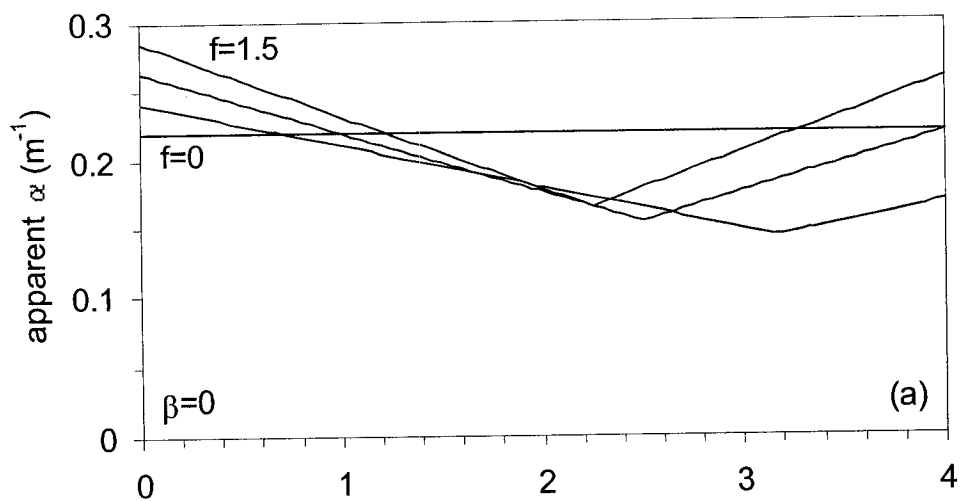


Figure A.3 Shown are some of the observable lineshapes with the modified model for the HE_{11} and HE_{12} modes, upper and lower curves respectively. Plotted are phase differences of 0, 0.25, 0.5, 0.75, 1.0 π between the two fiber modes when $m = 1.25$ and $T_{12} = T_{11} = 0.1 \alpha_i L$. The left and right hand scales are for the HE_{11} and HE_{12} modes, respectively.

coefficients, the peaks or asymmetry can be made more or less prominent.

Figure A.3 demonstrates that maximum dip depth frequency position can be shifted from the actual resonance frequency position by up to half the linewidth. Since the dip depth and observed linewidth change with β , m , and T_{12}/T_{11} , it is interesting to examine how the original model interprets this. Using an undercoupled mode, $\alpha_i = 0.22 \text{ m}^{-1}$, $L = 2\pi(180 \text{ } \mu\text{m})$, and $T_{11} = 0.2 \alpha_i L$, the dip depth and apparent linewidth from the observed reflection are numerically calculated at different values of β , m , and T_{12}/T_{11} . With these two parameters fed into the original model, equations (II.13) and (II.22), the loss coefficient for the undercoupled regime is calculated. The results are shown in Figure A.4, where plots (a)-(e) are for different β values, m is plotted on the x-axis, and different curves are plotted for T_{12}/T_{11} given the values 0, 0.5, 1.0, and 1.5. As



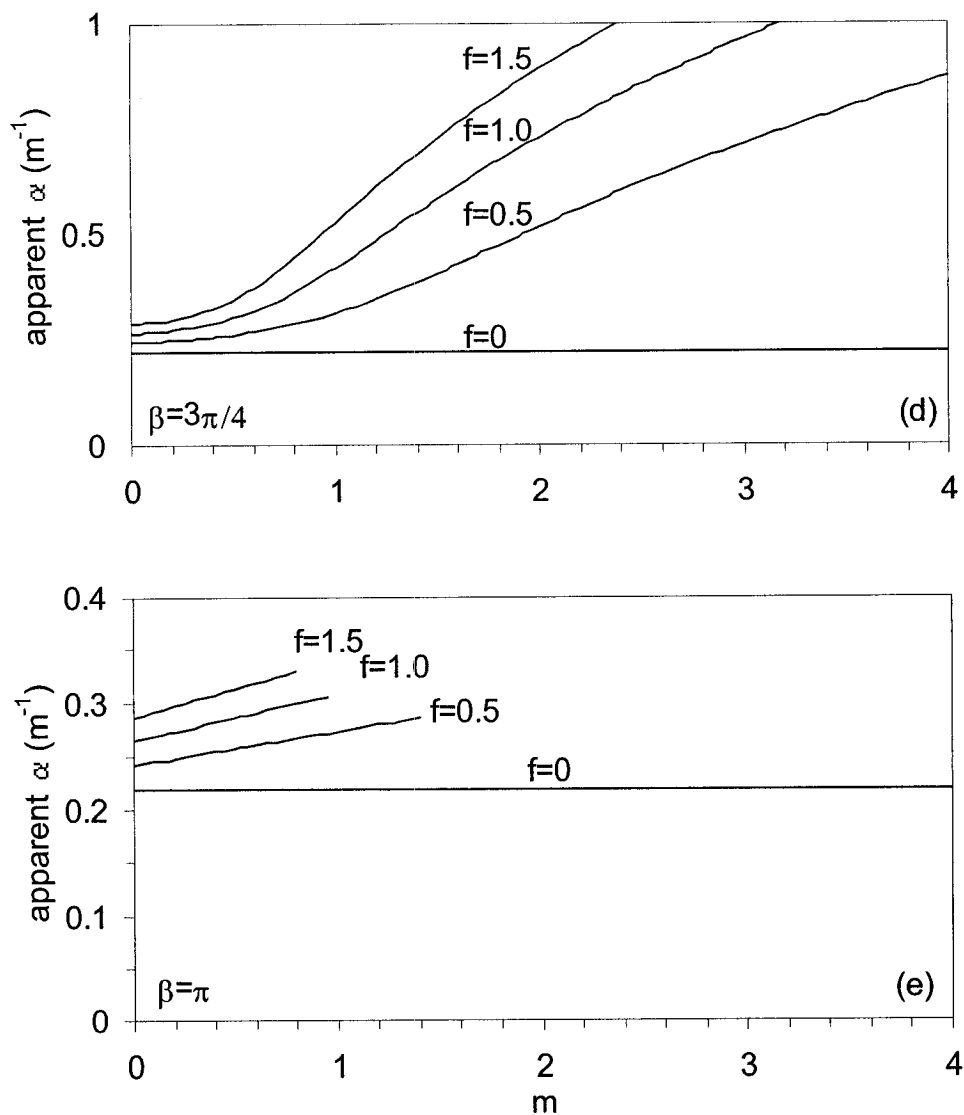


Figure A.4 Plots of the apparent loss coefficient for an undercoupled microsphere using the original single-fiber-mode model with the dip depth and Q calculated from the modified two-mode model. Plots (a)-(e) are for different phase difference between the two tapered fiber modes. m is the ratio of the initial electric fields in the fiber and f is the ratio of the transmission coefficients T_{12}/T_{11} . In the two-mode model, the absorption coefficient is 0.22 m^{-1} . The four values of $f = 0, 0.5, 1.0,$ and 1.5 are graphed in each plot. The curves in (e) end when the dip becomes a peak.

the WGM is moved toward and through critical coupling, the effect is more prominent and larger changes are possible than those presented in Figure A.4. An order of magnitude difference in values can easily be seen with the experimental parameters within a reasonable range. If the absorption coefficient calculated from the original model is larger than the actual value, the intrinsic Q of the microsphere is higher than originally thought.

This model can potentially explain the discrepancies in the trace-gas and liquid chemical detection results. It may also explain why repeatable results with the trace-gas detection were not possible. Once again, it should be pointed out that the extent of this model is limited by the fact that intermode coupling, in the transition region of the fiber after the microsphere, has not been accounted for.

To further validate this model, experimental data was collected and fitted with this model. The results are shown in Figures A.5 and A.6. The bi-tapered fiber used was first heat stretched, then HF acid etched. The wavelength dependence of the fiber transmission was similar to that shown in Figure III.4, where a minimum in transmitted power was observed at 1540 nm and a maximum at 1530 nm. WGM spectra were collected at these two wavelength values to demonstrate different limits of the model. When the transmission is at a minimum, more power is in the HE_{12} mode, giving a higher m value and increasing the likelihood of observing peaks. This is demonstrated in the 1540 nm WGM spectrum shown in Figure A.5, where three peaks are shown with their theoretical fits. The parameters for the theoretical fits took on the values of $m = 4$, $\beta = \pi$, $\alpha_i = 0.6 \text{ m}^{-1}$, and $T_{12} = 0.31T_{11}$ for all three WGMs. The value of T_{11} for the (1), (2), and (3) peaks are $0.075\alpha_iL$, $0.17\alpha_iL$, and $0.045\alpha_iL$ respectively. The value of m was

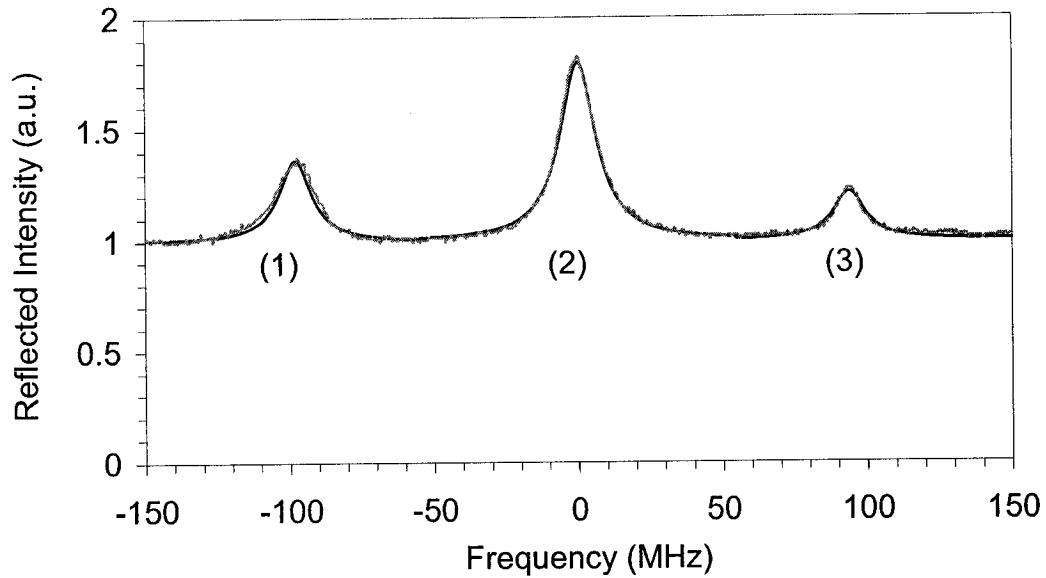


Figure A.5 Experimental verification of the modified ring cavity model. The light curve is the experimental data collected from a 400- μm microsphere at 1540 nm. The dark curve is the theoretical fit with $m = 4$, $\beta = \pi$, $\alpha_i = 0.6 \text{ m}^{-1}$, and $T_{12} = 0.31T_{11}$ for all three WGMs. The value of T_{11} for the (1), (2), and (3) peaks are $0.075\alpha_iL$, $0.17\alpha_iL$, and $0.045\alpha_iL$ respectively.

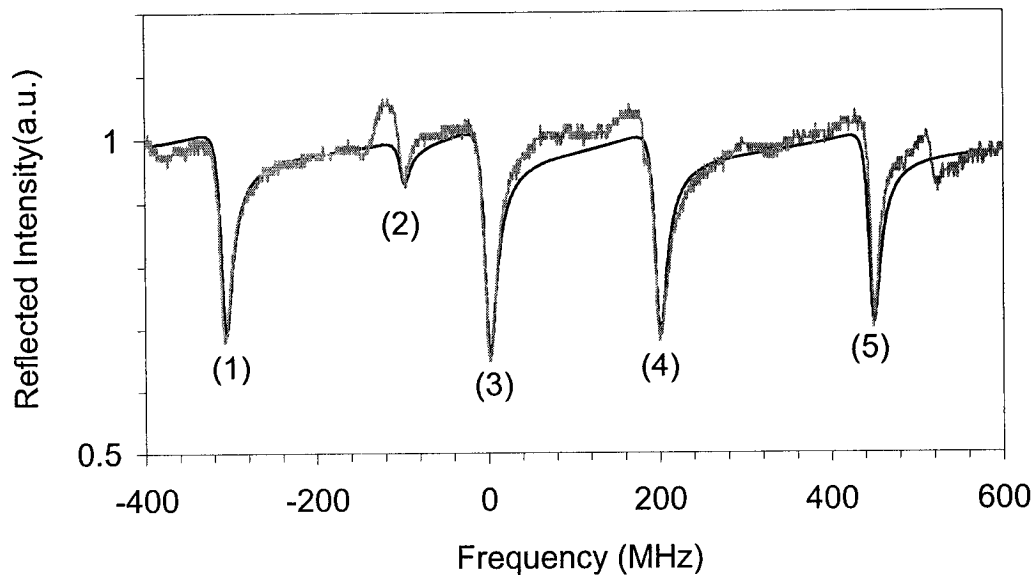


Figure A.6 Experimental verification of the modified ring cavity model. The light curve is the experimental data collected from a 400- μm microsphere at 1530 nm. The dark curve is the theoretical fit with $m = 1.4$, $\beta = -0.4\pi$, $\alpha_i = 0.70 \text{ m}^{-1}$, and $T_{12} = 0.31T_{11}$ for all the WGMs. The value of T_{11} for the (1)-(5) peaks are $0.067\alpha_iL$, $0.012\alpha_iL$, $0.075\alpha_iL$, $0.065\alpha_iL$, and $0.060\alpha_iL$ respectively.

approximated from the difference between the high and low values of transmitted power, and from the value of m that was used for fitting WGMs at the peak of the transmitted power in Figure A.6.

The 1530 nm WGM spectrum is shown in Figure A.5 where five dips are shown with their theoretical fits. The presence of asymmetry automatically implies that even at the maximum transmitted power, not all of the power is in the HE_{11} mode at the microsphere. This implies more than two modes are present in the tapered fiber region. Here the parameters for the theoretical fits took on the values of $m = 1.4$, $\beta = -0.4\pi$, $\alpha_i = 0.7 \text{ m}^{-1}$, and $T_{12} = 0.31T_{11}$ for all the WGMs. The values of T_{11} for the (1)-(5) peaks are $0.067\alpha_i L$, $0.012\alpha_i L$, $0.075\alpha_i L$, $0.065\alpha_i L$, and $0.060\alpha_i L$ respectively. As should be expected, the values of the intrinsic loss coefficient and the transmission coefficient are similar in both cases. It obvious that a perfect fit was not accomplished in Figure A.6, but with a large number of free parameters, this is hard to accomplish. For this demonstration, the important point is not to find exact values of the parameters, but rather to demonstrate the potential of this model to describe the observed phenomena.

VITA 2

JEROMY PAUL REZAC

Candidate for the Degree of

Doctor of Philosophy

Thesis: PROPERTIES AND APPLICATIONS OF WHISPERING-GALLERY MODE
RESONANCES IN FUSED SILICA MICROSPHERES

Major Field: Physics

Biographical:

Personal Data: Born in Breckenridge, Minnesota, on February 17, 1972, the son of Gerald and Margaret Rezac.

Education: Received Bachelor of Science degree in Physics and Mathematics from North Dakota State University, Fargo, ND, in May 1995. Completed the requirements for the Doctor of Philosophy degree with a major in Physics at Oklahoma State University, Stillwater, Oklahoma, in August 2002.